Doctoral Dissertation
博士論文

Planetary systems predicted from the ALMA disks: planet-disk evolution and long-term orbital stability of multi-planets
（アルマ原始惑星系円盤の予言する惑星系：惑星と円盤共進化、及び多重惑星の長期軌道安定性）

A Dissertation Submitted for the Degree of Doctor of Philosophy

December 2021

令和三年十二月 博士（理学）申請

Department of Physics, Graduate School of Science,
The University of Tokyo

東京大学大学院理学系研究科物理学専攻

Shijie Wang
汪 士杰

Abstract

Since the discovery of the first exoplanet in 1992, more than 5,000 exoplanets have been detected to date. The exoplanetary population exhibits a wide distribution over the semi-major axis, eccentricity, inclination and mass. The unexpected diversity strongly challenges the conventional planetary formation and evolution model, and spurred various proposals for the new theories. Despite the theoretical efforts devoted to understand the physical origin of the observed diversity, most of the theoretical predictions of these investigations rely on artificially fine-tuned initial conditions that need to be further justified on a realistic basis. Such a dilemma has long motivated searches for model-independent initial conditions of planetary systems from the protoplanetary disks. Nevertheless, inference of the planetary systems from the bulk properties of the disk involves great uncertainties, since there is no robust model to consistently explain the formation of planets from the first principle. In order to bypass this fundamental difficulty, more direct observational data of the protoplanets are required.

The advent of ALMA and its high resolution dust continuum data revolutionised the disk observation by successfully resolving the ring/gap substructures on HL Tau first in 2015, and later on a large number of protoplanetary disks. The disk substructures are commonly interpreted as signatures for protoplanets. Following the planetary interpretation, the locations and mass of the embedded planets can be directly constrained from the morphology of the gap structure and serve as initial conditions for the numerical investigation concerning the later stage planet-disk evolution. In this thesis, our main purpose is to deduce the realistic initial configurations from the observed protoplanetary disks, and then investigate the evolution outcomes of the planetary systems by numerically evolving the planetary systems within the disk lifetime and after the disk dispersal.

This thesis consists of three main parts. In the first part, we focus on the orbital evolution of planets in the HL Tau disk. At the disk stage, we produce a variety of widely-separated planetary systems consisting of three super-Jupiters by varying the disk parameters. We found the mass growth of the outer planets is more efficient, and the migration of the innermost planet is inefficient due to the accretion of outer planet(s). We also found the final orbital configuration and the final planetary mass depend on disk parameters. The migration is found to be convergent and no planet-pair has a period ratio less than 2. We also examine the orbital stability of the systems after the disk dispersal. Most simulated HL Tau systems remain stable for at least $10\,\mathrm{Gyr}$.

In the second part, we generalise our findings on HL Tau by expanding our targets to more ALMA disks. Predicting mass of those embedded planets is of fundamental importance in extracting the initial planetary configuration from the protoplanetary disks. For HL Tau, the planetary masses are predicted by assuming all three major gaps have opened in the gas disk. However, in a more general context, the planetary mass prediction depends on the assumption whether the same gap structure exists in the dust component alone or in the gas component as well, when observation data on the gas profile are not available. We distinguish the two possibilities by assuming that a planet can only open a gap in the gas component only when its mass exceeds the pebble isolation mass according to the core accretion scenario. We then propose two criteria to distinguish if a gap is opened in the dust disk alone or the gas gap as well. We apply the criteria to 35 disk systems with a total of 55 gaps compiled from previous studies, and classify each

gap into four different groups. The classification of the observed gaps allows us to predict the mass of embedded planets in a consistent manner with the pebble isolation mass. We find that outer gaps are mostly dust alone, while inner gaps are more likely to be associated with a gas gap as well. The distribution of such embedded planets is very different from the architecture of the observed planetary systems, suggesting that the significant inward migration and accretion are required in their later stage evolution.

In the third part, we perform simulations starting from the initial configurations of 12 multi-planetary systems that we deduced from ALMA disks in the second part. We investigate the evolution of the planetary systems at the disk stage as well as the long term orbital stability after the disk dispersal. At the disk stage, We found a variety of planetary systems are produced and have some overlap with the known exoplanetary population. We found the disk stage evolution as well as the final configurations are sensitive to both the initial mass assignments and viscosity. We continue integrating the systems after the disk stage with perturbative forces to test their orbital stability. Most planetary systems are found to be stable for at least $10\,\mathrm{Gyr}$ with perturbative force in a reasonable range. Our result implies that a strong perturbation source such as stellar flybys is required to drive the planetary systems unstable. We discuss the implications of our results on both the disk and planet observation, which may be confirmed by the next generation telescopes such as *JWST* and *ngVLA*.

In this thesis, we systematically investigate the evolution outcome as well as the long term orbital stability of the planetary systems deduced from the protoplanetary disks observed with ALMA. We found the interaction between the disk and the planet can strongly shape the configurations of the planetary systems at the disk stage, and most planetary systems are stable for at least $10\,\mathrm{Gyr}$ after the disk dispersal. The results of this study suggest that strong perturbative sources and/or very turbulent disks are necessary to produce the unstable configurations assumed by the dynamical evolution model. Our results also imply that the potential existence currently unresolved disk substructures at the inner disk as well as exoplanets at the larger orbital distance outside of the current detectability, which may be confirmed by the next generation telescopes.

Acknowledgements

First I would like to express my sincere gratitude to my supervisor, Prof. Yasushi Suto, for his continuous guidance and kind teaching throughout my PhD course. I have learned not only a vast amount of the scientific knowledge that is indispensable to progress in my physics research, but also the correct attitude, dedication and responsibility that are equally important to be a qualified physicist. I would also like to thank my principal collaborator, Dr. Kazuhiro Kanagawa, who broadened the horizon of my knowledge in the area of protoplanetary disks and provided many insightful ideas and suggestions during our weekly discussions. I would like to thank all members of the thesis committee, Prof. Cannon, Prof. Ando, Prof. Takada, Prof. Yamamoto, Prof. Yamasaki for their valuable comments and discussions. I would also like to thank my colleagues and other researchers, including Toshinori Hayashi, Souichiro Hashiba, Tilman Hartwig, Kazumi Kashiyama, Masataka Aizawa, Fei Dai, Ruobing Dong for their valuable contribution to the scientific discussions and constant encouragement that I never take for granted.

I would like to thank all the contributors for their altruistic efforts made to the publicly available open-source projects that are involved in this research, including but not limited to `rebound`, `reboundx`, `spyder`, `pandas`, `matplotlib`, `TeXstudio` and many others that are equally deserved to be listed. This PhD project was greatly benefited from these convenient, elegant, and versatile codes and modules in a way that a great amount of my time is saved for physics instead of dealing with the tedious data analysis.

I would like to thank my parents for their unconditional support, both financially and mentally, which I will appreciate and remember for my whole life.

Finally, I sincerely thank the financial support from the Chinese Scholarship Council (CSC). Most of the numerical simulations are computed on the general calculation node from Center for Computational Astrophysics (CfCA), National Astronomical Observatory of Japan (NAOJ), and the computing cluster `nekoya` offered by the Institute for Physics of Intelligence, the University of Tokyo.

Contents

List of Tables

List of Figures

Chapter 1

Introduction

The history of the planet observation can be dated back to Babyloninan period (e.g., Sachs, 1974), when six out of the eight planets in our solar system have been identified by the ancient astronomers for the first time. The invention of the telescope as well as Newton's formulation of the law of universal gravitation later directly contributed to the discovery of the remaining two planets in the nineteenth century, Uranus and Neptune, marking an important milestone in our endless pursuit of understanding the universe.

However, in contrast to the long history of observation and rich knowledge that we have for our solar system, we are still at the very early but exciting stage in understanding the planetary systems outside solar systems, i.e., the exoplanetary systems. In fact, the first exoplanet was discovered in 1992 as a moon-size object orbiting around the pulsar PSR 1257+12 (Wolszczan & Frail, 1992), together with another super-earth object around the same pulsar. A few years later in 1995, a planet hosted by a main sequence star was detected via radial velocity method, namely the 51 Pegasi b. After launching the Kepler space telescope in 2009, the number of observed exoplanets experienced a rapid increase. As of October 2021, there are $\sim 5,700$ planets in total that have been recorded in the exoplanet database (`exoplanets.org`), including both confirmed planets and Kepler candidates, and this number is readily increasing.

The bursting number of exoplanets brought us fresh insights into the uncharted new worlds that are surprisingly different from our own. Recent analyses on the Kepler systems have revealed that the population of exoplanets exhibits a great diversity that is very different from the solar system (e.g. Henry et al., 2000; Charbonneau et al., 2000; Queloz et al., 2000; Borucki et al., 2010; Ricker et al., 2014; Winn & Fabrycky, 2015). In fact, the aforementioned exoplanet 51 Pegasi b, is thought to be at least twice as massive as Saturn but have an orbital period for only four days (Mayor & Queloz, 1995). The existence of such close-in Hot Jupiters (e.g., Mayor & Queloz, 1995), far-away gas giants (e.g., Chauvin et al., 2004), planets with large spin-orbit misalignment (e.g., Winn et al., 2005, 2009), multi-planetary systems consisting of earth-like planets (e.g., Gillon et al., 2017), and widely separated super-Jupiters (e.g., Marois et al., 2008), all indicate that exoplanets actually have a broad distribution on their semi-major axis, mass, orbital eccentricity and inclinations.

The newly discovered diversity strongly challenged our understanding of the very genesis of the exoplanetary systems, since such exotic architectures were not expected by the

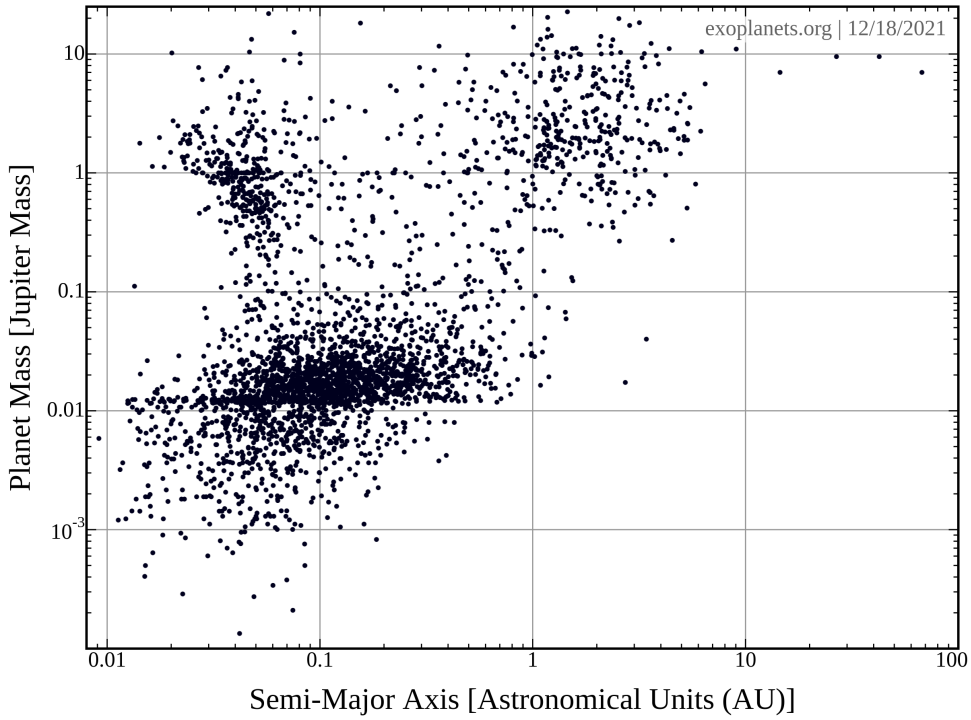

Figure 1.1: Mass and semi-major axis distribution of the exoplanetary population. Source: exoplanets.org, accessed on Dec. 18, 2021.

conventional planetary formation model developed to explain the formation of the Solar system (Hayashi et al., 1985). A significant amount of theoretical efforts have then been devoted to search for the physical explanations to the observed exoplanetary population. It has been proposed that the diverse architecture of the exoplanets may be explained, at least in part, by the dynamical evolution, including but not limited to planetary migration, dynamical instability, tidal circularisation, and secular perturbation (e.g., Lissauer, 1993; Lin & Papaloizou, 1993; Rasio & Ford, 1996; Tanaka & Ida, 1999; Wu & Murray, 2003; Alibert et al., 2005; Nagasawa et al., 2008; Naoz et al., 2011). However, these theoretical investigations mainly rely on artificial initial conditions that favour unstable configurations. Even if such approaches successfully reproduce the desired properties of specific observed planetary population, it is not clear to what extent it can be interpreted as a strong argument in favour of the proposed theoretical model unless the initial condition itself is justified.

The dilemma motivates to search for realistic initial conditions in the protoplanetary disks (PPDs), which are commonly recognised as birthplaces of exoplanets. These circumstellar disk objects not only offer dust and gas material that essentially make up the planet, but also provide suitable environment for the planets to grow. In the standard core accretion scenario (e.g., Mizuno, 1980; Hayashi et al., 1985), dust grains inside the gas disk collide and coagulate, form rocky cores, and eventually grow to giant gaseous planets via runaway gas accretion. Alternatively, a fraction of giant planets may be formed *in-situ* directly by gravitational instability within a massive disk (e.g., Cameron, 1978).

Since exoplanets are born within and co-evolve with the protoplanetary disks, it is natural to expect that the observed diversity of the exoplanets and the PPDs are tightly

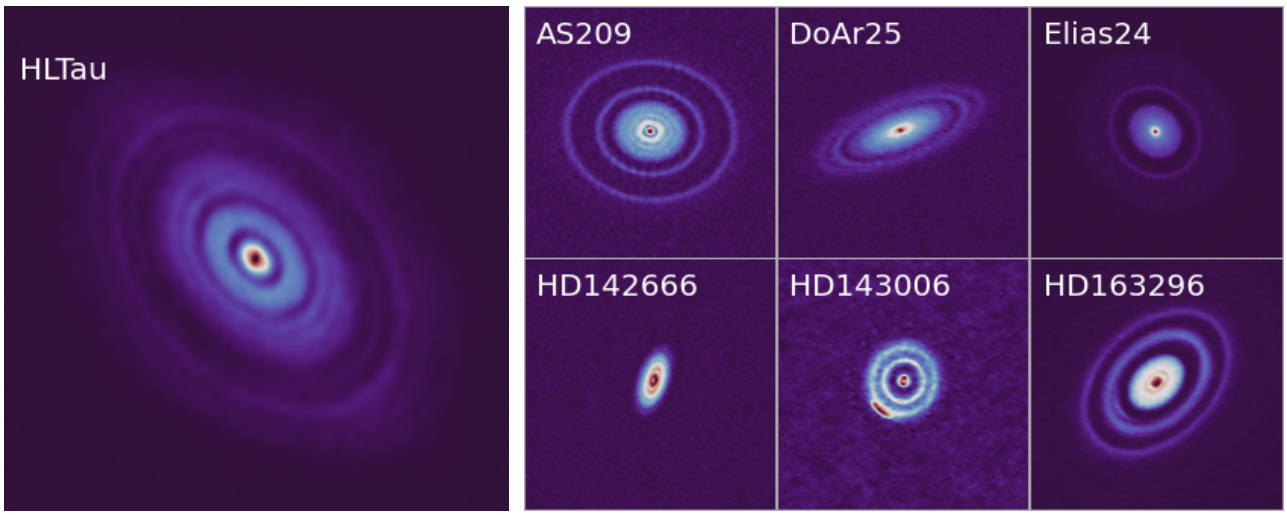

(a) (b)

Figure 1.2: Disk substructures resolved on (a) the HL Tau disk and (b) six nearby protoplanetary disks observed by ALMA. Images plotted using data provided by ALMA and the DSHARP project (Andrews et al., 2018).

connected. The connection between the two is mainly studied and discussed in two contexts: the primordial configurations of the planetary systems embedded in PPDs, and how the planets interact and evolve with the disk and after the disk dispersal. The former involves identifying the planetary signatures as well as extracting orbital/mass information of the planets from the disk observation; the latter requires one to quantitatively understand the physical interactions between planets and the hosting disk, with respect to different planetary and disk parameters. The planetary population synthesis model (e.g., Ida & Lin, 2004; Mordasini et al., 2009) has constructed sophisticated evolution model to connect the overall properties of the PPDs, such as mass, size, temperature profile, etc., to the diverse exoplanetary population. However, their synthesised planetary population strongly depends on the formation model of the planetesimals, which remains to be verified observationally. In order to have a more robust inference of the initial planetary configurations, we need to bypass this fundamental uncertainty by obtaining more direct evidence of the embedded planets inside the PPDs.

In 2015, the Atacama Large Millimeter Array (ALMA) made the breakthrough by spatially resolving the HL Tau disk down to a few au scale (Brogan et al., 2015) and successfully identifying the ring/gap substructure on the dust continuum image (Figure 1.2a). Such a structure is commonly believed to be the traits of the embedded planets, as theories have long predicted that a planet embedded in a disk can open a surface density gap in the disk once it is sufficiently massive (e.g., Lin & Papaloizou, 1979; Goldreich & Tremaine, 1980; Crida et al., 2006). Since then, various substructures in PPDs have been identified by the follow-up studies, including the gap/ring (e.g., Cieza et al., 2017; Huang et al., 2018a; Kanagawa et al., 2021), spiral arms (e.g., Wölfer et al., 2021; Xie et al., 2021), and inner cavities (e.g., Dong et al., 2018b; Kudo et al., 2018; Hashimoto et al., 2021). The follow-up project with particular focus on the disk substructures, namely Disk Substructures at High Angular Resolution Project (DSHARP), has already released continuum data for 20 nearby disks (Figure 1.2b). While alternative interpretations about

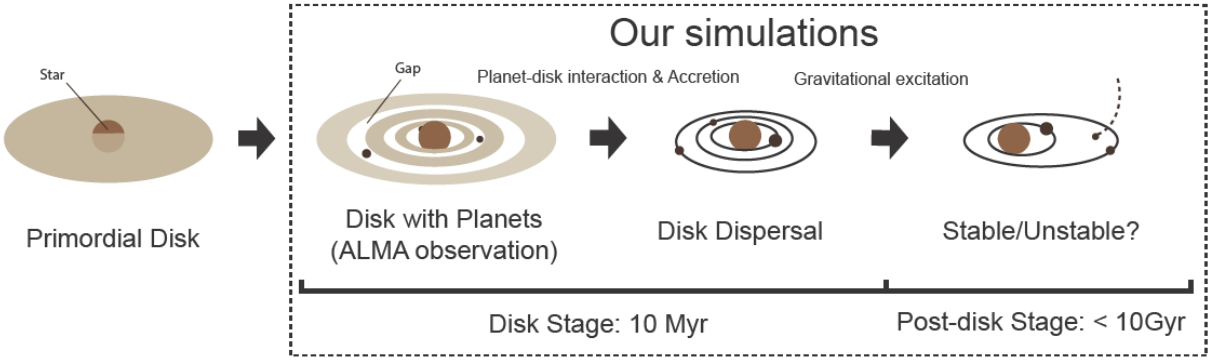

Figure 1.3: Schematic flow of the planetary evolution from disks to the currently observed architecture.

the substructures are possible, planets remain as one of the most conventional and popular interpretations.

Following the planetary interpretation, the orbital semi-major axis and the mass of the hidden planets can be inferred from the location and width of the gap, respectively. More specifically, the planetary masses can be predicted using the scaling relations between the gap width and planetary mass suggested by the numerical simulations (Kanagawa et al., 2015, 2016; Rosotti et al., 2016; Dong & Fung, 2017; Zhang et al., 2018). In turn, the primordial architectures of planetary systems hosted by those disks can then be fairly well constrained by the observed gap/ring substructures, and then serve as initial conditions for its future evolution.

To investigate the evolution outcome of the planetary systems deduced from those disks, both planet-disk interaction and accretion effects have to be carefully addressed. Since the observed protoplanetary disks are generally young, it is reasonable to expect that those embedded planets will evolve together with the disk throughout the disk lifetime. A planet embedded in a PPD exchanges angular momentum with the disk by exciting density waves, and thus changes its orbit, or migrates(Goldreich & Tremaine, 1979, 1980). In the course of migration, the planet also accretes the surrounding dust and gas from the disk and grows in mass. As a result, the architecture of the planetary systems are expected to be strongly shaped by both migration and accretion for the rest of the disk lifetime. Thus the resulting configuration may differ significantly from what has been currently observed(predicted) from the PPDs.

After the dispersal of the disk, the dynamical structure of the planetary systems continues evolving via gravity, and the long-term orbital stability of planetary systems depends on the configurations in terms of masses, orbital separations and mean-motion resonance states that are tightly connected with the evolution at the disk stage. Convergent migration at the disk stage force planets naturally enter a chain of resonance, therefore stabilise the planetary systems against small perturbations. On the other hand, strong migration and accretion may result in closely packed planetary system at the end of the disk stage, causing the subsequent orbital evolution to be chaotic due to the overlapping of the resonance zones. Together with the perturbative forces may eventually leads to orbital instabilities such as planet-planet scattering. It then poses a need to examine their long-term stability by performing numerical integration after the disk dispersal.

With the aforementioned motivations, this thesis aims to

1. extract the realistic initial configurations of planetary systems from the protoplanetary disk observation,
2. investigate the evolution the planetary system with the PPD based based on the initial conditions deduced from the disks, and
3. examine the long term orbital stability of the evolved planetary systems after the disk dispersal.

The schematic flow of the numerical approach is shown by Figure 1.3.

We begin our investigation by applying our evolution model to the well-known HL Tau system (Wang et al., 2020). However, it is unknown that to what extent the conclusion that we draw from the HL Tau system is also applicable to other protoplanetary disks, which implies the necessity to expand our sample size to a variety of the PPDs. We then generalise our result of HL Tau by applying our evolution model to other ALMA disks. We first develop the mass criteria for self-consistency and improve the mass predictions of planets in 35 ALMA disks by differentiating the gaps into the respective groups (Wang et al., 2021a). Based on the planetary mass predictions, we systematically investigate the evolution outcome of 12 multi-planetary systems out of ALMA disks with additional numerical implementations (Wang et al., 2021b). Our goal is to statistically understand the architecture of the planetary systems out of the disks with comparison to the observed population, and the general orbital stability of these configurations.

The rest of the thesis is organised as follows. In Chapter 2, we briefly review the PPD observation, followed by the theoretical modelling of the PPD structure and evolution. We then briefly review how planets interact with PPDs, including the formation, mass accretion and orbital migration. In Chapter 3, we show the evolution results of the HL Tau system. In Chapter 4, we developed the mass criteria and improve the planetary mass predictions by apply the criteria to 35 ALMA disks. In Chapter 5, we present the disk evolution results of the 12 ALMA disk with multi-gap structure as well as the long-term orbital stability under different strengths of perturbative forces. Finally we summarises the conclusions and discuss the future prospects of our results in Chapter 6.

Chapter 2

Review on observation and theoretical modelling of protoplanetary disks with planets

In this chapter, we present a short review of the studies that are relevant to this thesis. We first give an overview of the exoplanet and PPD observation. Then we introduce the theoretical modelling of the PPD, including the structure, radial profiles and viscous evolution. Finally we have a short review on the most important interactions between the planet and the disk, namely the planetary mass accretion and orbital migration processes.

2.1 Overview of exoplanet and disk observation

2.1.1 Exoplanet observation

Since the discovery of the first exoplanet around the pulsar PSR 1257+12 in 1992 (Wolszczan & Frail, 1992), more than 5,000 exoplanets have been detected in the recent three decades, thanks to the evolution of the exoplanet observing techniques. The exotic but interesting properties unveiled by the increasing number of detected exoplanets also have far reaching implications on the theoretical modelling of the planetary formation and evolution. In this subsection, we first give a short introduction to the planet detection techniques, followed by a brief review of the the statistical properties of the currently observed planets. The following review basically follows Wright & Gaudi (2013) and Winn & Fabrycky (2015).

Conceptually, detection of an exoplanet requires one to identify the observables that implies the presence of the planet. The main techniques include the radial velocity (RV) method, transits, imaging, timing, and gravitational microlensing. Except the imaging method that directly identify the signal from the planet, all other techniques detect the planet indirectly from the observables of the hosting star. The details of each method are summarise below.

- **The RV method**: a star wobbles around the centre of mass due to the orbital movement of its planetary companion, and such an effect is reflected by the change radial velocity of the star. The RV curve contains the information of the orbital period, radius and eccentricity. Technically, measuring of RV is achieved by performing high-precision Doppler measurement of the spectroscopic emission.

- **Transit**: for a star with a planetary companion, each time the planet is transiting in front of the star, it blocks the radiation of the star and causes a temporary dip of the stellar flux, which can be revealed by photometry. Based on the photometric data obtained by the *Kepler* mission, the transit method contributes to the discovery of most planets smaller than Neptune.

- **Imaging**: imaging directly detects the planet by identifying the electromagnetic emission from the planet, including both reflection of the stellar radiation and the thermal radiation of the planet. The latter also contains the information of the planet's constitution.

- **Timing**: The presence of a planet around the hosting star or stellar remnant (e.g., pulsars and eclipsing binaries) changes the periodic behaviour of its host, such as the pulsation periods. The concept of the timing method is similar to the RV method. The first exoplanet was detected using this method.

- **Gravitational microlensing**: when a foreground star is aligned with a background star in the line of sight, its gravity bends the light like a lens, and the image of the background star is magnified. If the foreground star has a planet orbiting around, the movement of the planet may create a perturbation (a spike) of the magnification by breaking the symmetry of the microlensing event.

Each of the planet detection technique has its own bias, intrinsically due to its respective sensitivity. Both the RV method favours inner planet and massive planet, because its signal-to-noise ratio scales with $M_p a^{-1/2}$, where M_p is the planetary mass and a is the semi-major axis. Similarly, the transit probability is inversely proportional to the semi-major axis, and its signal-to-noise ratio also scales with $R_p^2 a^{-1/2}$, where R_p is the planetary radius. While the direct imaging method is not only sensitive to the inner planet, it favours hot and large planets, which means distant low-mass planets are still out of its detectability. The microlensing method, however, has a complicated sensitivity as it is less analytically characterisable.

Considering the fact that so far the majority of the exoplanets were discovered using RV and transit (e.g. *Kepler*) methods, the overall distribution of the observed exoplanetary population is inevitably biased towards the massive (large) and close-in planets. Having said so, Figure 1.1 shows the current observed exoplanetary population still covers a significantly wide range of the semi-major axis ($10^{-2}\,\mathrm{au}$ to $10^{2}\,\mathrm{au}$) and planetary mass ($10^{-4}\,\mathrm{M_J}$ to $30\,\mathrm{M_J}$), over a few orders of magnitude. Overall the observed population can be roughly divided into four groups. The Neptune-like planets and earth-like terrestrial planets dominate the total population at the lower left corner, with mass below $0.1\,\mathrm{M_J}$ and semi-major axis ranging from $0.01\,\mathrm{au}$ to $1\,\mathrm{au}$. The giant planets larger than $0.1\,\mathrm{M_J}$ can be divided into two groups: the hot Jupiters at the upper left corner with semi-major axis $< 0.1\,\mathrm{au}$, and others that are relatively further away ($\sim 1\,\mathrm{au}$) from the star. Particularly,

the division between the two separate populations of the giant planets still remains as an intriguing question.

The occurrence rate, defined as the the mean number of planets per star, also differ with respect to different groups of planets: around 10% of the Sun-like star host giant planets with orbital period smaller than a few years, and this percentage increases to 50% for smaller planets between $1\,\mathrm{M}_\oplus$ and $4\,\mathrm{M}_\oplus$. Particularly, the occurrence rate for brown dwarfs ($> 10\,\mathrm{M}_\mathrm{J}$) within the period of a few years is very low as compared with lower mass planets. Within the same group, the occurrence rate also depends on the semi-major axis: for example, the occurrence rate for small planet drops quickly when the period smaller than ten days.

The current exoplanet observation, particularly the *Kepler mission*, also reveals many systems hosting multiple planets. The period ratios of the adjacent planet pairs exhibits a wide distribution: the majority of the period ratios are in range $1.5 - 5.0$ with a peak at 2.0, while there is a long tail extending to 100. The number of pairs also decreases sharply below the 1.5 period ratio. It was also observed that the giant planets are more frequently found in mean-motion resonances, with period ratios not at the exact resonance but slightly deviating from the exact integer number.

2.1.2 Protoplanetary disk observation

Observation on PPDs is strongly motivated by the fact that these circumstellar disks are the birthplaces of planets. Measuring the properties of their structure, such as mass, size, surface density and temperature, is of crucial importance to understand the formation, evolution and final configuration of planets that are born within. In this subsection, we first present a brief overview the current PPD observation, and then focus on the observation on disk substructures, which are the most relevant to this thesis. The following review is mainly based on Brogan et al. (2015), Andrews et al. (2018) and Andrews (2020).

The PPD observation mainly relies on three different observational tracers: the scattered light, spectral line emission and dust continuum emission. The scattered light is the reflection of the star radiation produced by the micron-size dust particles. The resolution of the scattered light observation can be as high as 30 to $50\,\mathrm{mas}$ ($\sim$5 au at the standard distance $150\,\mathrm{pc}$) for a 8 to $10\,\mathrm{m}$ telescope, however it is not available for the inner disk region due to the poor contrast with the host star. The spectral line emission is available for molecules with permanent dipole moment (e.g. CO line emission), line intensity of which can be used to estimate the gas surface density of the disk, if the relative abundance of the emitting gas is known.

The dust continuum emission is the the most important tracer in revealing the fine substructures of the disk. It is the thermal emission of the dust with broad wavelengths ranging from $\mu\mathrm{m}$ to cm. At sub-millimetre wavelength, it is optically thin and thus has high brightness and resolution up to 10 to $20\,\mathrm{mas}$, around $2\,\mathrm{au}$ at the standard distance. The high resolving power of the dust continuum emission directly contributes to the discovery of the ring/gap substructures on HL Tau.

Although many of PPDs have already been discovered, robust knowledge about the demographic details of the currently observed disks is still limited, as large uncertainties

and assumptions are involved in the process of determining the principal properties of the disk. The dust mass of the disk is indirectly estimated from the luminosity of the mm emission, and the gas mass of the disk is estimated from the spectral line emission, such as HD and CO measurement. In case the spectral line observation is not available, the gas mass is instead estimated from the dust mass by assuming a constant dust-to-gas ratio. The current data comprising of 887 disks show that the solid mass of PPDs is from $0.1\,\mathrm{M}_\oplus$ to a few hundreds of $M_\oplus$.

The size of PPDs, or the effective size, is measured empirically by setting a lower fraction limit for the luminosity of the tracer. At 90 % threshold, the radii of around 200 disks range from 10 au to 500 au at mm wavelength, while the radius inferred from the CO line emission is roughly 2.5 times as large as that in mm-size, implying that the gas disk is more extended than the dust disk.

ALMA observation on disk substructures

The ALMA telescope consists of 66 high-precision radio antennas and has unprecedented sensitivity and resolving power at sub-millimetre wavelength. ALMA began its operation in 2012, and its groundbreaking observation on HL Tau started from October 14 and lasted for one month. HL Tau is a young star in the Taurus star-forming region at a mean distance of 140 pc, with a mass estimated from $0.55\,\mathrm{M}_\odot$ to $1.2\,\mathrm{M}_\odot$. HL Tau is located in a molecular ridge visible in ^{13}CO emission, which causes the strong extinction and therefore poor detectability at the optical band. At millimeter wavelength there is much less extinction effects, and its high brightness has attracted a huge amount of observational interests in the past. The continuum was observed in Band 3 (2.9 mm or 101.9 GHz), Band 6 (1.3 mm or 233 GHz) and Band 7 (0.87 mm or 343.5 GHz).

The high resolution continuum image later released by ALMA clearly revealed the concentric ring structure on HL Tau in all three observed bands (Brogan et al., 2015). In total there are seven "bright rings" (hereafter ring) and "dark rings" (hereafter gaps) that appears in an alternate manner, and their semi-major axis ranges from 13.2 au to around 97 au. Among the seven gaps, there are three major gaps at 13.2 au, 32.3 au and 73.7 au, where the dust has depleted for at least a factor of ten Pinte et al. (2015). The rest of the gaps are relatively shallow and narrow as compared with the three major ones. Followed up studies (e.g., Dipierro et al., 2015; Jin et al., 2016) also confirmed that the morphology of the HL Tau gaps can be reproduced by three giant planets.

The success of ALMA in observing the disk substructure in the HL Tau disk suggests the possibilities of existence of similar substructure on other nearby disks. As one of the initial Large Programs in ALMA, the followed up DSHARP project was then conducted to survey, resolve, and characterise the disk substructures on 20 nearby disks that are the brightest and most massive ones (Andrews et al., 2018). The DSHARP observation uses the optimal ALMA Band 6 (240 GHz) with an expected resolution down to 5 au (comparable to the gas scale height) and $\sim$ %10 contrast at 40 au scale, meaning it is capable of resolving both the fine structure of the disk and faint substructure at the outer disk, including small perturbation of the gas profile due to a low-mass planet and weak votices. The actual observation took place in 2017 from May to November.

The results of DSHARP observation are fruitful: various disk substructures have been observed on most of the disks, including annular ring/gap substructure (Huang et al., 2018a), spiral structure Huang et al. (2018b); Kurtovic et al. (2018), bright arc and a misaligned inner disk (Pérez et al., 2018), and the interpretations of the substructures are also summarised in a series of papers (e.g., Zhang et al., 2018). Particularly, 90% of the disks exhibit ring and gap substructure similar to that in the HL Tau disk, with a diverse distribution of locations and width. A few of annular substructures are associated with spiral arms that are potentially generated by massive planets. In addition to the DSHARP project, recent studies Long et al. (2018a) and van der Marel et al. (2019) also found similar structures by analysing the archive data of ALMA. The abundance of the disk substructure discovered indicates that these substructures may have a ubiquitous origin, and planet is one of the most promising answers.

2.2 Theoretical model of protoplanetary disks

The PPDs are disk-structured objects around young stars with lifetime of a few million years. The PPD is mainly composed of dust and gas, which structure can be well described by the model based on quasi-equilibrium state. The structure of the PPD strongly shapes the migration and accretion of the planets that form inside the disk; in addition, since the evolution of PPD tightly couples with its structure as well, both the structure and evolution of the disk deserve equal attention while the overall influence on the evolution path of the planet is considered. The review in this subsection generally follows Armitage (2009) and Naruse et al. (2015).

2.2.1 Gas structure

While considering the structure of the disk, we adopt the approximation that the disk evolves axisymmetrically and slowly enough that the quasi-equilibrium state can be applied at any instant. Starting from the assumptions, we will mainly consider the vertical structure, radial structure and temperature profile of the disk. We use the cylindrical coordinate system (R, z) centered at the star and align the z-direction with the total angular momentum. We define $T(R, z)$, $\Omega(R, z)$ and $\mathbf{v} = (v_R, v_\phi, v_z)$ to be the temperature, angular velocity and velocity of the gas, and use the subscript 'dust' to distinguish the respective quantities that associate with the dust from those that associate with the gas. We also define $\rho(R, z)$ and $\Sigma(R)$ to be the density and surface density. Particularly, the density and surface density of the gas are denoted as ρ_g and Σ_g to avoid any confusion.

Vertical gas structure

The vertical structure of the PPD can be derived by considering the hydrostatic equilibrium, that is, the balance between the gravitational force exerted by the star and the gas pressure. In order to proceed, three further assumptions have to be introduced:

(i) the disk is vertically isothermal,

(ii) the disk is not self-gravitational, i.e., the disk mass to the stellar mass ratio is much smaller than unity, and

(iii) the disk is geometrically thin.

If we assume irradiation from the star is the only source to heat up the disk, the temperature of the disk is only a function of the cylindrical distance to the star, and thus the first assumption is reasonable. The second assumption ensures that the star is the only source of the gravity which shapes the disk. Finally, the third assumption ensures that the hydrostatic equilibrium is valid as generally pressure inside a disk is small due to the large surface to volume ratio of the disk that favors effective cooling. Therefore, geometrically-thick disks cannot balance the gravity by the gas pressure and only thin disks are relevant to the later discussion.

If the hydrostatic equilibrium is assumed, we can write down the following equation considering the balance between the gravity and the pressure:

$$\begin{aligned}\frac{1}{\rho_g}\frac{dP}{dz} &= \frac{-\mathcal{G}M_*}{R^2+z^2}\sin\theta,\\ \frac{dP}{dz} &= \frac{-\mathcal{G}M_*}{R^2+z^2}\frac{z}{(R^2+z^2)^{1/2}}\rho_g,\\ &= \frac{-\mathcal{G}M_* z}{(R^2+z^2)^{3/2}}\rho_g,\end{aligned} \tag{2.1}$$

where $\mathcal{G}$ is the gravitational constant, P is the gas pressure, and M_* is the mass of the star. From the isothermal equation of state, we have $P = \rho_g c_s^2$, where c_s is the sound speed. Substituting to equation (2.1), one obtains

$$c_s^2\frac{d\rho_g}{dz} = \frac{-\mathcal{G}M_* z}{(R^2+z^2)^{3/2}}\rho_g. \tag{2.2}$$

Integration of equation (2.2) gives

$$\begin{aligned}\int\frac{d\rho_g'}{\rho_g'} &= -2\frac{\mathcal{G}M_*}{c_s^2}\int\frac{z'dz'}{\left(R^2+z'^2\right)^{3/2}}\\ \ln\rho_g(z) &= \frac{\mathcal{G}M_*}{c_s^2}\frac{1}{(R^2+z^2)^{1/2}}\end{aligned} \tag{2.3}$$

at $z=0$,

$$\rho_g(z=0)\equiv\rho_{g,0} = \exp\left(\frac{\mathcal{G}M_*}{Rc_s^2}\right). \tag{2.4}$$

Given $z \ll R$, we can expand the right hand side of equation (2.3) and take the leading term

$$\begin{aligned}\ln\rho_g(z) &\approx \frac{\mathcal{G}M_*}{Rc_s^2}\left[1-\frac{1}{2}\left(\frac{z}{R}\right)^2\right]\\ \rho_g(z) &= \rho_{g,0}\exp\left(-\frac{\mathcal{G}M_*}{2R^3c_s^2}z^2\right).\end{aligned} \tag{2.5}$$

Given the Keplerian orbital velocity at the mid-plane $\Omega_K \equiv \sqrt{\mathcal{G}M_*/R^3}$, we define h as the scale height that takes the form

$$h \equiv \frac{c_s}{\Omega_K}. \tag{2.6}$$

Equation 2.5 can then be re-expressed in the scale height as

$$\rho_g = \rho_{g,0} \exp\left(-z^2/2h^2\right), \tag{2.7}$$

and $\rho_{g,0}$ is the gas density at the mid-plane. We can further express the mid-planet surface density as $\Sigma_g = \int_{+\infty}^{-\infty} \rho dz$ and obtain the following relation for $\rho_{g,0}$ and Σ_g:

$$\rho_{g,0} = \frac{1}{\sqrt{2\pi}} \frac{\Sigma_g}{h}. \tag{2.8}$$

Equation (2.7) shows that the vertical density profile follows the Gaussian distribution. At a range where z/h is around unity, even the full treatment which does not assume condition $z \ll R$ produces a density ρ_g that only deviates slightly from the Gaussian profile. Although there exist other factors which can cause significant deviation from the Gaussian profile, such as the non-isothermal temperature profile, magnetic pressure(e.g Hirose & Turner (2011)), etc., the detailed discussion of these effects is beyond the scope of this review.

Radial gas structure

Compared to the relatively trivial derivation of the vertical density profile, the radial density profile of the disk involves detailed considerations of the transport of the angular momentum and therefore will be discussed later in Section 2.2.3. Nevertheless, when the surface density Σ_g and temperature T distribution are known, the orbital velocity of the gas $v_{\phi,gas}$ at the mid-planet can be derived from the Euler equation by considering force balance in the radial direction

$$\frac{\partial \mathbf{v}}{\partial t} + (\mathbf{v} \cdot \nabla)\mathbf{v} = \frac{1}{\rho_g}\nabla P - \nabla\Phi, \tag{2.9}$$

where ϕ is the gravitational potential. Since we are interested in the steady state of the disk, $\partial/\partial t \equiv 0$. Taking only the radial component of equation (2.9), we have

$$\frac{v_\phi^2}{R} = \frac{\mathcal{G}M_*}{R^2} + \frac{1}{\rho_g}\frac{dP}{dR}. \tag{2.10}$$

Assuming $\Sigma_g \propto R^\gamma$ and $T \propto R^\beta$ and using the relations:

$$c_s^2 \propto T, \tag{2.11}$$

$$\rho_g \propto \frac{\Sigma_g}{h}, \tag{2.12}$$

we get

$$P \propto R^{\gamma - \frac{3-\beta}{2}} \propto R^n, \tag{2.13}$$

where we define $n \equiv \gamma - \frac{3-\beta}{2}$. Substitute the expression of P into equation 2.10 and define the mid-planet Keplerian speed as $v_K \equiv \Omega_K R \equiv \sqrt{\mathcal{G}M_*/R}$, the final result is

$$\frac{v_\phi^2}{R} = \frac{v_K^2}{R} + \frac{c_s^2}{P}\frac{dP}{dR}, \tag{2.14}$$

Hence, we can obtain v_ϕ as

$$\begin{aligned} v_\phi &= v_K \left[1 + n\frac{c_s^2}{v_K^2}\right]^{1/2}, \\ &= v_K \left[1 + n\left(\frac{h}{R}\right)^2\right]^{1/2}. \end{aligned} \tag{2.15}$$

It can be concluded here that the difference between the gas speed v_ϕ and Keplerian speed v_K is in the order of square of h/R. Although this deviation is only a tiny fraction of the Keplerian speed(for example, when $n = -3$ and $[h/R]_{R=1\,\mathrm{au}} = 0.05$, the fractional difference $(v_K - v_\phi)/v_K$ is $0.4\,\%$), this difference is vitally important in considering the growth of particles inside the disk: since large particles orbit at Keplerian speed, they will experience a headwind while moving inside the sub-Keplerian disk, therefore losing angular momentum due to the viscous drag and moving inwards in a spiral.

The above derivation is only applicable to calculate the Keplerian speed deviation at the mid-plane. At places off the mid-plane, the angular velocity should also depend on the vertical distance z. More detailed calculation (e.g., Takeuchi & Lin, 2002) shows that near the mid-plane region below $z \sim 1.48h$, particles rotate faster than the gas and therefore experience a headwind; at elsewhere, particles rotate slower than the gas.

2.2.2 Temperature profile and vertical geometry

To investigate the temperature profile of the PPD, one may assume that the PPD is in thermal equilibrium, and what remains is to find the temperature at which the energy gain and loss balance out each other. There are mainly two sources that the PPD can gain thermal energy from: the irradiation from its hosting star and the gravitational energy released by the accretion matter. On the other hand, the PPD also loses energy through re-emission process. In the following derivation we will start from a simplified disk model, which is the razor-thin and passive disk. If the disk energy income can be solely determined by the irradiation from the hosting star, the disk is called "passive" and thus the temperature profile will be determined by its geometrical shape. A razor-thin disk will then ensure that the mid-plane of the disk intercept all the radiation and then re-emit in black body spectrum.

Consider a star in radius R_* with a constant stellar surface brightness I_*. Let θ and ϕ be the polar and azimuthal angles. If we write the unit vector $\hat{\mathrm{n}}$ of the light direction as

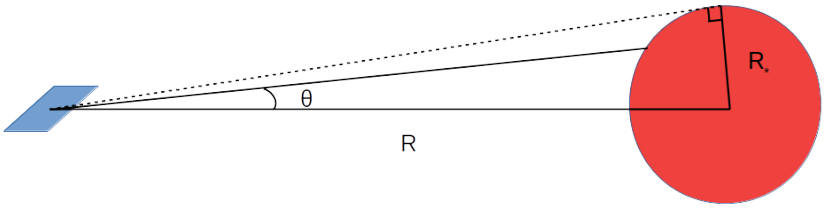

Figure 2.1: Illustration of the flux from the star.

$(\sin\theta\cos\phi, \sin\theta\sin\phi, \cos\theta)$, then the light flux F can be expressed as

$$\begin{aligned} F &= \int I_*(\hat{\mathbf{n}}\cdot\hat{\mathbf{x}})d\Omega \\ &= \int I_* \sin^2\theta\cos\phi d\theta d\phi. \end{aligned} \tag{2.16}$$

Since only half of the star can contribute to the total flux, equation (2.16) is integrated over $0 < \theta < \sin^{-1}\left(\frac{R_*}{R}\right)$ and $-\pi/2 < \phi < \pi/2$ and we obtain

$$\begin{aligned} F &= I_* \int_{-\pi/2}^{\pi/2} \cos\phi d\phi \int_0^{\sin^{-1}(R_*/R)} \sin^2\theta d\theta \\ &= 2I_* \left[\frac{1}{2} - \frac{1}{4}\sin 2\theta\right]_0^{\sin^{-1}(R_*/R)} \\ &= I_* \left[\sin^{-1}\left(\frac{R_*}{R}\right) - \frac{R_*}{R}\sqrt{1-\left(\frac{R_*}{R}\right)^2}\right]. \end{aligned} \tag{2.17}$$

The brightness of the star at its surface can be related to the effective temperature of the starby using the Stefan-Boltzmann law (Rybicki & Lightman, 1979)

$$I_* = \frac{F}{\pi} = \frac{\sigma T_*^4}{\pi}. \tag{2.18}$$

For one side of the disk, the flux $F = \sigma T^4$. Substituting back to both sides of the equation (2.17) gives

$$\left(\frac{T}{T_*}\right)^4 = \frac{1}{\pi}\left[\sin^{-1}\left(\frac{R_*}{R}\right) - \frac{R_*}{R}\sqrt{1-\left(\frac{R_*}{R}\right)^2}\right]. \tag{2.19}$$

In the region far from the star, i.e., $R_* \ll R$, equation (2.19) is reduced to a simple power law temperature profile

$$T \propto R^{-3/4}. \tag{2.20}$$

Using the relation $c_s^2 \propto T$ and $h \equiv c_s/\Omega_K$, the aspect ratio is

$$\frac{h}{R} \propto R^{-\frac{3}{4}\cdot\frac{1}{2}+\frac{3}{2}-1} \propto R^{1/8}. \tag{2.21}$$

Defining the flaring index f through $(h/R) \propto R^f$, the temperature profile for a razor-thin, passive disk gives $f = 1/8$. This shows that when R increases, the aspect ratio also increases, resulting in a disk called 'flared'.

The above result is over-simplified in many aspects. At large R, the flared part of the disk contributes to additional absorption area and therefore gaining higher temperature than the originally-assumed razor-thin disk. The full solution that takes account of the flaring effect can be derived in a similar way, but a simplified consideration that takes the limit $R_* \ll R$ and the star to be a point source is sufficient to understand the effect qualitatively.

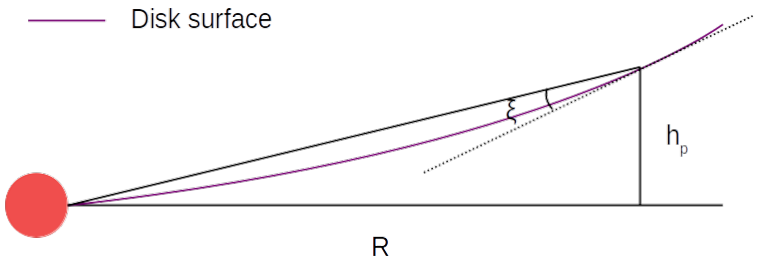

Figure 2.2: Illustration of a flared disk.

Following the arguments in Armitage (2009), we define a maximum absorption height h_p at radius R and then define ξ as the angle between the incoming radiation and the tangent of the local disk surface:

$$\xi \equiv \frac{dh_p}{dR} - \frac{h_p}{R}. \tag{2.22}$$

ξ is determined by the relation between h_p and scale height h. Assuming black-body emission, we can equate the local heating rate(left-side) and the cooling rate(right-side) as

$$\xi \left(\frac{L_*}{4\pi R^2}\right) = \sigma T^4. \tag{2.23}$$

Using $L_* = 4\pi R_*^2 \sigma T_*^4$, we obtain

$$\left(\frac{T}{T_*}\right)^4 = \xi \left(\frac{R_*}{R}\right)^2, \tag{2.24}$$

$$T \propto \xi^{1/4} R^{-1/2}. \tag{2.25}$$

This shows that at large radii the temperature of a flared disk drops slower than that of a razor-thin disk, as R increases(c.f. equation (2.21)).

2.2.3 Viscous evolution

The PPD evolves as the gas keeps accreting onto the central star, whereas the disk wind launched by the magnetic field and photoevaporation effect continues to cause the mass loss. The movement of the gas is governed by the gain and loss of the angular momentum. Therefore, the key idea to understand the evolution of the PPD is to understand how the angular momentum is transferred and redistributed within the disk. Starting from the basic conservation laws, we can write the hydrodynamical equations in the context of the PPD and then obtain various characteristics of the disk evolution. The following review mainly follows Pringle (1981).

Classical picture

The classical picture of the disk evolution concerns the evolution of a vicious, axisymmetric and geometrically-thin disk. Construct the cylindrical coordinate system (R, z) as before, the conservation of mass and angular momentum can be written as

$$R\frac{\partial \Sigma_g}{\partial t} + \frac{\partial}{\partial R}(R\Sigma_g v_R) = 0 \tag{2.26}$$

$$R\frac{\partial}{\partial t}(R^2\Omega\Sigma_g) + \frac{\partial}{\partial R}(R^2\Omega \cdot R\Sigma_g v_R) = \frac{1}{2\pi}\frac{\partial G}{\partial R}. \tag{2.27}$$

Compared with equation (2.9), equation (2.27) is derived from the Navier-Stokes equation which also takes account of the viscosity. G on the right side of the equation (2.27) is the vicious torque that acting on the edge of the annulus:

$$G = 2\pi R \cdot \nu\Sigma_g R\frac{d\Omega}{dR} \cdot R, \tag{2.28}$$

where ν is the kinematic viscosity. From equation (2.26) we have

$$\frac{\partial \Sigma_g}{\partial t} = -\frac{1}{R}\frac{\partial}{\partial R}(R\Sigma_g v_R). \tag{2.29}$$

Substituting equations (2.29) and (2.28) to equation (2.27) and use prime to denote $\frac{d}{dR}$, then

$$-R^2\Omega\frac{\partial}{\partial R}(R\Sigma_g v_R) + R\Sigma_g\frac{\partial}{\partial t}(R^2\Omega) + \frac{\partial}{\partial R}(R^2\Omega \cdot R\Sigma_g v_R) = \frac{\partial G}{\partial R}, \tag{2.30}$$

$$R\Sigma_g\frac{\partial}{\partial t}(R^2\Omega) + R\Sigma_g v_R\frac{\partial}{\partial R}(R^2\Omega) = \frac{\partial}{\partial R}(v\Sigma_g R^3\Omega'). \tag{2.31}$$

Since $\frac{d}{dt} \equiv \frac{\partial}{\partial t} + v_R\frac{\partial}{\partial R}$,

$$R\Sigma_g\frac{dR}{dt}(R^2\Omega)' = \frac{\partial}{\partial R}(v\Sigma_g R^3\Omega'), \tag{2.32}$$

$$R\Sigma_g v_R = \frac{1}{(R^2\Omega)'}\frac{\partial}{\partial R}(v\Sigma_g R^3\Omega'). \tag{2.33}$$

Substituting equation (2.33) back to equation (2.29),

$$\frac{\partial \Sigma_g}{\partial t} = -\frac{1}{R}\frac{\partial}{\partial R}\left[\frac{1}{(R^2\Omega)'}\frac{\partial}{\partial R}(v\Sigma_g R^3\Omega')\right]. \tag{2.34}$$

Using Keplerian $\Omega \propto R^{-3/2}$,

$$\frac{\partial \Sigma_g}{\partial t} = \frac{3}{R}\frac{\partial}{\partial R}\left[R^{1/2}\frac{\partial}{\partial R}(v\Sigma_g R^{1/2})\right], \tag{2.35}$$

and the radial velocity is given by

$$v_R = -\frac{3}{\Sigma_g R^{1/2}}\frac{\partial}{\partial R}\left(\nu\Sigma_g R^{1/2}\right). \tag{2.36}$$

The above result describes the diffusion of the gas. Additional terms need to be considered if other sources of mass loss(e.g. thermal wind) or external torques are present. In the case of the extra mass loss $\dot{\Sigma}_{g_{ext}}$, equation (2.35) simply becomes

$$\frac{\partial \Sigma_g}{\partial t} = \frac{3}{R}\frac{\partial}{\partial R}\left[R^{1/2}\frac{\partial}{\partial R}(v\Sigma_g R^{1/2})\right] + \dot{\Sigma}_{g,ext}. \tag{2.37}$$

With the presence of the radial flow v_{ext} driven by external torque, it becomes

$$\frac{\partial \Sigma_g}{\partial t} = \frac{3}{R}\frac{\partial}{\partial R}\left[R^{1/2}\frac{\partial}{\partial R}(v\Sigma_g R^{1/2})\right] - \frac{1}{R}\frac{\partial}{\partial R}(R\Sigma_g v_{ext}). \tag{2.38}$$

We can define a new set of variables

$$X \equiv 2R^{1/2}, \tag{2.39}$$

$$f \equiv \frac{3}{2}\Sigma_g X, \tag{2.40}$$

to write equation (2.35) in a more enlightening way:

$$\frac{2}{3}\frac{\partial}{\partial t}\left(\frac{f}{X}\right) = 3\left(\frac{2}{X}\right)^2\frac{2}{X}\frac{\partial}{\partial X}\left[\frac{X}{2}\frac{2}{X}\frac{\partial}{\partial X}(\nu f/3)\right]. \tag{2.41}$$

Then trivial calculations give

$$\frac{\partial f}{\partial t} = \frac{12\nu}{X^2}\frac{\partial f^2}{\partial X^2}, \tag{2.42}$$

which is a diffusion equation with a diffusion coefficient $12\nu/X^2$. If a disk has a characteristic scale of ΔR, the diffusion time scale can be written as

$$\tau_\nu \sim \frac{(\Delta X)^2}{D} \sim \frac{(\Delta R)^2}{\nu}. \tag{2.43}$$

2.2.4 Solutions of the surface density Σ_g

Consider the steady-state of equations (2.26) and (2.27) as well as equation (2.28), then the time derivative will vanish and we obtain:

$$2\pi R\Sigma_g v_R \cdot R^2\Omega = 2\pi R^3 \nu\Sigma_g \frac{d\Omega}{dR} + C \tag{2.44}$$

where C is a constant of integration. The left-hand side of the equation can be re-expressed by realising that the accretion rate $\dot{M}$ is equal to $-2\pi R\Sigma_g v_R$:

$$-\dot{M}R^2\Omega = 2\pi R^3 \nu\Sigma_g \frac{d\Omega}{dR} + C. \tag{2.45}$$

To determine the value of the constant C, the boundary condition of Ω is needed. When $R = R_*$, i.e., at the surface of the star, the angular frequency Ω of the disk should be equal to that of the star Ω_*. In the region where $R \gg R_*$, Ω can be approximated by the Keplerian angular frequency $\Omega_K \propto R^{-3/2}$. Due to the discrepancy between Ω_* and Ω_K, it is expected that there must be a point at some R' where the viscous stress vanishes or $d\Omega/dR = 0$. In general R' is very close to R_*, and using this approximation, the value of C is

$$C \approx -\dot{M}R_*^2\Omega_*. \tag{2.46}$$

Substituting the equation (2.46)to equation (2.45) at the region where $\Omega \propto R^{-3/2}$, we have

$$-\dot{M}R^2\Omega = 2\pi R^3 \nu\Sigma_g \frac{d\Omega}{dR} - \dot{M}R_*^2\Omega_*, \tag{2.47}$$

$$3\pi R^2\Omega(\nu\Sigma_g) = \dot{M}\left(R^2\Omega - R_*^2\Omega_*\right), \tag{2.48}$$

$$\nu\Sigma_g = \frac{\dot{M}}{3\pi}\left(1 - \sqrt{\frac{R_*}{R}}\right). \tag{2.49}$$

If the region $R \gg R_*$ is considered, equation (2.49) becomes

$$\Sigma_g \approx \frac{\dot{M}}{3\pi\nu}. \tag{2.50}$$

This is the steady state solution of the surface density at large radii.

Shakura-Sunyeav α prescription

We may realise that the viscosity plays a central role in the angular momentum transport that takes place inside the disk, and thus it is important to understand the physics that contributes to the viscosity. One might think that the molecular collision is one of the sources. Denote such viscosity as ν_m, then ν_m is approximately given by λc_s, where λ is the mean free path and c_s is the sound speed. Since $\lambda = (n\sigma_m)^{-1}$, where n is the density and σ_m is the cross-section, if typical values $\sigma_m \approx 2 \times 10^{-15}\,\mathrm{cm}^2$ and $n = 10^{12}\,\mathrm{cm}^{-3}$ are used for $R = 10\,\mathrm{au}$, the viscous time scale given by equation (2.43) is

$$\tau_\nu \sim O(10^{13})\mathrm{yr}. \tag{2.51}$$

This time-scale is much longer than the lifetime of the protoplanetary disk, so the molecular viscosity alone cannot explain the total viscosity required.

It is widely recognised that the turbulence caused by the instabilities makes the major contribution to the viscosity, and to characterise it, we follow the prescription introduced by the paper Shakura & Sunyaev (1973), and define the dimensionless α parameter

$$\nu = \alpha c_s h. \tag{2.52}$$

It is possible to assume that the value of α is a constant, and by taking the power-law profile of the temperature $T \propto R^{\beta}$, the kinematic viscosity ν can be expressed as $\nu \propto r^{\gamma}$, where $\gamma = \beta + 3/2$.

2.3 Planetary accretion and orbital migration

In this section, we review the two most important interactions between the planet and the disk during the disk stage, namely the planetary mass accretion and the orbital migration. The planetary accretion process can be divided into two stages: when the planetary mass is below the pebble isolation mass, the planet undergoes the pebble accretion; once the planetary mass exceeds the pebble isolation mass, the pebble accretion terminates and the run away gas accretion is triggered. We then present a review of the orbital migration mechanism starting from the linear perturbation theory of the disk, the parameter dependence of the migration torque, followed by the two types of migration that depends on whether the gas gap is open.

2.3.1 The accretion model

Pebble accretion

Pebbles are defined as aerodynamically small particles with Stokes number roughly between $O(10^{-3})$ and order of unity (Ormel, 2017). The pebble accretion model bypasses several drawbacks involved in the application of the traditional planetesimal accretion model, such as the formation timescale of the planetesimals and strong negative feedback onto the accretion rate as the planet becomes massive. Here we follow Ormel (2017) and briefly review the physics of the pebble accretion by considering how the pebbles encounter and settle onto the planet.

Figure 2.3 shows a shearing box at the vicinity of a planet. A pebble is initially far away from the planet with the impact parameter b and approaching the planet at speed $v_\infty = v_{\rm hw} + 3/2\Omega_K b$. The first term is the headwind speed due to the difference of the gas speed and Keplerian speed; the second term is the Keplerian shear.

As the pebble particle approaches the planet, it is gradually attracted by the planet due to the gravity and coupled to the local gas due to aerodynamic friction. In order for the pebble to settle onto the planet, two conditions are necessary to be satisfied at the same time:

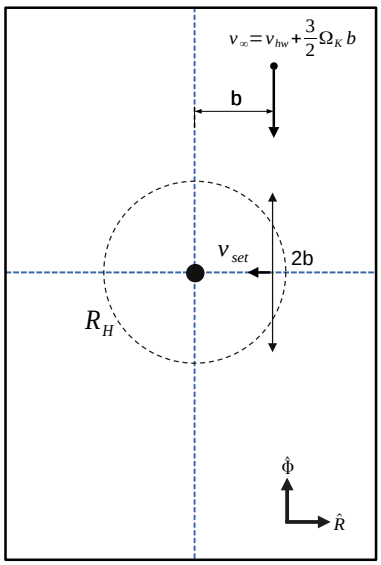

Figure 2.3: Illustration of how a pebble encounters with a planet within a shearing box that is co-rotating with the planet.

1. The time for the pebble to couple with the local gas (stopping time) should be less than the duration of the encounter;

2. The time for the pebble to settle onto the planet should be less than the duration of the encounter.

The timescales mentioned above are determined by the properties of the dust and planet, as well as the impact parameter b. The stopping time t_s of the pebble particle is related to the pebble size. The encounter happens when the pebble is most strongly influenced by the gravity of the planet, therefore its duration $t_{\rm enc}$ is estimated as $2b/v_\infty$. The settling time $t_{\rm set}$ depends on both the strength of the planetary gravity and the stopping time of the pebble particle. At the distance b, the pebble experiences the strongest gravitational acceleration $g = \mathcal{G}M_p/b^2$, which results in the characteristic settling speed $v_{\rm set} = gt_{\rm s}$ and the settling time $t_{\rm set} = b/v_{\rm set} = b^3(\mathcal{G}M_p t_s)^{-1}$.

The above arguments show that a particle cannot be either too small or too large in order to fit the requirement of the pebble accretion. A very small pebble particles that well couples with the gas satisfy the first condition (small t_s), but the settling time may be too long. If the particle is too large aerodynamically, it cannot effectively couple with the local gas so it also fails to settle onto the planet due to the large relative speed.

At large impact parameter b, the pebble accretion is in so-called the Hill limit. In this regime, the settling time scale equals to Ω_K, giving

$$b_H \sim \left(\frac{\mathcal{G}M_p t_s}{\Omega_K}\right)^{1/3} = (t_s\Omega_K)^{1/3}\left(\frac{\mathcal{G}M_p}{\mathcal{G}M_*}\right)^{1/3} R_p \tag{2.53}$$

$$\sim St^{1/3} R_{\rm H}, \tag{2.54}$$

where $St = t_s \Omega_K$ is the Stokes number, R_H is the Hill radius. From condition 1, when $t_{enc} \sim {\Omega_K}^{-1}$, the stokes number is required to be smaller than unity. Here b_H should be interpreted as the largest impact parameter where the pebble accretion can happen, so effectively it is the accretion radius $r_{\rm acc}$ of the planet.

For a planet accreting pebbles from the influx of pebbles, there are two asymptotic limits corresponding to the 2D and 3D accretion. In the 2D limit, $r_{\rm acc}$ is much larger than the scale height of the pebbles, therefore the accretion process is approximated by intercepting a two-dimensional pebble flux within the range $2b_H$ (shear regime). In the 3D limit, the vertical spreading of the pebbles is significant, and the accretion process is approximated by intercepting a three-dimensional pebble flux with the cross section area πb_H^2. The respective accretion rates are

$$\dot{M}_{\rm peb,i} = \begin{cases} 2 v_\infty b_H \Sigma_{\rm peb} & 2D \\ \pi b_H^2 v_\infty \rho_{\rm peb} & 3D \end{cases} \tag{2.55}$$

where $\Sigma_{\rm peb}$ and $\rho_{\rm peb}$ are surface density and density of pebbles, respectively. The term $b_H^2 v_\infty$ can be solved from $t_{\rm enc} = t_{\rm set}$ and substituted to equation 2.55

$$\dot{M}_{\rm peb,i} = \begin{cases} 2 R_H^2 St^{2/3}\, \Omega_K \Sigma_{\rm peb} & 2D \\ 6\pi R_H^3 St \Omega_K \rho_{\rm peb} & 3D \end{cases} \tag{2.56}$$

which are the pebble accretion rates expressed in the dust, planetary and stellar properties in the respective 2D and 3D limits.

The pebble accretion cannot continue indefinitely: when the planet grows and reaches the so-called the pebble isolation mass, it starts to open a shallow gas gap and generate a pressure maxima at the outer edge of the gap, which traps the inflow of pebbles by reversing the local pressure gradient. As a result, the planet no longer has access to the pebbles, and the pebble accretion is self-terminated. As will be introduced in the next subsection, the halt of the pebble accretion is the prerequisite to trigger the rapid runaway gas accretion onto the planet, which eventually leads to the formation of the gas giant. For those planets that never reach the pebble isolation mass, they cannot enter the runaway gas accretion phase and therefore remain as low-mass planets.

Gas accretion

In the standard core accretion model, the rocky core of a planet can acquire a gas envelope when its gravity is strong enough to bound the gas. During the pebble accretion stage, the gas envelope is supported by the thermal pressure that is contributed by both the stellar radoation and the energy realised by the pebbles Mizuno (1980). Along the way of depositing to the planet surface, pebbles are decelerated by the gas envelope due to the drag and thus strongly heat up the planet by converting their gravitational potential energy to the internal energy of the gas. For an opaque gas envelope, pebble accretion is the dominant heating source at the bottom of the gas envelope, while the stellar radiation dominates the outer part.

However, once the planet reaches the pebble isolation mass, no more pebble can accrete onto the planet, and the gas envelope loses one of its heating source. Since the radiation itself alone cannot sustain the mass of the gas envelope, the envelope contracts in order to balance with the gravity, and the gas from nearby disk also flows into the envelope. The contraction of the gas envelope can be approximated as a quasi-static process, and the rapid runaway gas accretion begins when the mass of the envelope exceeds the mass of the core. The gas accretion rate due to the contraction is derived by Ikoma et al. (2000) as

$$\dot{M}_{\rm gas,env} = 10^{-5}\,{\rm M_\oplus yr^{-1}} \left(\frac{M_p}{10\,{\rm M_\oplus}}\right)^4 \left(\frac{\kappa}{0.1\,{\rm m^2 kg^{-1}}}\right)^{-1}, \tag{2.57}$$

where κ is the opacity of the envelope.

The gas accretion rate due to contraction of the gas envelop sharply increases with the planetary mass. The rapid growth of the planet quickly depletes the gas envelop, and the gas supply from the disk is soon saturated and becomes the limiting factor of the growth. However, the gas from the PPD can only be captured and accrete onto the planets at certain sites. The hydrodynamical simulation performed by Tanigawa & Watanabe (2002) revealed that the gas accrete onto the planet by dissipating its energy to the spiral shock generated by the planet.The gas accretion can only take place at $2.5R_{\rm H}$, and the band is as narrow as $0.2R_{\rm H}$, where $R_{\rm H}$ is the Hill radius of the planet. The gas accretion rate is then described by the product of the accretion area per unit time D and the gas surface density of the disk $\Sigma_{\rm g}$:

$$\dot{M}_{\rm gas,hydro} = D\Sigma_{\rm g} \tag{2.58}$$

where

$$D = 0.29 \left(\frac{h_p}{R_p}\right)^{-2} \left(\frac{M_p}{M_*}\right)^{4/3} R_p^2 \Omega_p \tag{2.59}$$

if the range $0.5R_{\rm H} < h_p < 1.8R_{\rm H}$ is considered (Tanigawa & Ikoma, 2007). We adopt this gas accretion rate in our disk evolution model (see section 3.2.3), and couple the gas accretion with a adaptive surface density profile $\Sigma_{\rm g}$ that feedbacks the migration and accretion.

2.3.2 Orbital migration

When a planet is embedded in a PPD, it keeps exchanging of the angular momentum with the disk via gravitational torques and, as a result, migrates. The orbital migration is particularly important in the early evolution phase of a planetary system as it can significant change the configuration of a planetary system in a short time-scale. Modelling the planetary migration requires the quantitative understanding the physical origins of the torques arising from the non-axisymmetric density wave exited by the resonance. In this subsection, we first review the theoretical modelling of the resonance using linear perturbation theory, then the orbital migration in the respective unperturbed and gap-opening scenarios.

Co-rotational and Lindblad resonance

We start from the treatment of Goldreich & Tremaine (1979), who approach this problem by considering the linear perturbation of the gravitational potential followed by the responses of the disk in different resonant modes. Using the same mathematical formalism as Goldreich & Tremaine (1979), we adopt the cylindrical coordinate system (R, θ, z).

Let $\mathbf{v}_0 = R\Omega\hat{\mathbf{e}}_\theta$ and σ_0 be the unperturbed azimuthal velocity and surface density, while $\mathbf{v}_1$ and σ_1 are the first order perturbations of the respective quantity. We introduce an external perturbation potential $\psi_1(R, \theta, t)$ and denote the additional potential perturbation due to σ_1 as ψ_1^D. The linearised hydrodynamical perturbation equations then reduce to

$$\frac{\partial \mathbf{v}_1}{\partial t} + (\mathbf{v}_0 \cdot \nabla)\mathbf{v}_1 + (\mathbf{v}_1 \cdot \nabla)\mathbf{v}_0 = -\nabla(\psi_1 + \psi_1^D + \eta_1), \tag{2.60}$$

$$\frac{\partial \sigma_1}{\partial t} + \nabla \cdot (\sigma_0 \mathbf{v}_1) + \nabla \cdot (\sigma_1 \mathbf{v}_0) = 0, \tag{2.61}$$

where

$$\eta_1 = c_{s0}^2 \left(\frac{\sigma_1}{\sigma_0}\right), \tag{2.62}$$

$$\nabla^2 \psi_1^D = 4\pi \mathcal{G} \sigma_1 \delta(z). \tag{2.63}$$

Here c_{s0} is the unperturbed sound speed, $\delta(z)$ is the Dirac delta function, and η is the enthalpy related to the sound speed. Equations (2.60) and (2.61) are derived from the angular momentum conservation and mass conservation, respectively. Then by writing each perturbation variable in the form of $\mathbf{X} = \mathbf{X}(R) \exp i(m\theta - \omega t)$ with m being an integer, the momentum conservation can be re-written as

$$i(m\Omega - \omega)v_{1,R} - 2\Omega v_{1,\theta} = -\frac{d}{dR}(\psi_1 + \psi_1^D + \eta_1), \tag{2.64}$$

$$2Bv_{1,R} + i(m\Omega - \omega)v_{1,\theta} = -\frac{im}{R}(\psi_1 + \psi_1^D + \eta_1), \tag{2.65}$$

where $v_{1,R}$ and $v_{1,\theta}$ are $\hat{\mathbf{R}}$ and $\hat{\theta}$ components of $\mathbf{v}_1$. B is the Oort parameter defined as

$$B(R) = \Omega(R) + \frac{R}{2}\frac{d\Omega}{dR}, \tag{2.66}$$

Solving $v_{1,R}$ and $v_{1,\theta}$ from the above equations, we obtain

$$v_{1,R} = -\frac{i}{D}\left[(m\Omega - \omega)\frac{d}{dR} + \frac{2m\Omega}{R}\right](\psi_1 + \psi_1^D + \eta_1), \tag{2.67}$$

$$v_{1,\theta} = \frac{1}{D}\left[2B\frac{d}{dR} + \frac{m}{R}(m\Omega - \omega)\right](\psi_1 + \psi_1^D + \eta_1), \tag{2.68}$$

$$D = \kappa^2 - (m\Omega - \omega)^2, \tag{2.69}$$

where $\kappa = 2\sqrt{B(R)\Omega(R)}$ is the epicyclic frequency. We can then substitute the above solution to the mass conservation equation, and the resulting differential equation shows that there are singularities at both $m\Omega - \omega = 0$ and $D = 0$. These correspond to

1. **Co-rotational resonance:** $\Omega(R) = \omega$,
2. **Lindblad resonance:** $m(\Omega(R) - \omega) = \pm\kappa(R)$.

In the case that the planet is the perturbation source, $\omega = \Omega_p$, where Ω_p is the angular velocity of the planet. This means that the co-rotational resonance happens at the same R as the planet. For the Lindblad resonance, if the disk is Keplerian, $\Omega(R) = \kappa(R)$, and

$$\Omega_p = \Omega(R)\left(1 \mp \frac{1}{m}\right). \tag{2.70}$$

If the planet is in a circular orbit with semi-major axis a_p,

$$a_p^{-3/2} = R_L^{-3/2}\left(1 \mp \frac{1}{m}\right), \tag{2.71}$$

$$R_L = \left(1 \mp \frac{1}{m}\right)^{2/3} a_p, \tag{2.72}$$

where R_L is the position that Lindblad resonance takes place. This shows that Lindblad resonance can take place at multiple places. Further details of the calculation can be found in Goldreich & Tremaine (1979).

The migration torque

As a direct consequence of the resonance, density waves are excited at the sites of the resonance and the shock of the wave propagate both inwards and outwards. Such an spiral structure breaks the axial symmetry of the disk, and the planet therefore experience a net torque $\Gamma_{\rm tot}$ can be computed as

$$\Gamma_{\rm tot} = -\int_{-\infty}^{\infty} RdR \int_0^{2\pi} d\phi \sigma_1 (\mathbf{R} \times \nabla\psi_1) \cdot \hat{z}, \tag{2.73}$$

where the notations follow the same meaning as those in the previous subsection. The total torque Γ_{tot} that is experienced by the planet can be written as a summation of both the co-rotational $\Gamma_{\rm C}$ and Lindblad torques $\Gamma_{\rm L}$

$$\begin{aligned}\Gamma_{\rm tot} &= \Gamma_{\rm C} + \Gamma_{\rm L} \\ &= \Gamma_{\rm C} + \Gamma_{\rm L,in} + \Gamma_{\rm L,out},\end{aligned} \tag{2.74}$$

where the subscripts "in" and "out" denote the Lindblad torque exerted by the inner and outer wake of the density wave, respectively. If the total torque is negative (the common case), the planet loses angular momentum and migrates inward; otherwise, the planet gains angular momentum and migrates outwards.

Computation of the torque requires special mathematical expertise to solve the wave equations, and this is usually done by performing numerical integrations. Tanaka et al. (2002) shows that given a planet in a circular orbit located at R_p and the disk surface density profile $d\ln\Sigma/d\ln R = -s$, the Lindblad and corotational torques exerted onto the

planet are approximated by:

$$\Gamma_L = -(2.34 + 0.10s)\Gamma_0, \tag{2.75}$$

$$\Gamma_C = (0.98 + 0.64s)\Gamma_0, \tag{2.76}$$

$$\Gamma_0 = \left(\frac{M_p}{M_*}\right)^2 \left(\frac{h_p}{R_p}\right)^{-2} \Sigma(R_p) R_p^4 \Omega_K^2(R_p), \tag{2.77}$$

where Γ_0 is the characteristic torque, M_p/M_* is the planet-star mass ratio, h_p/R_p is the aspect ratio at the planetary location and Ω_K is the Keplerian angular velocity.

The co-rotational torque $\Gamma_{\rm C}$ is always positive for a disk with surface density decreases with R ($s > 0$), meaning the planet gains angular momentum due to the co-rotational torque; for Lindblad torques, while $\Gamma_{\rm L,in}$ is positive, $\Gamma_{\rm L,out}$ is negative and larger in magnitude, so overall the net $\Gamma_{\rm L} < 0$ and the planet loses angular momentum due to the Lindblad torque. More recent numerical results from Paardekooper et al. (2010) considers the effect of the non-linear horseshoe drag and how the torque scales with the temperature profiles. In this thesis, we adopt the migration recipe based on the result of Paardekooper et al. (2010) and the detailed expressions are in section 3.2.2.

Type I and Type II migration

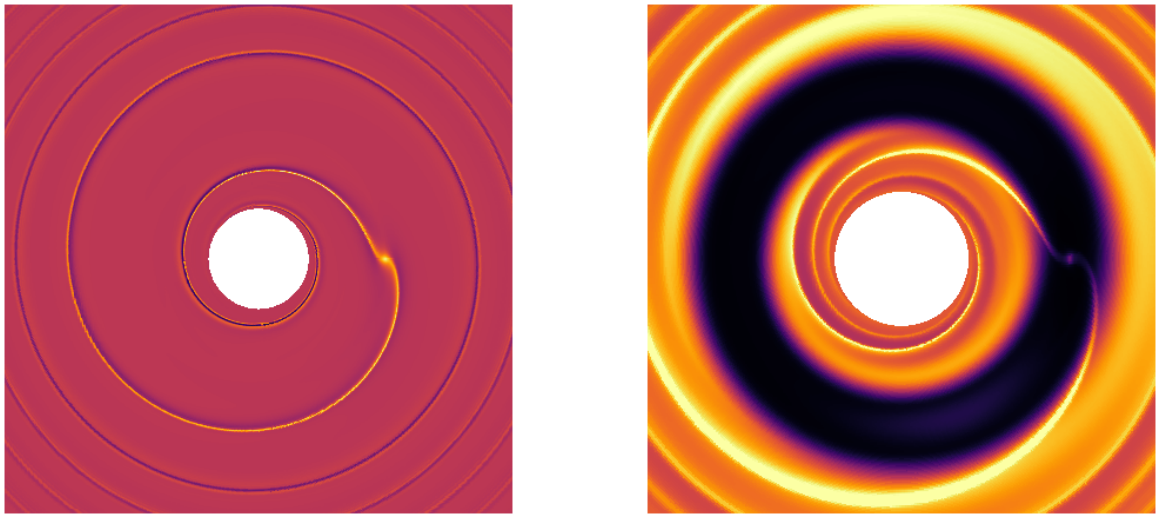

(a) (b)

Figure 2.4: Hydrodynamical simulation results showing how a planet interacts with the disk. (a) Spiral density wave is excited by a low mass planet in a disk. The density of the disk is not strongly perturbed, and the planet is undergoing Type I migration. (b) A deep gas gap (black colour) is opened by a giant planet hydrodynamical simulation. The depletion of the gas inside the gap slows down the migration, and thus the planet is undergoing Type II migration. Colour coded according to the surface density. Credits: Dr. Kazuhiro Kanagawa.

The planetary migration can be classified into Type I and Type II migration depending on the extent that the disk surface density is perturbed by the planet. The planet undergoes

Type I migration when the planetary mass is low so that the disk structure is only slightly perturbed (Figure 2.4 a). In this linear regime, the viscous torques dominates the local angular momentum transport around the planet, and thus we can neglect the change of the disk structure due to the planet's gravitational torques. For Type I migration, all the resonance modes are available, and the planet can migrate at a fast speed.

After the planet becomes massive, the viscous torques around the planet can no longer compete with the strong gravitational torque exerted by the planet. As a result, the gas at the vicinity of the planet is repelled by the shock and a gas gap is opened, and the planet undergoes Type II migraiton (Figure 2.4 b). The low density inside the gap implies that all the resonant modes that are close to the planet will be ineffective, and therefore the total inward migration torque is weaker compared to that of the Type I migration. Type II migration is much more slower and has a much longer migration timescale.

In the classical picture of Type II migration, the gap forbids any gas to cross, and the planet migrates inward at the same viscous speed as the gas with $v_R = 3\nu/2R$. It was later found by Kanagawa et al. (2018) that the gas can still cross the gap even the planet is as massive as Jupiter. Moreover, the migration speed of the planet can be scaled by the depth of the gas gap, defined as the ratio of the surface density inside gap to the unperturbed surface density. We adopt the migration model of Kanagawa et al. (2018) that seamlessly connects the Type I & Type II migration, and the details are in section 3.2.2.

Chapter 3

Planetary systems predicted from the HL Tau disk

3.1 Introduction

HL Tau is a young star hosting a PPD in the Taurus star forming region. It is a well-studied system for interferometric observation even prior to ALMA because of its high brightness at millimetre wavelength, as it hosts one of the most massive disks that have been observed to date, with estimated total disk mass ranging from $0.03\,\mathrm{M}_\odot$to $0.14\,\mathrm{M}_\odot$ (Robitaille et al., 2007; Guilloteau et al., 2011). The HL Tau system attracted particular attention because it is the first PPD whose substructure is well resolved by ALMA high angular resolution observation (Brogan et al., 2015). ALMA successfully resolved the dust concentric ring/gap substructure and identified seven bright rings and dark gaps. Follow-up modelling on the continuum data performed by Pinte et al. (2015) shows the deepest three major gaps are located at $13.2\,\mathrm{au}$, $32.3\,\mathrm{au}$ and $73.7\,\mathrm{au}$, in which the dust density is depleted to at least a factor of 10. The other four gaps are relatively shallow.

There are multiple interpretations of the concentric ring/gap substructures, including secular gravitational instability (Takahashi & Inutsuka, 2016), snowlines (Zhang & Jin, 2015), sintering (Okuzumi et al., 2016) and non-ideal MHD effect (e.g. Flock et al., 2015; Hu et al., 2019). However, the planetary interpretation is widely believed to be a promising explanation. Results of hydrodynamic simulations have confirmed that the morphology of the gap substructure can be well reproduced by a planetary systems consisting of three planets. (e.g., Dipierro et al., 2015; Picogna & Kley, 2015; Jin et al., 2016). By considering the early debris disk dynamics, Boley (2017) also pointed out that three giant planets can produce both major and minor gaps of HL Tau via dynamical interactions between planets and planetesimals. Using the mass-width scaling relation obtained from hydrodynamical simulations, Kanagawa et al. (2016) predict the masses of the three planets from the width of the respective gap along with the disk properties.

As the pioneering work concerning the evolution of the planetary system hosted by HL Tau, Simbulan et al. (2017) performed a series of numerical simulations to predict the

This chapter is mainly based on the modified manuscript of the journal article Wang et al. (2020) that has been published in the Astrophysical Journal.

fate of the observed HL Tau system. Instead of adopting unbiased, realistic initial conditions that are consistent with the disk observation and hydrodynamical simulation, Simbulan et al. (2017) assign four or five planets at the gap locations, and set each planet with equal, large enough mass to make the system initially unstable. They found that more than half of the planets were ejected from the system, collided with another planet, and/or migrated within the Roche radius of the host star. Their conclusion is interesting and may explain the origin of the observed diversity of exoplanets including eccentric cold Jupiters, hot Jupiters, and free-floating planets, at least in a qualitative fashion.

There are a few points in Simbulan et al. (2017) that need to be carefully checked, especially the assumption that inward migration induced by the disk-planet interaction is quite inefficient. Since the age of the HL Tau is only around $1\,\mathrm{Myr}$, the migration and mass accretion of the planets during the rest of the disk lifetime are expected to strongly shape the configuration of the planetary system in the later stage orbital evolution. Moreover, their initial mass assignment of the HL Tau planets is biased towards the their purpose of producing orbital instabilities. It is important to know the intrinsic stability of the HL Tau system when observation-motivated planetary masses predicted from the morphology of the gap, i.e., the gap width and location, are adopted.

In this chapter, we start from the three-planet configuration of HL Tau that has been proposed by previous hydrodynamical simulations (e.g., Kanagawa et al., 2016), and adopt the initial conditions that are motivated by observation for both the planets and disk. We then evolve the HL Tau system with planet-disk interactions as well as planetary mass accretion effects until the end of the disk dispersal. After that, we continue integrating the systems with only mutual gravities among star and planets to examine the orbital stability of the systems. The rest of this chapter is arranged as follows: section 3.2 describes our methodology, including equations of motion, models of migration and accretion, model of disk profile evolution, and initial conditions of the disk and the HL Tau system we adopted. We present results of our simulations in section 3.3, and discuss implications of our results in section 3.4 with particular attention to the orbital stability of the multi-planets. Section 3.5 is the summary of this chapter.

3.2 Methods

In this section, we present our methods to evolve the HL Tau planetary system from the disk stage to $10\,\mathrm{Gyr}$ after the disk dispersal. We also describe the equation of motion for planets inside a disk as well as our accretion and migration model of planets coupled with a surrounding disk.

3.2.1 Equation of motion of planets

For a planet within a disk, in addition to the gravitational forces exerted by the central star and other planets, the planet will experience forces due to planet-disk interactions. Consider the forces acting on the i-th planet, the equation of motion can be written as

$$\ddot{\boldsymbol{r}}_i = \boldsymbol{f}_{\mathrm{grav},i} + \boldsymbol{f}_{\mathrm{a},i} + \boldsymbol{f}_{\mathrm{e},i}, \tag{3.1}$$

where $\boldsymbol{r}_i$ is the position vector of the i-th planet. The $\boldsymbol{f}$ notations on the right hand side of the equation are respective forces *per unit mass* exerting on the i-th planet. We assume the planets to be co-planar, and thus $\boldsymbol{r}_i$ can be replaced by the position vector $\boldsymbol{R}_i(R_i, \phi_i)$ in cylindrical coordinate system. We use $\boldsymbol{R}$ to denote the cylindrical position vector unless stated otherwise.

The first term, $\boldsymbol{f}_{\rm grav}$, of the right-hand-side of equation (3.1) denotes gravitational force exerted by the central star and other planets, and is given by (e.g. Murray & Dermott, 2000):

$$\begin{aligned}\boldsymbol{f}_{{\rm grav},i} &= -\mathcal{G}(M_* + M_i)\frac{\boldsymbol{R}_i}{R_i^3} \\ &+ \sum_k^{k\neq i} \frac{\mathcal{G}M_k}{\parallel \boldsymbol{R}_k - \boldsymbol{R}_i \parallel^3}(\boldsymbol{R}_k - \boldsymbol{R}_i) - \sum_k^{k\neq i} \frac{\mathcal{G}M_k}{R_k^3}\boldsymbol{R}_k,\end{aligned} \tag{3.2}$$

where M_* is the mass of the central star, M_i is the mass of the i-th planet, $R = |\boldsymbol{R}|$, and $\mathcal{G}$ is the gravitational constant.

The second term, $\boldsymbol{f}_{a,i}$, denotes the force driving the migration of planet. A planet with index i embedded in the disk experiences an effective torque Γ_i, and migrates inwards. To describe the motion, it is convenient to introduce an e-folding inward migration time-scale $\tau_{a,i}$:

$$\tau_{a,i}(t) \equiv -\frac{a_i}{{\rm d}a_i/{\rm d}t}, \tag{3.3}$$

where a_i is the semi-major axis of the i-th planet. In the case of a co-planar and near circular orbit, $|\boldsymbol{R}_i| \approx a_i$, and equation (3.3) reduces to

$$\tau_{a,i} = \frac{L_i}{2\Gamma_i} \tag{3.4}$$

in terms of the angular momentum L_i and the torque Γ_i acting on the planet from the disk. Thus, the effective migration force, $\boldsymbol{f}_{a,i}$, is simply given by

$$\boldsymbol{f}_{{\rm a},i} = \ddot{\boldsymbol{R}}_i = -\frac{\dot{\boldsymbol{R}}_i}{2\tau_{a,i}}. \tag{3.5}$$

The disk tends to circularise a planetary orbit. Similarly as equation (3.3), we define the eccentricity damping time-scale, $\tau_{e,i}$. Following Lee & Peale (2002); Kley et al. (2004), we further assume the following expression:

$$\tau_{e,i} = C\tau_{a,i}\left(\frac{h_i}{R_i}\right)^2, \tag{3.6}$$

where C is a constant, and h_i/R_i is the aspect ratio of the disk at the location of the i-th planet. Then the eccentricity damping force is computed as

$$\boldsymbol{f}_{{\rm e},i} = -\frac{2}{3\tau_{e,i}}\left(\frac{\dot{\boldsymbol{R}}_i}{1-e_i^2} - \hat{\boldsymbol{\ell}}_i \times \hat{\boldsymbol{R}}_i\sqrt{\frac{\mathcal{G}(M_* + M_i)}{a_i(1-e_i^2)}}\right), \tag{3.7}$$

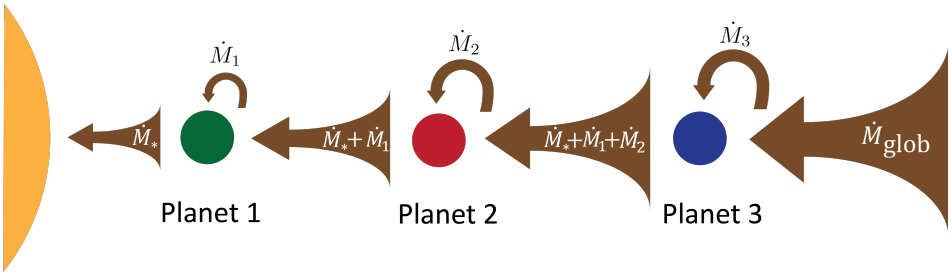

Figure 3.1: Schematic view of the mass flow from outside of the disk to the inside. Blue circles and green arrows are the planets and mass flow. Due to the accretion of the planet, mass flow is discontinuous at the position of each planet.

where $\hat{\ell}_i$ is the unit vector of the specific angular momentum of the i-th planet. (See Appendix A of Lee & Peale, 2002).

3.2.2 Migration model

In section 3.2.1 we have defined the migration time-scale $\tau_{a,i}$ to capture the physics of the migration process. In practice, we adopt an empirical model $\tau_{a,i}$ by Kanagawa et al. (2018). Since this is one of the most important processes that we implement in the current simulation, we summarise the explicit formulae in this subsection.

Kanagawa et al. (2018) performed two-dimensional hydrodynamical simulations, and investigated the planetary migration by varying disk parameters. They found that the migration slows down as the gap becomes deeper. The depth of the gap, defined as the ratio between the minimum bottom density of the gap $\Sigma_{\rm min,i}$ and the surface density of the unperturbed vicinity $\Sigma_g(R_i)$, can be characterised by a dimensionless factor K_i as

$$\frac{\Sigma_{min,i}}{\Sigma_g(R_i)} = \frac{1}{1+0.04K_i}, \tag{3.8}$$

where

$$K_i = \left(\frac{M_i}{M_*}\right)^2 \left(\frac{h_i}{R_i}\right)^{-5} \alpha^{-1}. \tag{3.9}$$

A small value of K_i corresponds to the case of a small planet mass (M_i), in which the planetary migration is in Type I regime. As the planet mass grows due to accretion from disk, the gap depth and therefore K_i gradually increase, and the migration becomes slower (Type II regime).

Adopting this gap parametrisation, Kanagawa et al. (2018) found the following empirical expression of $\tau_{a,i}$ that incorporates the slower migration for the deeper gap:

$$\tau_{a,i} = \frac{1+0.04K_i}{\gamma_{L,i}+\gamma_{C,i}\exp(-K_i/K_t)}\tau_{0,i}(R_i). \tag{3.10}$$

In equation (3.10), $\gamma_{C,i} = \Gamma_{C,i}/\Gamma_{0,i}$ and $\gamma_{L,i} = \Gamma_{L,i}/\Gamma_{0,i}$, where $\Gamma_{C,i}$, $\Gamma_{L,i}$, and $\Gamma_{0,i}$ denote the co-rotation, Lindblad, and characteristic torque for the i-th planet, respectively. The

characteristic torque $\Gamma_{0,i}$ is defined as

$$\Gamma_{0,i}(R_i) = \left(\frac{M_i}{M_*}\right)^2 \left(\frac{h_i}{R_i}\right)^{-2} \Sigma_g(R_i) R_i^4 \Omega_{K,i}^2. \tag{3.11}$$

Here K_t is the co-rotational cut-off value of K_i, $\Omega_{K,i}$ is the Keplerian angular velocity of the i-th planet, and $\tau_{0,i}$ is the characteristic time-scale defined as $\tau_{0,i} = L_i/(2\Gamma_{0,i})$. For a deep gap ($K_i \gg K_t$), equation (3.10) reduces to

$$\tau_{a,i} \approx \frac{1 + 0.04K_i}{\gamma_{L,i}} \tau_{0,i}(R_i), \tag{3.12}$$

which reflects the fact that the migration becomes slower for a deeper gap.

We further adopt the following explicit expressions for the dimensionless torques, which are derived by Paardekooper et al. (2010) assuming that the disk is locally isothermal:

$$\gamma_{C,i} = 1.1(1.5 - s)b_i + 2.2\beta b_i^{0.71} - 1.4\beta b_i^{1.26}, \tag{3.13}$$
$$\gamma_{L,i} = -(2.5 - 0.1s + 1.7\beta)b_i^{0.71}, \tag{3.14}$$

where $s = -\ln \Sigma_g / \ln R$ and $\beta = -\ln T / \ln R$ are the power-law indices of the surface density and temperature profiles. The dimensionless factor b_i was originally introduced by Paardekooper et al. (2010). The value of b_i is fixed to be $2/3$ in our simulation, following Kanagawa et al. (2018).

3.2.3 Mass accretion model

Tanigawa & Tanaka (2016) studied the mass growth of a giant planet and obtained a semi-empirical model of the gas accretion rate onto the planet, which is in reasonable agreement with the results of hydrodynamic simulations. We adopt their model of planetary accretion and hereby summarise key expressions relevant to our simulation.

The model of Tanigawa & Tanaka (2016) states that the accretion rate of the i-th planet, $\dot{M}_i$, can be expressed in terms of the accretion *area* per unit time D_i and the disk surface density of the accretion channel $\Sigma_{\mathrm{acc},i}$ at its location R_i. Since the gas accretion only takes place at the close vicinity of the planet (gas can accrete at around two Hill radii from the planet), we can replace $\Sigma_{\mathrm{acc,i}}$ to $\Sigma_{\mathrm{min,i}}$ given by Equation (3.8). $\dot{M}_i$ is then written as

$$\dot{M}_i = D_i \Sigma_{\mathrm{min},i}, \tag{3.15}$$
$$D_i = 0.29 \left(\frac{h_i}{R_i}\right)^{-2} \left(\frac{M_i}{M_*}\right)^{4/3} R_i^2 \Omega_{K,i}, \tag{3.16}$$

We compute $\dot{M}_i$ iteratively for a given $\dot{M}_{\mathrm{glob}}$ and other planetary configuration.

Instead of Equation (3.8), Tanigawa & Tanaka (2016) adopt a slightly different formula $\Sigma_{\mathrm{min,i}} = 1/(1 + 0.034K_i)$. This difference does not change our main results.

3.2.4 Model of the disk profile hosting multiple planets

The planetary migration and accretion require a disk profile model. For a static and axisymmetric disk surrounding a star, the surface density profile is given by

$$\Sigma_g(R) = \frac{\dot{M}_*}{3\pi\nu(R)}\left(1-\sqrt{\frac{R_*}{R}}\right), \tag{3.17}$$

where $\dot{M}_*$ is the stellar accretion rate, and ν is the kinematic viscosity (Pringle, 1981).

Equation (3.17) assumes that the disk mass accretes on the central star only and neglects the accretion on planets. Tanigawa & Tanaka (2016) incorporates the mass accretion onto a single planet by approximating the planet as a sink for mass and angular momentum within an inward disk mass flow. We generalise their model for a multi-planetary system, as schematically illustrated in Figure 3.1.

To be more specific, we consider a quasi-steady disk with the i-th planet located at R_i with its accretion rate $\dot{M}_i$ ($i = 1, 2, \cdots, N$). We define a global accretion rate as the sum of all the accretion rates:

$$\dot{M}_{\rm glob} = \dot{M}_* + \sum_{i=1}^{N} \dot{M}_i. \tag{3.18}$$

Moreover we assume that the initial value of $\dot{M}_{\rm glob}$ only depends on global parameters of the disk, which are unaffected by the migration and accretion of the planets (see later section 3.2.5).

For a static disk hosting N planets, each located at R_i with accretion rate $\dot{M}_i$, $i \in \{1, 2, ..., N\}$, the conservation of mass can be written as

$$\dot{M}(R) = \begin{cases} \dot{M}_* & (R < R_1), \\ \dot{M}_* + \sum_{i=1}^{n} \dot{M}_i & (R_n < R < R_{n+1}), \\ \dot{M}_* + \sum_{i=1}^{N} \dot{M}_i & (R > R_N), \end{cases} \tag{3.19}$$

where $n \in \{1, 2, ...N-1\}$. Similarly, conservation of the angular momentum gives

$$\dot{M}(R)j(R) = \begin{cases} \dot{M}_* j_* & (R < R_1), \\ \dot{M}_* j_* + \sum_{i=1}^{n} \dot{M}_i j_i & (R_n < R < R_{n+1}), \\ \dot{M}_* j_* + \sum_{i=1}^{N} \dot{M}_i j_i & (R > R_N), \end{cases} \tag{3.20}$$

where $j_i = j(R_i) = R_i^2\Omega_i$ is the specific angular momentum. When $R_n < R < R_{n+1}$, we assume the zero-torque boundary conditions at $R = R_i$, and solve mass transfer equation and obtain

$$3\pi\nu j(R)\Sigma_g(R) = \dot{M}(R)j(R) - \dot{M}_* j_* - \sum_{i}^{n} \dot{M}_i j_i. \tag{3.21}$$

Notation	Meaning	Value
Free Parameters*		
f	Flaring index	[0.15,0.20,**0.25**,0.30,0.35]
$\tau_{\rm disk}$	Disk lifetime	$[1, \underline{\mathbf{2}}, 3]$Myr
α	Viscosity parameter	$[2, \underline{\mathbf{3}}, 4, 5, 6] \times 10^{-4}$
Fixed Parameters		
$M_{\rm disk}^{\rm ini}$	Initial disk mass	$0.105\,{\rm M}_\odot$
M_*	Stellar mass	$1.0\,{\rm M}_\odot$
$(h/R)_{1\,\rm au}$	Aspect ratio at 1 au	0.03

*For free parameters, the underscored values are fiducial values

Table 3.1: Initial conditions of HL Tau disk

where $\Sigma_g(R)$ is the gas surface density at distance R, ν is the kinematic viscosity that can be expressed by theα parameter (Shakura & Sunyaev, 1973). Substituting equation (3.19) to equation (3.21), the surface density profile $\Sigma_{\rm g}(R)$ between the n-th and $(n+1)$-th planets ($R_n \leq R < R_{n+1}$) is then modelled as

$$\begin{aligned}\Sigma_g(R) &= \frac{\dot{M}_*}{3\pi\nu}\left(1-\frac{j_*}{j(R)}\right)+\sum_{i=1}^{n}\frac{\dot{M}_i}{3\pi\nu}\left(1-\frac{j_i}{j(R)}\right)\\ &= \frac{\dot{M}_*}{3\pi\nu}\left(1-\sqrt{\frac{R_*}{R}}\right)+\sum_{i=1}^{n}\frac{\dot{M}_i}{3\pi\nu}\left(1-\sqrt{\frac{R_i}{R}}\right).\end{aligned} \tag{3.22}$$

The above formula shows that the surface density profile couples with the migration and accretion of the planet. Particularly, when R is large, the profile reduces to the form of equation (3.17), *i.e.*, $\Sigma_g(R) \simeq \dot{M}_{\rm glob}/(3\pi\nu)$.

Since the location that we consider is far away from the star ($R \gg R_*$), the bracket of the first term on the right-hand-side of equation (3.22) is unity in practice. If the position and mass of each planet are specified, we can first express the accretion rate of each planet in terms of $\dot{M}_{\rm glob}$ by evaluating equation (3.22) at each R_i and then substituting to equation (3.15). Once $\dot{M}_{\rm glob}$ is given, we can then compute the explicit mass accretion rate of each planet as well as surface density at an arbitrary distance R.

We take account of the gas removal from the disk, simply adopting an exponentially decaying model:

$$\dot{M}_{\rm glob}(t) = \dot{M}_{\rm glob}^{\rm ini} e^{-t/\tau_{\rm disk}}, \tag{3.23}$$

where $\dot{M}_{\rm glob}^{\rm ini}$ is the initial value of the global mass acrretion rate, and τ_{disk} is the e-folding decay time of the disk mass.

Due to the large uncertainty of the disk lifetime, we treat $\tau_{\rm disk}$ as a free parameter in the simulation and consider $\tau_{\rm disk} = 1$, 2 and 3 Myr. Note that for simplicity, the surface density profile given by equation (3.22) does not include the shape of the gap induced by the planet. Equation (3.22) gives $\Sigma_{\rm g}(R_i)$ in equation (3.8).

Notation	Meaning	Value
N	Number of planets	3
a_1, a_2, a_3	Semi-major axis	$13.2, 32.3, 73.7$au
e_1, e_2, e_3	Eccentricity	10^{-7}
i_1, i_2, i_3	Inclination	0
M_1	Mass of Planet 1	$1.4(\alpha/10^{-3})^{1/2}\mathrm{M_J}$
M_2	Mass of Planet 2	$0.2(\alpha/10^{-3})^{1/2}\mathrm{M_J}$
M_3	Mass of Planet 3	$0.5(\alpha/10^{-3})^{1/2}\mathrm{M_J}$

Table 3.2: Initial conditions of planets

3.2.5 Numerical methods and initial condition

We evolve each system numerically including the planet-disk interaction and mass accretion on the basis of the public N-body code `REBOUND` (Rein & Liu, 2012) and its extension `REBOUNDx`. We choose an adaptive time-step integrator integrator `ias15` (Rein & Spiegel, 2014). Within the framework of `REBOUNDx`, we implement additional forces and modify the disk mass according to the surface density.

Our simulation starts from initial conditions following the observed structure of the HL Tau disk (see section 3.1). Table 3.1 summarizes the disk initial conditions that we adopted.

The disk mass has been estimated to be between $0.03\,\mathrm{M_\odot}$ and $0.14\,\mathrm{M_\odot}$ (Robitaille et al., 2007; Guilloteau et al., 2011; Kwon et al., 2011), and the recent result from Kwon et al. (2015) gives the mass of $0.105\,\mathrm{M_\odot}$. We take $0.105\,\mathrm{M_\odot}$ as the disk mass and set the inner edge and outer edge to be $10\,\mathrm{au}$ and $80\,\mathrm{au}$. For simplicity, we assume the stellar mass of HL Tau is $1\,\mathrm{M_\odot}$.

We use a simple power law model to characterise the vertical geometry of the HL Tau disk. The aspect ratio is expressed as

$$\frac{h}{R} = \left(\frac{h}{R}\right)_{1\,\mathrm{au}} \left(\frac{R}{1\,\mathrm{au}}\right)^{f}, \tag{3.24}$$

where f is the flaring index. We consider five flaring indices from 0.15 to 0.35. The reference aspect ratio at $1\,\mathrm{au}$ is fixed to be 0.03, which is roughly consistent with the values used in previous studies (e.g. Dipierro et al., 2015; Kanagawa et al., 2015).

Since the inclination angle of the HL tau disk is around $47°$, ALMA images also resolve the vertical structure of the disk in high resolution. Based on the fact that the gaps and rings are sharp at all azimuthal angles, Pinte et al. (2015) concluded that the HL Tau disk is geometrically-thin and that the majority of the dust is settled near the disk mid-plane. Such a shape suggests a weak turbulence level inside the disk, and thus, a low viscosity due to ineffective angular momentum transfer. Pinte et al. (2015) shows that $\alpha = 3 \times 10^{-4}$ for the α-parameter of the viscosity (Shakura & Sunyaev, 1973) well reproduces the observed image of the HL Tau disk. We follow Pinte et al. (2015) and take the fiducial α value to be 3×10^{-4}. We assume that the disk viscosity α does not vary with time and position. We also consider $\alpha = 2 \times 10^{-4}$, 4×10^{-4}, 5×10^{-4}, and 6×10^{-4} so as to

see the dependence on α.

We normalise the initial global accretion rate $\dot{M}_{\rm glob}^{\rm ini}$ using the initial disk mass calculated from the unperturbed surface density profile(equation 3.17)

$$\begin{aligned} M_{\rm disk}^{\rm ini} &= \int_{R_{\rm in}}^{R_{\rm out}} \Sigma \cdot 2\pi r dr \\ &= \int_{R_{\rm in}}^{R_{\rm out}} \frac{\dot{M}_{\rm glob}^{\rm ini}}{3\pi\nu} \cdot 2\pi r dr. \end{aligned} \tag{3.25}$$

Therefore,

$$\dot{M}_{\rm glob}^{\rm ini} = \frac{3}{2}\nu_{\rm 1au}\left(\frac{M_{\rm disk}^{\rm ini}}{1\,{\rm au}^2}\right)\left[\frac{3/2-2f}{\left(\frac{R_{\rm out}}{1\,{\rm au}}\right)^{3/2-2f}-\left(\frac{R_{\rm in}}{1\,{\rm au}}\right)^{3/2-2f}}\right], \tag{3.26}$$

where $\nu_{\rm 1au} = \alpha h_{\rm 1au}^2 \Omega_{K,1\,{\rm au}}$. Note that in the present simulation, we adopt $M_{\rm disk}^{\rm ini} = 0.105 M_\odot$, which is the initial mass of the disk within the range from $R_{\rm in} = 10\,{\rm au}$ to $R_{\rm out} = 80\,{\rm au}$. In the fiducial case, $\dot{M}_{\rm glob}^{\rm ini} = 3.82 \times 10^{-9}\,{\rm M}_\odot{\rm yr}^{-1}$.

Table 3.2 summarises the planet-related initial conditions. Simbulan et al. (2017) interpreted the HL Tau disk substructure as the existence of four or five planets. Since hydrodynamic simulations (Dipierro et al., 2015; Jin et al., 2016) have shown that the major substructures of the HL tau disk can be well reproduced by three planets, we consider three planets initially located at $13.2\,{\rm au}$, $32.3\,{\rm au}$ and $73.7\,{\rm au}$, corresponding to the first, second and fourth planets in Simbulan et al. (2017). For reference, the mid-plane disk temperature at the location of each planet is $45\,{\rm K}$, $29\,{\rm K}$ and $19\,{\rm K}$ from inner to outer, if the temperature at $13.2\,{\rm au}$ gap is taken as $45\,{\rm K}$ (Table 2, Pinte et al. (2015)) and the flaring index is the fiducial value 0.25.

We assume that the planets are co-planar and initially in near-circular orbits by setting the initial eccentricity to be 10^{-7} for all the three planets. The adopted planetary masses are given from the width of the gap to the planetary mass using an empirical formula following Kanagawa et al. (2016). We choose the planetary masses to be $0.77\,{\rm M_J}$, $0.11\,{\rm M_J}$, and $0.27\,{\rm M_J}$ for our fiducial model of $\alpha = 3 \times 10^{-4}$, and scale them by $\propto \alpha^{1/2}$ (See Equation (5) of Kanagawa et al. (2015) and also Table 3.2).

3.3 Planetary systems evolved from HL Tau

3.3.1 Results before the dispersal of the disk

As shown in Table 3.1, we perform $5 \times 3 \times 5 = 75$ simulation runs by varying disk parameters. The simulation stops at $t = 3\tau_{\rm disk}$ when the gas component of the disk is sufficiently removed from the system.

Figure 3.2 shows an example of planetary evolution with fiducial parameters: flaring index $f = 0.25$, disk lifetime $\tau_{\rm disk} = 2\,{\rm Myr}$ and viscosity $\alpha = 3 \times 10^{-4}$. In $6\,{\rm Myr}$, orbits of planets $1, 2, 3$ shrink from $(13.2, 32.3, 73.7){\rm au}$ to $(11.6, 22.5, 40.7){\rm au}$, respectively, which remain widely separated. Their masses increase from $(0.77, 0.11, 0.27){\rm M_J}$ to $(1.6, 2.3, 4.6){\rm M_J}$.

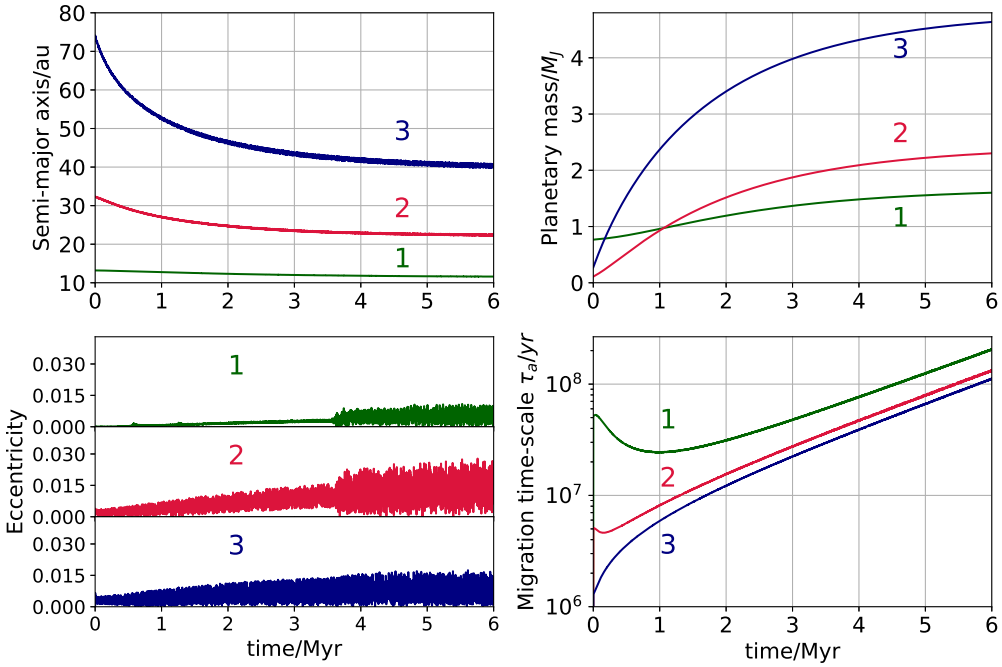

Figure 3.2: The evolution of semi-major axis(top left), planetary mass(top right), eccentricity(bottom left) and migration time-scale(bottom right) in the fiducial case ($f = 0.25$, $\tau_{disk} = 2\,\mathrm{Myr}$, $\alpha = 3 \times 10^{-4}$). The numbers are the planet indices.

The relation between semi-major axis and mass agrees with the result of Tanaka et al. (2020) who have investigated the evolution of a single planet within the disk.

Due to the large initial mass and the low surface density, the innermost planet (Planet 1) barely migrates throughout the disk stage. The outer two planets (Planet 2 and 3) quickly grow and migrate inward for the first $0.5\,\mathrm{Myr}$. As the mass of planets keep growing, the migration of the two planets gradually slows down, and they eventually approach their final positions as the disk surface density decays.

Over the entire migration, eccentricities of the three planets are very small since the slow Type II migration does not lead to any close encounter between the planets. The eccentricities of all three planets are below 0.01 for $t < 2\,\mathrm{Gyr}$. For Planet 2, there is a slight excitation of eccentricity at around $3.6\,\mathrm{Myr}$ due to the approach of Planet 3. Even after the excitation, eccentricities of Planet 2 and 3 fluctuate around 0.025 and 0.015 and nearly stop growing.

The migration time-scales in Figure 3.2 indicate that the outer planet initially migrates faster than the inner planet. In the first Myr, the migration time-scales of Planet 2 and Planet 3 gradually increase, as their gaps become deeper due to the mass growth. The accretion rates of the outer planets also drop, so more mass can flow inside and boost the migration of Planet 1, which explains the decrease of the migration time-scale of Planet 1. The migration time-scales of all the three planets exceed $10\,\mathrm{Myr}$ at $t = 2\,\mathrm{Myr}$. They eventually exceed $100\,\mathrm{Myr}$ at $t = 6\,\mathrm{Myr}$, and their migration ceases practically.

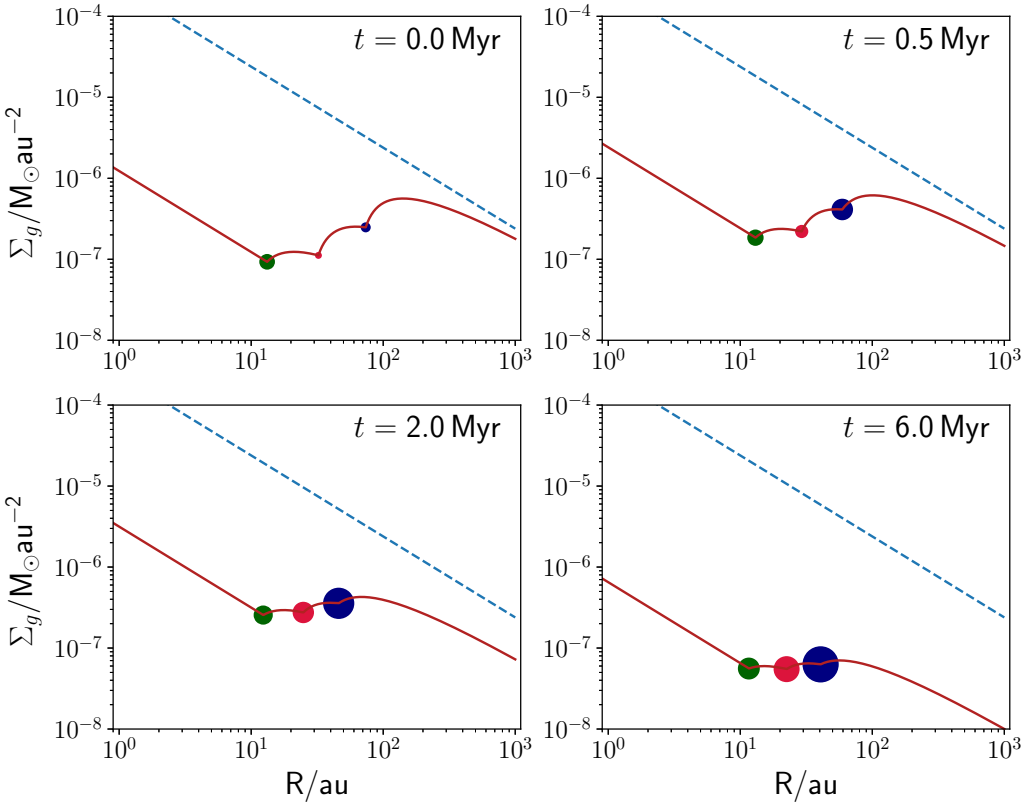

Figure 3.3: Disk surface density profile at four different epochs. Each coloured dot indicates the respective position of the planet, where the size of the dot is proportional to the mass of the planet. As a reference, the blue dotted line is the disk profile without the planets at t = 0.

Figure 3.3 plots the global surface density profile (*cf.* equation 3.22) at four different epochs of the fiducial run, while Figure 3.4 is the evolution of the surface density evaluated at the location of each planet. At $t = 0$, the strong mass accretion onto planets 2 and 3 creates steep bumps on the density profile, and the surface density around Planet 1 is quenched to less than $1\,\%$ of the unperturbed value. As Planets 2 and 3 continue to grow, their accretion rates drop as $\dot{M}_i \propto M_i^{-2/3}$. Thus the mass flows through the outer planets and accretes inward preferentially on planet 1 and the star. At $t = 2\,\mathrm{Myr}$, the planetary system becomes more closely packed and accretion rates of all the planets drop. As a result, density bumps around the planets almost vanish, while the density at the vicinity of each planet reaches the maximum at this epoch. At $t = 6\,\mathrm{Myr}$, the density bumps become further negligible and the surface densities at three planets become nearly identical.

Figure 3.5 illustrates the configurations of the planetary systems at $3\tau_{\mathrm{disk}}$ with different disk parameters. For each plot, we vary only one free parameter while the other two are fixed as their fiducial values. Overall the mass of the outer planet is larger than that of inner one, because the outer planet grows faster than the inner one. The gas accretion onto the outer planet decreases the gas surface density around the inner planets. Because of the lower gas density, the migration and mass growth of the inner ones are

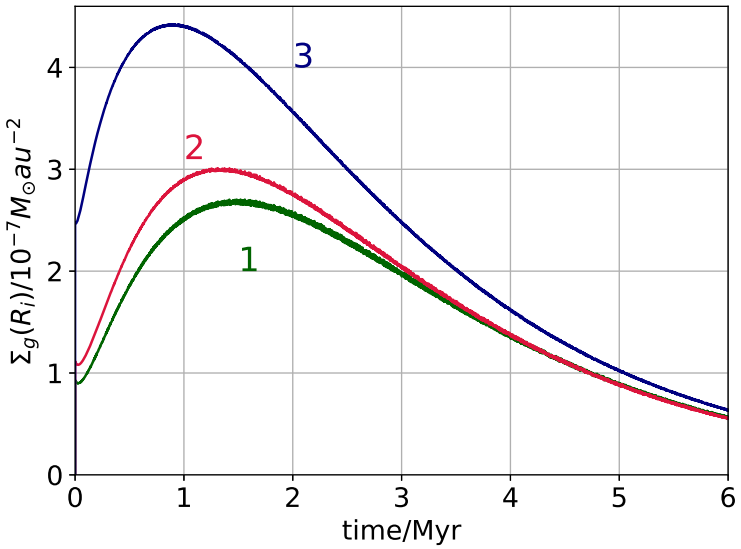

Figure 3.4: Evolution of the disk surface density at the location of each planet

suppressed until the gas accretion onto the outer planet becomes small due to the formation of the deep gap. This is why the evolution of the inner planet is less sensitive to the disk parameters compared to the outer planet. The final semi-major axis and planetary mass change monotonically with the value of each parameter.

When the flaring index f increases from 0.15 to 0.35, the final semi-major axis decreases and final mass increases. As the flaring index become larger, the aspect ratio of the disk increases quickly with radii, resulting in a much shallower gap since the gap depth is sensitive to the aspect ratio to the fifth power (see equations 3.8 and 3.9). While the ratio of Lindblad torque decreases with the flaring index since $T \propto R^{-(1-2f)}$ and $\Sigma \propto R^{-(0.5+2f)}$ (see equation 3.14), the effects caused by a shallower gap dominates both the migration time-scale (see equation 3.12) and accretion rate. Consequently, the planets experience stronger migration and accretion, and eventually move further inward and become more massive. This effect is stronger at large radii, and hence the outermost planet is most affected, as shown by Figure 3.5.

When τ_{disk} increases from $1\,\mathrm{Myr}$ to $3\,\mathrm{Myr}$, the final semi-major axis decreases and final mass increases monotonically. Since τ_{disk} is basically a disk lifetime, the above trend is easily understood as planets in a long-lived disk simply have longer time for migration and accretion.

Finally, a higher viscosity implies that planets experience stronger migration and accretion, as evidenced by the decreasing semi-major axis and increasing final mass. Physically, it is because the angular momentum transfer becomes more efficient with a higher viscosity. A more quantitative discussion can be made from equation (3.9), which is similar to the explanation of flaring index dependence. Since the diffusion time-scale is proportional to $\nu^{-1} \propto \alpha^{-1}$, a larger value of α leads to a faster gas diffusion, resulting in a shallower gap carved by a planet with the same given mass, *i.e.*, the K value is smaller. Thus the migration time-scale is shorter and migration is faster. The mass accretion dependence on K is understood similarly: the accretion density Σ_{acc} is higher for a shallower gap, and therefore a planet grows factor with a higher accretion rate and becomes

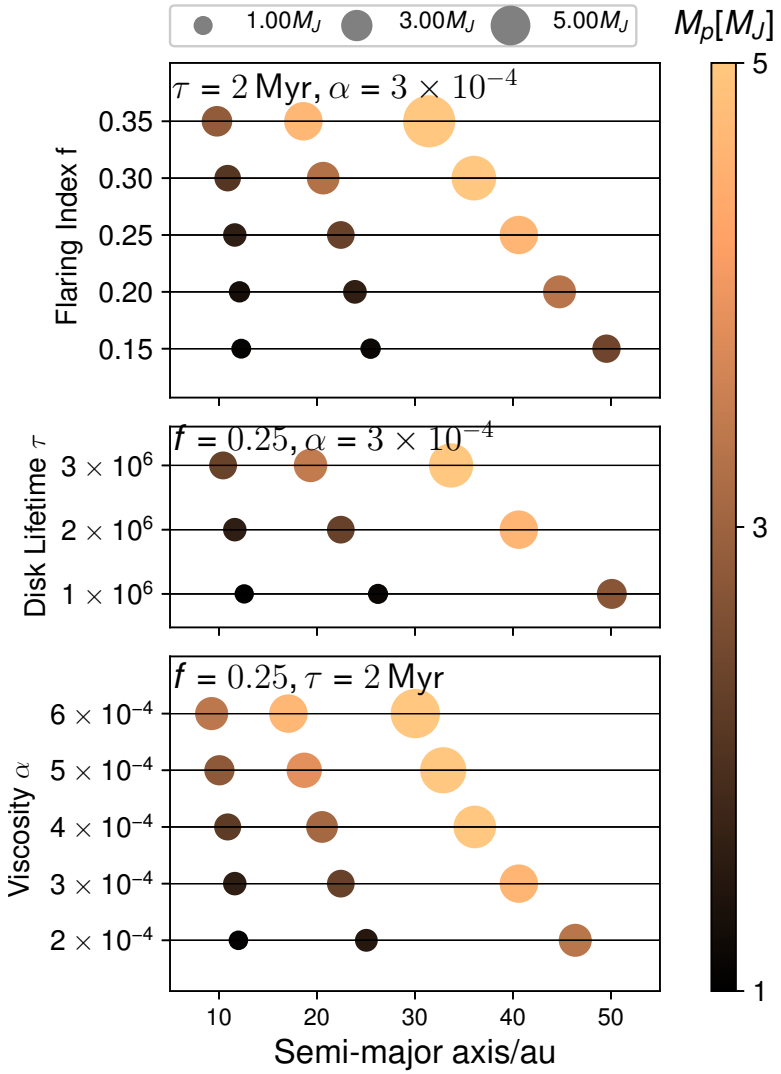

Figure 3.5: Planetary configurations at $t = 3\tau_{\rm disk}$ with different disk parameters. The size of the marker is proportional to the mass of the planet.

more massive.

We find that 74 out of our 75 runs remain stable until the end of the disk gas removal at $3\tau_{\rm disk}$, but the remaining run with $f = 0.35$, $\tau_{\rm disk} = 3\,{\rm Myr}$, and $\alpha = 6 \times 10^{-4}$ turns out to be unstable before the epoch. In this case, the innermost Planet 1 is ejected due to gravitational scattering, and the remaining Planet 2 and 3 are in fairly eccentric orbits($e_2 = 0.55, e_3 = 0.21$). We therefore exclude this single unstable case in our follow-up analysis. Nevertheless, this unstable case stresses the importance of the planet-planet interaction even before the dispersal of the disk, which is absorbed in our N-body approach. When planets are close to each other, particularly inside the resonance overlapping region, planet-planet interactions can couple with the planet-disk interactions and play an important role in shaping the stability of the configuration.

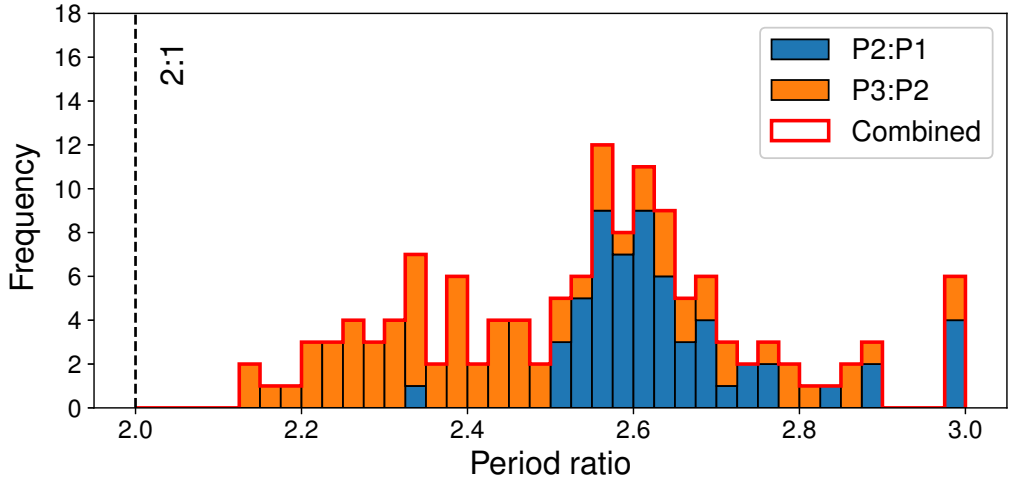

Figure 3.6: Histogram of period ratios of adjacent planet pairs at $t = 3\tau_{disk}$. The bin size is 0.025.

3.3.2 Period ratios and mean motion resonance

The stability of systems emerging from the HL Tau disk may be understood as well in the context of the mean-motion resonance (MMR) capture during a convergent migration (Mustill & Wyatt, 2011; Goldreich & Schlichting, 2014; Deck & Batygin, 2015; Tamayo et al., 2017). Obertas et al. (2017) found that the stability of a planetary system is enhanced if a pair of planets are in a near-resonant state. Tamayo et al. (2017) performed simulations for the TRAPPIST-1 planetary system, and concluded that the disk migration can produce a resonant chain of planets, which significantly stabilises the system.

Motivated by these studies, we plot the histogram of period ratios between adjacent planets, P_2/P_1 and P_3/P_2, at the initial epoch (Figure 3.6). The period ratios fall within the range from 2.1 to 3.0. The minimum period ratio is clearly above 2.0, indicating that no planet pair has ever entered the strongest first-order resonance region. The cut-off implies the existence of a strong co-migration between two planets; when the outer planet approaches the inner planet from outside of 2:1 period ratio, the inner planet is forced to migrate together, which prevents the planet pair from further approaching and entering the first-order MMR region.

The period ratios of the two adjacent pairs also exhibit different statistical distributions. The period ratios of the outer pair (P_3/P_2) are widely distributed between 2.1 and 2.9 range, while those of the inner pair (P_2/P_1) are in a narrow range between 2.5 and 2.8 with a peak at 2.6. These distributions indicate that the outer pairs are more closely-packed than the inner pairs on average. One possible explanation is that the period ratio is determined by the migration speed difference of the pair. In the case of the outer pair, the faster migration speed of Planet 3 allows Planet 3 to reach the region closer to the 2:1 resonance before the co-migration starts. In the case of the inner pair, however, the migration speed of Planet 2 slows down and their orbital separation is wider before Planet 2 approaches Planet 1.

In order to see the depth of the resonance, we plot in Figure 3.7 the 2:1 resonant argument of the inner planet in the fiducial run; upper and lower panels correspond to the inner

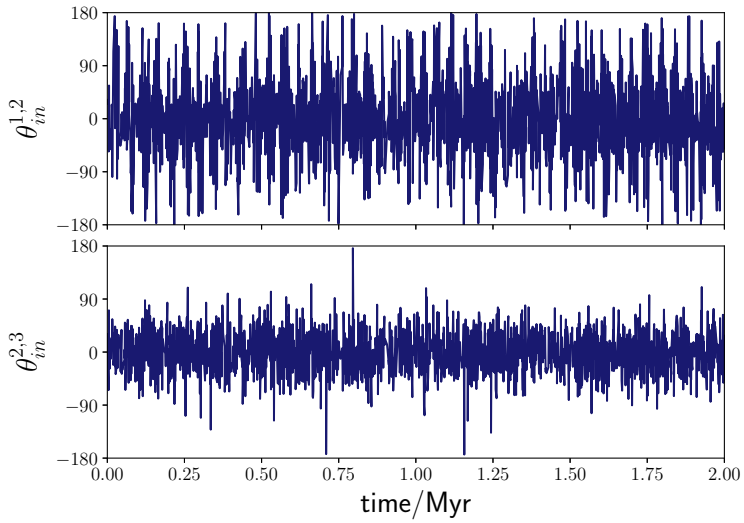

Figure 3.7: 2:1 resonant argument evolution of the inner planet in planet-pair 1,2 and planet-pair 2,3 of the fiducial case after disk dispersal.

and outer planet-pairs, respectively. The 2:1 resonant argument of the inner planet is defined as

$$\theta_{in} = \lambda_{in} - 2\lambda_{out} + \varpi_{in}, \tag{3.27}$$

where λ is the mean longitude and ϖ is the longitude of periastron with subscripts “in" and “out" denoting the inner and outer planet, respectively.

The resonant argument of Planet 1 in the inner planet-pair shows significant fluctuation around $\theta = 0°$ with an amplitude of nearly $180°$. The resonant argument of Planet 2 in the outer planet-pair shows a much ‘well-behaved’ oscillation at an amplitude of $90°$, with sporadic spikes almost touching $\pm 180°$. It is expected that the outer pair of planets are in a deeper resonance state because they are closer to each other than the inner pair, shown by the period ratio histograms. Both of the resonant arguments indicate that the planets are neither in deep resonance nor totally out-of-resonance, since both arguments are not librating between $\pm 180°$ throughout the time. It is not clear that how much such a weak resonance state can contribute to the long-term stability. However, as already pointed out by dynamical stability studies concerning the system HR 8799 (see section 3.4.2), being in deep resonance state is not a necessary condition for long-term stability.

3.3.3 Results at $10\,\mathrm{Gyr}$ after disk dispersal

We continue evolving the 74 systems from the final planetary configurations at $3\tau_{\mathrm{disk}}$ of the previous disk stage using purely N-body simulation after the disk dispersal. When one of the planets is ejected from the system or collide with star/other planet, we stop the simulation and mark the run unstable. Otherwise the system is integrated up to $10\,\mathrm{Gyr}$. The simulation runs are effectively 2D simulation since no inclination has been introduced throughout our simulations.

Figure 3.8 shows the orbital evolution of the planets in our fiducial case after the disk

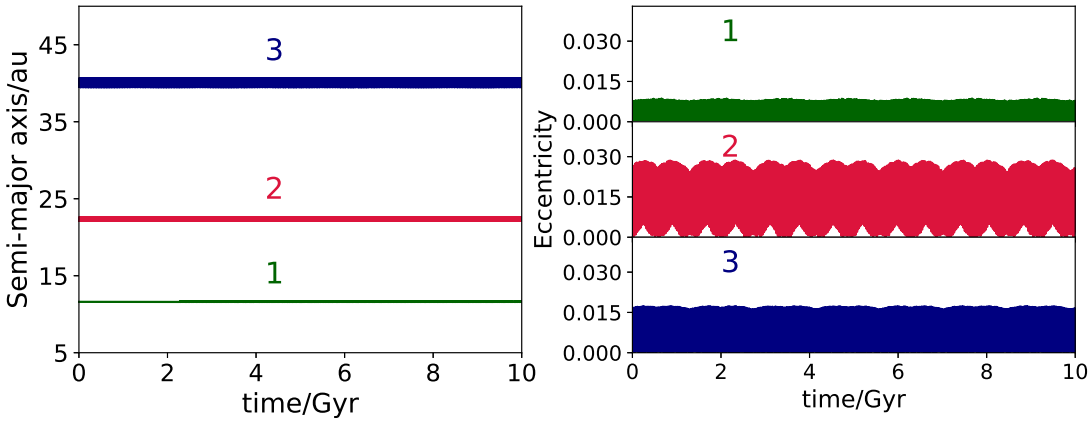

Figure 3.8: Evolution of the semi-major axis and eccentricity of the fiducial case $10\,\mathrm{Gyr}$ after disk dispersal in our fiducial case (the parameters are the same as these in the case shown in Figure 3.2).

dispersal. Clearly there is no significant change in the semi-major axis and eccentricity of the planet during $10\,\mathrm{Gyr}$. We also confirmed that the majority of the systems (69 out of 74) remain stable until $10\,\mathrm{Gyr}$ as in the case shown in Figure 3.8.

A low fraction of unstable systems may imply that most of the planetary configuration achieved through physical disk-planet evolution is indeed stable. This is in contrast to the fact that a significant fraction of numerical simulations exhibit unstable outcomes, most likely due to their relatively artificial initial conditions. Our result indicates that the production of misaligned planets and Hot Jupiters via the instability channel is rather inefficient, at least for the HL Tau disk.

The remaining 5 systems become unstable within $0.004\,\mathrm{Gyr}$ to $5.7\,\mathrm{Gyr}$. We find that the instability time is extremely sensitive to the numerical treatment because of the chaotic nature of such systems, and even a tiny numerical truncation error could result in a $50\,\%$ change of the instability time. The precise value of the instability time can be trusted roughly within an order of magnitude. More detailed discussions on the instability is given in section 3.4.1 below.

3.4 Discussion

3.4.1 Consistency with the previous stability criteria

The stability criterion of a multi-planetary system has been extensively investigated. In particular, a number of previous work (e.g. Gladman, 1993; Chambers et al., 1996; Marzari & Weidenschilling, 2002; Quillen, 2011; Tamayo et al., 2016; Wu et al., 2019) pointed out on the basis of the Hill stability argument that a mutual orbital separation of planets plays an important role in their long-term stability. However, when the planetary mass is large, the mean resonance becomes important and those empirical relations based on mutual Hill radius are not directly applicable. We found that the instability time predictions given by Chambers et al. (1996) and Marzari & Weidenschilling

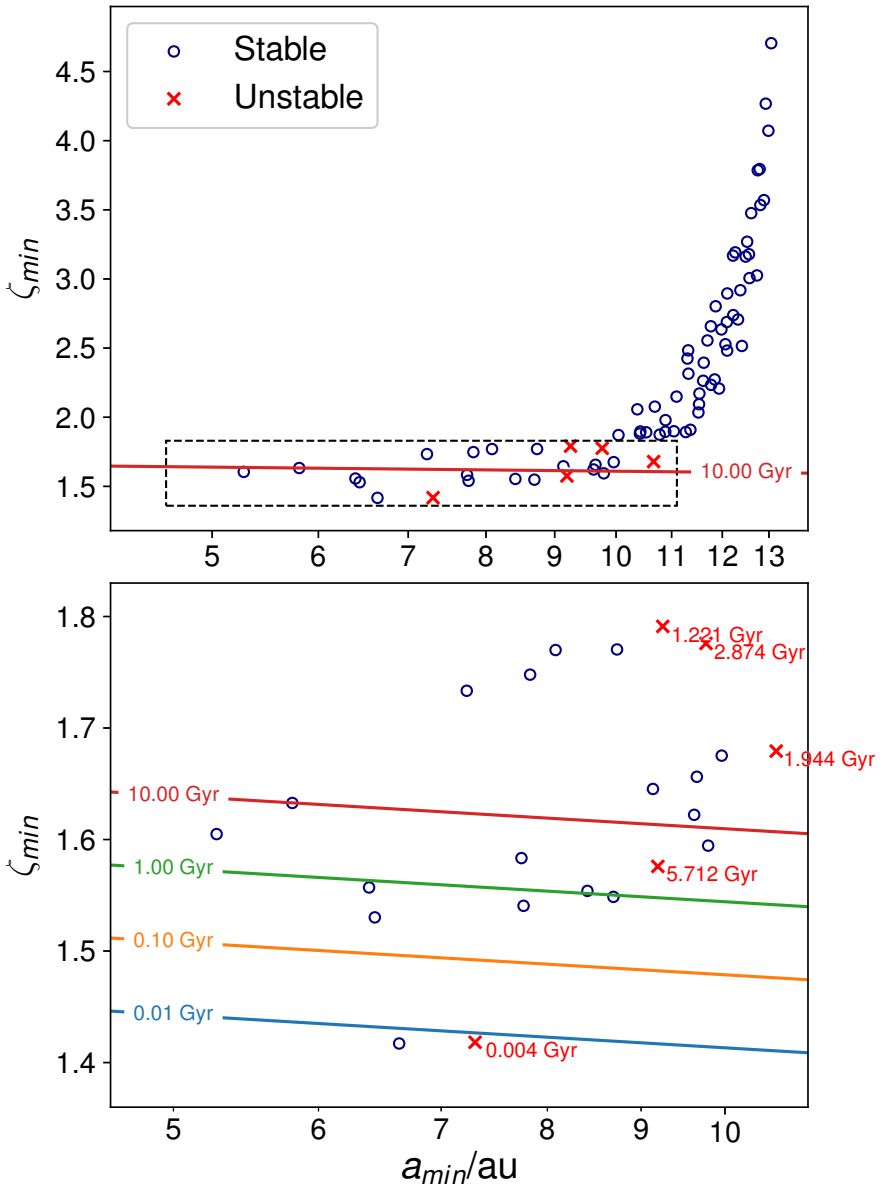

Figure 3.9: $\zeta_{\min}$ against the semi-major axis of the innermost planet. The figure below is the enlarged dotted area on figure above. Unstable cases and corresponding instability time are tagged in red. The coloured lines are the instability time contours based on the result of Morrison & Kratter (2016).

(2002) significantly underestimate the lifetime of our simulated systems. For instance, the criterion given by Marzari & Weidenschilling (2002) predicts half of the systems to be unstable, though most of the systems are stable in our simulations. This discrepancy is originated from the planetary mass dependence of the stability criterion.

Morrison & Kratter (2016) performed a series of simulations with three and five equal-mass planets and found that the mean resonance overlap is a better measure of the orbital stability in the high mass regime larger than Jupiter. On the basis of their argument, we consider the following empirical log-linear relation between an orbital instability time $T_{\rm ins}$ and a dimensionless orbital spacing ζ:

$$\log(T_{\rm ins}/P_{\rm inner}) = c\zeta + d, \tag{3.28}$$

$$\zeta_{\rm min} = \min_{i=0,1,2} \zeta_i, \tag{3.29}$$

$$\zeta_i \equiv \left.\frac{a_{i+1} - a_i}{\delta a_{{\rm ro},i}}\right|_{\rm init}, \tag{3.30}$$

$$\delta a_{{\rm ro},i} \equiv 1.5 \left(\frac{M_p}{M_*}\right)^{2/7} a_i, \tag{3.31}$$

where $P_{\rm inner}$ is the orbital period of the inner-most planet, M_p is the planetary mass, $\delta a_{{\rm ro},i}$ is the separation where two first-order mean resonances overlap, and c and d are numerical constants. Note that the initial conditions of the simulations of Morrison & Kratter (2016) are such that ζ_i are independent of i for a given system, and thus $\zeta_{\rm min} = \zeta_i$. Then we fit equation (3.28) to their result (left panel of their Figure 3 with three equal-mass planets), and found that $c \approx 15.3$ and $d \approx -16.1$ for planets more massive than $10^{-3}\,{\rm M}_\odot$ reproduce their data roughly within one order-of-magnitude.

Since our systems consist of three unequal-mass planets, and ζ_i depend on i, we cannot directly adopt equation (3.28) for the stability condition. Deck et al. (2013) found the same relation hold if the mass ratio in the original $\delta a_{{\rm ro},i}$ is replaced by the sum of the mass ratios of two planets, *i.e.*, $\delta a'_{{\rm ro},i}$. We compared both scaling factors and found $\delta a'_{{\rm ro},i}$ is more consistent with our results with unequal planetary mass. Thus we extrapolate equation (3.28) and rewrite it in terms of $\delta a'_{{\rm ro},i}$ as follows:

$$\log\left(\frac{T_{\rm ins}}{\rm yr}\right) = c\zeta'_{\rm min} + d + \frac{3}{2}\log\left(\frac{a_{\rm inner}}{1\,{\rm au}}\right) - \frac{1}{2}\log\left(\frac{M_*}{{\rm M}_\odot}\right). \tag{3.32}$$

In the above expression, $a_{\rm inner}$ is the semi-major axis of the innermost planet evaluated at the initial epoch for the N-body simulation (*i.e.,* at the end of the disk-planet interaction run), and

$$\zeta'_{\rm min} = \min_{i=0,1,2} \zeta'_i, \tag{3.33}$$

$$\zeta'_i \equiv \left.\frac{a_{i+1} - a_i}{\delta a'_{{\rm ro},i}}\right|_{\rm init}, \tag{3.34}$$

$$\delta a'_{{\rm ro},i} \equiv 1.5 \left(\frac{M_i + M_{i+1}}{M_*}\right)^{2/7} a_i. \tag{3.35}$$

Figure 3.9 plots ζ_{min} against the $a_{\rm inner}$ for 74 runs. Circles indicate 69 systems that are stable until $t = 10\,{\rm Gyr}$, while the remaining 5 systems (crosses) become unstable within the integration time. As a reference, equation (3.32) predicts that 62 systems are stable, and our simulation confirmed that 59 out of the 62 systems (95.2%) are indeed stable. On

the other hand, among the 12 systems that are predicted to be unstable within 10 Gyr, only 2 systems become unstable, indicating that equation (3.32) systematically underestimates the instability time to some extent. Although the actual instability time can deviate up to two or three orders of magnitude from the predicted line, equation (3.32) outperforms other criteria and is roughly consistent with our result that most of systems are stable within 10 Gyr.

3.4.2 Implications for widely-separated massive planetary systems like HR 8799 and PDS 70

Our simulation shows that a stable, widely-separated super-Jupiter system is the dominant outcome of the three-planet configuration that we extracted from the current HL Tau observation, within the parameter space that we explored. Such a configuration is beyond the detection range of the previous prolific planet-hunting telescopes like *Kepler*, and therefore our result is largely different from the majority of multi-planetary systems known to-date, which are generally closely-packed with earth-size planets. There are a couple of such systems, HR 8799 and PDS 70, which have been detected so far via direct imaging or high-resolution spectroscopy.

Both HR 8799 and PDS 70 host planets several times massive than Jupiter separated by a large distance. The HR 8799 system is known as the first multi-planetary system discovered via direct imaging (Marois et al., 2008, 2010). It consists of four giant planets located at 16.4 au, 27 au, 42.9 au and 68 au, with estimated mass ranging from 7 M_J to 10 M_J (Marois et al., 2010; Soummer et al., 2011). The best-fit model shows that the orbits are near co-planar with a low eccentricity ~ 0.1. PDS 70 hosts two planets with semi-major axes 20.6 au and 34.5 au and planetary masses estimated to be 7 M_J to 8 M_J (Keppler et al., 2018; Haffert et al., 2019). Results of our simulations show the mass of the outer planet is likely to be larger than that of the inner planet. Moreover, the period ratios of the planet pair can be close to but outside the 2:1 mean-motion resonance. The systems of HR 8799 and PDS 70 satisfy the above features, which may indicate that these planets may be formed in protoplanetary disks similar to HL Tau.

In terms of the planet formation picture, PDS 70 agrees with what we assume for HL Tau. Its two planets are observed inside a gap of the transiting disk, and the Hα emission indicates that gas accretion onto the planets is still ongoing (Keppler et al., 2018). The formation channel of HR 8799, however, remains to be understood. Previous studies (e.g. Boss, 2011; Vorobyov, 2013) suggest that planets in HR 8799 are likely to be produced via *in-situ* gravitational fragmentation, due to the difficulty to apply the standard core accretion model at such a large distance. Our simulation shows it is physically possible to form such wide-separated systems similar to HR 8799 via migration and accretion, if our planetary interpretation on the current substructure of the HL Tau disk is adopted. However, such a initial condition bypasses the fundamental difficulty of forming planets at large distances from the star, and may only be an intermediate state in a larger evolution picture.

The dynamical stability of HR 8799 remains as yet another unsolved question. Fabrycky & Murray-Clay (2010) pointed out that HR 8799 may have an instability time much shorter than the stellar age, and some sort of resonance is required to stabilise

the system. Goździewski & Migaszewski (2018) proposed that the stable configuration of HR 8799 may be attributed to the resonance capture resulting from the convergent migration. In a different context, our simulation result confirmed that the convergent migration is a natural solution to the long-term stable configuration, even though our systems are in marginal resonance. In fact, our results are similar to the results shown by Figure 10 in Götberg et al. (2016), who found the presence of systems only 'sporadically' in resonance without being locked (See Figure 3.7).

Due to the limited number of such observed systems, we are unable to conclude anything definite at this point. Since we have seen some interesting connections with the two observed examples, however, we may speculate that those widely-separated planetary systems originate from the HL Tau like disks may commonly exist. This speculation can be tested further by future possible detection of systems similar to HR 8799 and PDS 70 using the current and next-generation telescopes, such as *WFIRST* and *JWST*.

3.5 Summary

We consider three planets initially in co-planar, circular orbits with semi-major axis corresponding to the three deepest gas gaps in the HL Tau disk, and perform two-stage numerical simulations. In the disk stage, we include both realistic migration and accretion processes coupling with an adaptive disk profile, and evolve the system until the disk is sufficiently dispersed. After the disk dispersal, we continue to evolve the system using purely gravitational N-body simulations, and examine the orbital stability up to $10\,\mathrm{Gyr}$. Our main conclusions are summarized below:

- We are able to produce a variety of widely separated multi-planetary systems by varying the disk parameters from the HL Tau. When we increase the values of the flaring index, disk lifetime and the α viscosity, both the migration and accretion become stronger. Both the final semi-major axis and mass of the inner planet are less sensitive to the disk parameters, while those of the outer planet are more sensitive. Although the period ratios of most planet pairs are larger than 2, these pairs are in marginal 2:1 resonance. Planets of the outer pair (Planet 2 & 3) are closer to each other than those of the inner pair (Planet 1 & 2).

- We found that majority of systems are stable. We run 75 models with different disk flaring index, viscosity, and gas dispersal time-scale, and 69 out of the 75 models remain stable for 10 Gyr. In our fiducial model, for instance, three planets migrate from $13.2, 32.3, 73.7\mathrm{au}$ to $11.6, 22.5, 40.7\mathrm{au}$ within $6\,\mathrm{Myr}$, while their masses also grow from $0.77, 0.11, 0.27\mathrm{M_J}$ to $1.6, 2.3, 4.6\mathrm{M_J}$. The eccentricities of all planets are below 0.03 due to the absence of close-encounter, and the migration is convergent.

- The stability of those systems is roughly consistent with the previous empirical criterion by Morrison & Kratter (2016). It is also explained by the lack of adjacent planet pairs crossing the 2:1 resonance zone.

- The resulting architecture of widely-separated massive planetary systems is similar to the observed systems including HR 8799 and PDS 70, indicating an inter-

esting link between the HL Tau like disks and the origin of such wide-orbit giant-planet systems.

Our results imply that the HL Tau disk predicts a fairly stable architecture with longer-period planets. While such systems remain to be detected in future with longer-time monitering, there are a couple of systems resembling our prediction. To understand the statistical significance of our result from HL Tau, we need to expand our disk sample to more ALMA disks.

Chapter 4

Planetary systems predicted from multiple ALMA disks I: initial planetary mass predictions

4.1 Introduction

In Chapter 3, we investigated the evolution of the HL Tau system and found a variety of the widely-separated super-Jupiter systems can be produced at the end of the disk, and most of the systems can stay stable for at least $10\,\mathrm{Gyr}$. Nevertheless, such a conclusion may not necessarily hold for planetary systems hosted by other protoplanetary disks.

As we have reviewed in section 2.1.2, the observed PPDs exhibit a broad distribution in mass, size, temperature profile, and their gap substructures also differ in terms of location and width. Since the initial planetary configurations are sensitive to the morphology of the gap substructure and the later-stage evolution is tightly coupled to the disk parameters, the architecture of the planetary systems out of other ALMA PPDs may differ significantly from that of the HL Tau. It therefore motivates us to generalize our findings by exploring a variety of the ALMA PPDs with similar gap substructure like HL Tau.

We start our investigation on other disks from the planetary mass prediction. In the case of HL Tau, we adopt the interpretations of Kanagawa et al. (2016) that all planets have opened gas gaps. The opening of the gas gaps on the HL Tau disk has been largely confirmed by the HCO^+ (1-0) gas emission data (Yen et al., 2016). However, most of the observed gap/ring shapes can only be derived from the dust continuum image alone, so it is not clear if the gap is opened in the gas disk as well. Although a high angular resolution observation of gas line emission can resolve this degeneracy, it is technically difficult and feasible only for very nearby disks even with ALMA except for some particular nearby disks such as TW Hya and PDS 70 (Nomura et al., 2021; Long et al., 2018b).

Since the gap opening mechanisms on gas and dust are physically different, the mass-width scaling relations in the respective regimes are likely to have different dependence

This chapter is mainly based on the modified manuscript of the journal article Wang et al. (2021a) that has been published in the Astrophysical Journal.

on the planet and disk properties. Indeed, the scaling relations derived for massive planets that open both dust and gas gaps (Kanagawa et al., 2016; Dong & Fung, 2017; Zhang et al., 2018) are found to have more explicit dependence on gas disk parameters than those derived for relatively low mass planets opening gaps only in the dust disk (Dipierro et al., 2015; Rosotti et al., 2016; Dipierro & Laibe, 2017). The difference between those two models results in fairly different mass predictions and eventually leads to distinct fates for those disk systems, therefore posing a need to distinguish between the two gap opening scenarios.

The above difficulty motivates us to use mass criteria to differentiate the two scenarios and improve the planetary mass predictions. Theoretically, a planetary core formed by the collision or the fragmentation is supposed to grow via pebble accretion until its mass reaches the pebble-isolation mass $M_{\rm iso}(\sim 10\,{\rm M}_\oplus)$. (e.g., Morbidelli & Nesvorny, 2012; Lambrechts et al., 2014; Bitsch et al., 2018). When the core mass is smaller than $M_{\rm iso}$, it forms no gap or very shallow gap in the gas disk. After the core mass exceeds $M_{\rm iso}$, the planetary core acquires a gas envelope due to the onset of runaway gas accretion (e.g., Mizuno, 1980; Bodenheimer & Pollack, 1986; Ikoma et al., 2000). The resulting giant gaseous planet carves a deep gap in both gas and dust disks. According to the above theoretical understanding, the pebble isolation mass can be used as a boundary to break the degeneracy of two possible situations: the case that only the dust gap is opened, and the case that both the gas and dust gaps are opened.

In this chapter, we consider the two different predictions for the planetary mass from the dust gap properties, and discuss how we can distinguish between the two models, the dust only gap and both the gas and dust gaps. The rest of this chapter is organized as follows. Section 4.2 describes disk systems that we consider in the present study, and summarizes the observed properties of observed gaps revealed by the dust continuum. In section 4.3, we review the current understanding of the planet formation in the core-accretion scenario, the methods to deduce the planet mass from the shape of the gap, and the criteria to classify the gaps according to the two models. Section 4.4 presents the result of gap classification and the corresponding planetary mass predicted from the classification. Section 4.5 discusses the implications of our results on the planet formation. Finally, section 4.6 is devoted to the summary and conclusion of this chapter.

4.2 Properties of disks and gaps of our sample

Recent observations have discovered a number of substructures in PPDs. In particular, the continuum data of 20 nearby PPDs by The Disk Substructures at High Angular Resolution Project (DSHARP) (Andrews et al., 2018) have revealed clear gap structures in most of the disks (Huang et al., 2018a). Long et al. (2018a) surveyed 32 PPDs observed by ALMA in the Taurus star-forming region and identified gap and ring structures in 12 disks. Using ALMA archive data, van der Marel et al. (2019) also identified gaps for 16 diverse disk systems. Our sample is assembled from previously published data. Since we are interested in gaps that are possibly induced by planets, we select those gaps that are likely to be of planetary origin following Zhang et al. (2018) and Lodato et al. (2019). We also include the gaps in the HL Tau disk (Brogan et al., 2015). Our sample comprises of 35 disks with a total of 55 gaps.

Disk	M_*[a] ($M_\odot$)	L_* ($L_\odot$)	T_{gas}(100 au) (K)	h/R(100 au)	Gap index	R_{gap} (au)	Δ_{gap} (au)	Δ_{gap}/R_{gap}	h_{gap}/R_{gap}	Ref
Single-gap disks										
DM Tau	$0.35^{+0.05}_{-0.05}$	$0.2^{+0.03}_{-0.02}$	8.1	0.097	1	70.0	30.0	0.429	0.088	4
DN Tau	0.52	0.69	11.0	0.093	1	49.3	3.8	0.078	0.078	3
DS Tau	0.58	0.25	8.5	0.077	1	32.9	27.0	0.821	0.058	3
Elias 20	$0.48^{+0.15}_{-0.07}$	$2.24^{+1.31}_{-0.83}$	14.8	0.112	1	25.1	3.5	0.140	0.079	1,2
Elias 27	$0.49^{+0.2}_{-0.11}$	$0.91^{+0.64}_{-0.37}$	11.8	0.099	1	69.1	14.3	0.207	0.090	1,2
FT Tau	0.34	0.15	7.5	0.095	1	24.8	4.8	0.195	0.067	3
GW Lup	$0.46^{+0.12}_{-0.15}$	$0.33^{+0.19}_{-0.12}$	9.2	0.090	1	74.3	12.1	0.163	0.084	1,2
HD 135344B	$1.5^{+0.1}_{-0.1}$	$6.7^{+1.3}_{-2.9}$	19.4	0.072	1	73.0	6.0	0.082	0.067	4
HD 142666	$1.58^{+0.15}_{-0.04}$	$9.12^{+5.67}_{-3.5}$	21.0	0.073	1	16.0	3.5	0.219	0.046	1,2
HD 169142	$1.75^{+0.05}_{-0.05}$	$14^{+3.5}_{-5}$	23.4	0.074	1	42.0	20.0	0.476	0.059	4
HD 97048	$2.2^{+0.1}_{-0.1}$	$31.2^{+2.1}_{-6}$	28.6	0.072	1	125.0	90.0	0.720	0.077	4
IM Lup	$0.89^{+0.21}_{-0.23}$	$2.57^{+1.5}_{-0.95}$	15.3	0.083	1	117.4	15.8	0.135	0.087	1,2
IQ Tau	0.5	0.21	8.2	0.081	1	41.2	6.9	0.169	0.065	3
MWC 480	1.91	17.38	24.7	0.072	1	73.4	33.3	0.454	0.067	3
RU Lup	$0.63^{+0.2}_{-0.14}$	$1.45^{+0.85}_{-0.53}$	13.3	0.092	1	29.1	4.5	0.155	0.068	1,2
RXJ 1615.3-3255	$0.6^{+0.1}_{-0.1}$	$0.83^{+0.07}_{-0.07}$	11.5	0.088	1	92.5	35.0	0.378	0.087	4
RY Tau	2.04	12.3	22.6	0.067	1	43.4	4.9	0.112	0.054	3
SR 4	$0.68^{+0.19}_{-0.19}$	$1.17^{+0.69}_{-0.43}$	12.6	0.087	1	11.0	6.3	0.573	0.059	1,2
Sz 114	$0.17^{+0.04}_{-0.03}$	$0.2^{+0.12}_{-0.08}$	8.1	0.139	1	38.6	4.3	0.111	0.108	1,2
Sz 129	$0.83^{+0.06}_{-0.24}$	$0.44^{+0.26}_{-0.16}$	9.8	0.069	1	41.0	4.1	0.100	0.055	1,2
Sz 98	$0.6^{+0.1}_{-0.1}$	$1.1^{+0.2}_{-0.3}$	12.4	0.091	1	79.0	18.0	0.228	0.086	4
UZ Tau E	0.39	0.35	9.3	0.098	1	69.1	7.3	0.106	0.089	3
V1247 Ori	$1.95^{+0.15}_{-0.15}$	$20^{+2.7}_{-5.3}$	25.6	0.073	1	107.5	15.0	0.140	0.074	4
Multi-gap disks										
AA Tau	$0.65^{+0.15}_{-0.15}$	$0.56^{+0.2}_{-0.2}$	10.5	0.081	1	72.0	14.0	0.194	0.074	4
					2	118.0	16.0	0.136	0.084	
DoAr 25	$0.95^{+0.09}_{-0.34}$	$0.95^{+0.56}_{-0.35}$	11.9	0.071	1	98.0	15.5	0.158	0.071	1,2
					2	125.0	10.0	0.080	0.075	
Elias 24	$0.85^{+0.05}_{-0.05}$	$6.8^{+5.8}_{-3.2}$	19.5	0.096	1	55.0	20.0	0.364	0.083	4
					2	94.0	12.0	0.128	0.095	
GO Tau	0.36	0.21	8.2	0.096	1	58.9	22.9	0.389	0.084	3
					2	87.0	16.1	0.185	0.093	
HD 143006	$1.78^{+0.22}_{-0.3}$	$3.8^{+1.57}_{-1.11}$	16.9	0.062	1	22.0	21.7	0.986	0.042	1,2
					2	51.0	12.8	0.251	0.052	
AS 209	$0.83^{+0.24}_{-0.23}$	$1.41^{+0.83}_{-0.52}$	13.2	0.080	1	8.7	4.7	0.541	0.043	1,2,4
					2	60.8	15.5	0.255	0.071	
					3	93.0	18.0	0.194	0.079	
CI Tau	0.89	0.81	11.5	0.072	1	13.9	8.9	0.636	0.044	3
					2	48.4	10.9	0.225	0.060	
					3	119.0	22.1	0.186	0.075	
DL Tau	0.98	0.65	10.8	0.067	1	39.3	6.7	0.170	0.053	3
					2	67.0	13.8	0.207	0.061	
					3	88.9	25.9	0.292	0.065	
GY 91	$0.19^{+0.01}_{-0.01}$	$0.33^{+0.2}_{-0.2}$	9.2	0.140	1	41.0	14.0	0.341	0.112	4
					2	69.0	10.0	0.145	0.127	
					3	107.0	14.0	0.131	0.142	
HL Tau	1.0	$9.25^{+5.5}_{-5.5}$	21.1	0.092	1	11.8	9.5	0.809	0.054	Mix
					2	32.3	7.5	0.233	0.070	
					3	82.0	24.0	0.293	0.088	
V1094 Sco	$0.8^{+0.1}_{-0.1}$	$0.57^{+0.07}_{-0.13}$	10.5	0.073	1	60.0	10.0	0.167	0.064	4
					2	102.5	35.0	0.341	0.073	
					3	174.0	20.0	0.115	0.084	
HD 163296	$2.04^{+0.25}_{-0.14}$	$16.98^{+16.9}_{-8.47}$	24.5	0.070	1	10.0	3.2	0.320	0.039	1,2
					2	48.0	20.2	0.421	0.058	
					3	86.4	16.2	0.188	0.067	
					4	145.0	13.4	0.092	0.077	

[a] For HL Tau, we adopt the same stellar mass as Wang et al. (2020) adopted.
Reference. (1) Andrews et al. (2018); (2) Huang et al. (2018a); (3) Long et al. (2018a); (4) van der Marel et al. (2019).

Table 4.1: Properties of the disks and gaps

Basic properties of stars, disks and gaps of our sample are summarized in Table 4.1. Stellar properties of disks listed in Zhang et al. (2018) and Lodato et al. (2019) are based on Andrews et al. (2018) and Long et al. (2018a), respectively. For disks sampled by van der Marel et al. (2019), we use the same stellar properties except for those overlapped with the DSHARP disks. For HL Tau system, we keep using the same parameters as we adopted in our previous study Wang et al. (2020).

The stellar parameters can be used to estimate the disk temperature and the aspect ratio at a reference radius of $100\,\mathrm{au}$ following the temperature scaling relation by Dong et al. (2018a). We assume that both dust and gas components of the disk have approximately the same temperature $T_{\rm dust} \approx T_{\rm gas}$. Then, the disk temperature at radius R is given by

$$T(R) = 12.1\,\mathrm{K}\left(\frac{L_*}{\mathrm{L}_\odot}\right)^{1/4}\left(\frac{R}{100\,\mathrm{au}}\right)^{-1/2}, \tag{4.1}$$

where L_* is the stellar luminosity. Equation (4.1) is shown to be consistent with the results produced by previous radiative transfer models (e.g. Dong et al., 2015; Facchini et al., 2017). We would like to note here that the $T_{\rm dust}$ defined by equation (2) in the Appendix B of Dong et al. (2018a) indeed corresponds to the dust temperature at $R = 0.5R_{\rm mm}$ instead of $R = R_{\rm mm}$. Thus, our equation (4.1) is identical to their model (R. Dong, personal communication).

For locally isothermal disks where the ideal gas equation of state holds, the gas aspect ratio at R is then

$$\begin{aligned}\frac{h(R)}{R} &= \left(\frac{k_B T}{\mu m_p}\right)^{1/2}\Omega_K^{-1}R^{-1} \\ &= 0.07\left(\frac{L_*}{L_\odot}\right)^{1/8}\left(\frac{M_*}{M_\odot}\right)^{-1/2}\left(\frac{R}{100\,\mathrm{au}}\right)^{1/4},\end{aligned} \tag{4.2}$$

where μ is the mean molecular weight (we adopt $\mu = 2.3$), and m_p is the proton mass.

Table 4.1 also lists the properties of the gaps based on Huang et al. (2018a), Long et al. (2018a), and van der Marel et al. (2019). Again for overlapped systems (e.g. AS 209 and HD 163296), we adopt DSHARP data that have a higher angular resolution. The third gap of the AS209 disk is adopted from van der Marel et al. (2019), which combines the fine gap structure found by DSHARP into a single gap centered at $93\,\mathrm{au}$. For HL Tau, we keep using the same gap properties as we adopted in Wang et al. (2020).

Among the 35 disks, 23 disks are single-gap systems, and the rest are multi-gap systems. The width of the gap $\Delta_{\rm gap}$ is defined to be the difference between the outer and inner edges for systems adopted from van der Marel et al. (2019), and the gap location is set to be the midpoint of the outer and inner edges. We neglect all the inner cavities (i.e. gaps start at $0\,\mathrm{au}$), because the interpretation of such a structure remains unclear, making it difficult to deduce the mass or number of the potential planet(s) inside the cavity. We also calculate $\Delta_{\rm gap}/R_{\rm gap}$ and the gas aspect ratio $h_{\rm gap}/R_{\rm gap}$. Most of the gaps have widths greater than the scale heights, with the third gap of GY 91 as the only exception.

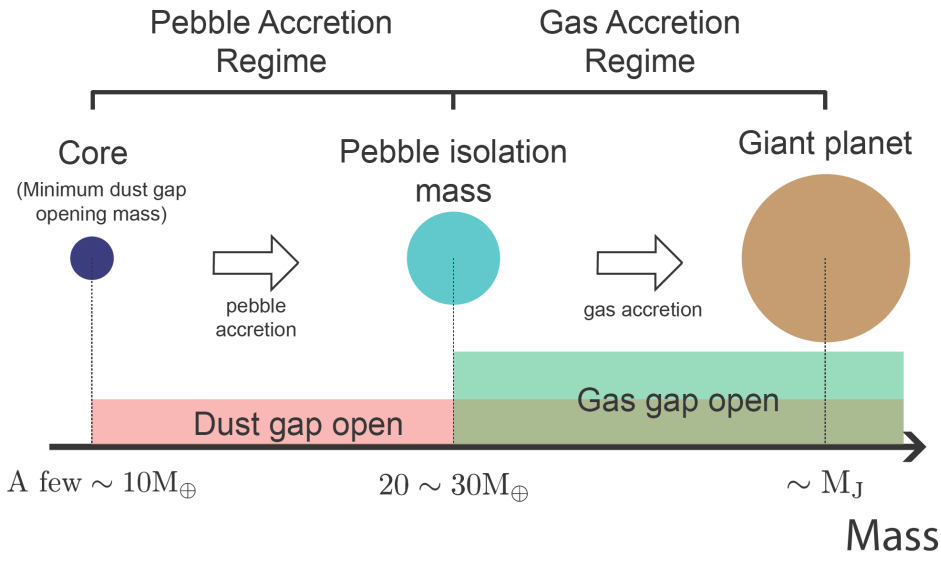

Figure 4.1: Schematic mass growth history of planets we considered in this study. A solid core is formed first and then grows via pebble accretion. The dust gap is opened at the minimum dust gap opening mass. After reaching the pebble isolation mass $M_{\rm iso}(R)$ at the location of the planet R, the pebble accretion process terminates and the gas accretion begins.

4.3 Methods

4.3.1 Mass accretion history of planets and pebble isolation mass

In the standard core-accretion scenario, a giant planet forms out of a small solid core, and grows via two-stage accretion processes as illustrated in Figure 4.1. At the first stage when its core mass is small, a planet mainly accretes solid materials from the surrounding disk. While it was believed that the accreting material at this stage is mainly km-size planetesimals (e.g. Safronov, 1969), recent studies (e.g. Ormel & Klahr, 2010; Ormel, 2017) suggested that the aerodynamically small particles with Stokes number between 10^{-3} and 1, so-called pebbles, may instead be the major source of accretion. In the following, we will use the terms "dust grains" and "pebbles" interchangeably.

As pebble accretion continues, the planet becomes more massive and starts to gravitationally interact with its surrounding disk with increasing strength. Several studies have suggested that the dust disk is more susceptible to gap opening torque than gas disk (e.g. Paardekooper & Mellema, 2004; Muto & Inutsuka, 2009; Rosotti et al., 2016). Before the planet is massive enough to generate a pressure maximum, it is possible to open a gap only in the dust disk through tidal torque and gas drag (Dipierro et al., 2016; Dipierro & Laibe, 2017). For instance, Rosotti et al. (2016) showed that even a planet with $15\,M_\oplus$ can open the dust gap without creating the pressure maximum. This result implies that dust gaps carved by planets above the minimum dust gap opening mass can be possibly observed by ALMA that is sensitive to millimeter-size dust particles. Once the dust gap

is opened, the planet loses access to the fraction of pebbles sensitive to the ALMA band. Nevertheless, until the planet reaches the pebble isolation mass $M_{\rm iso}$ and generates a gas pressure maximum, some pebbles may still cross the planetary orbit depending on their Stokes number.

The pebble accretion is a self-terminating process that ends when the planetary mass reaches a certain mass threshold, namely the pebble isolation mass (e.g. Lambrechts et al., 2014). At the pebble isolation mass, a planet is just massive enough to carve a shallow gas gap that generates a pressure maximum at the outer edge of the gap. Such a pressure maximum can trap *all* the pebbles with Stokes number > 0.005 (Bitsch et al., 2018), a range that effectively covers those pebbles that are most favourable to pebble accretion. The planet has no access to the inflow of the pebbles afterwards and the pebble accretion process is stopped. Since both the width and depth of the gas gap increase with the planetary mass, it is reasonable to expect that a relatively deep gas gap is formed once the planetary mass exceeds the pebble-isolation mass, and the dust gap is also strongly shaped by the gas gap due to the pressure maximum. Before reaching the pebble-isolation, it is reasonable to assume that a visible gap should be formed only in the dust disk because the gas gap is too shallow.

Three-dimensional hydrodynamical simulations by (Bitsch et al., 2018) indicate the pebble isolation mass $M_{\rm iso}(R)$ at the location of R from the central star, is written in terms of the stellar mass M_*, the aspect ratio of the disk h/R, the pressure gradient $\eta = \partial \ln P / \partial \ln R$, and the viscosity of the gas α as

$$M_{\rm iso}(R) = 25 M_\oplus \left(\frac{M_*}{M_\odot}\right) \left(\frac{h/R}{0.05}\right)^3 f(\alpha, \eta), \tag{4.3}$$

$$f(\alpha, \eta) = \left[0.34 \left(\frac{-3.0}{\log \alpha}\right)^4 + 0.66\right] \left(1 - \frac{\eta + 2.5}{6}\right). \tag{4.4}$$

Throughout this chapter, we consider locally isothermal disks with a temperature profile of $T \propto R^{-1/2}$ and a surface density profile of $\Sigma \propto R^{-1}$. We simply adopt the mid-plane pressure $P_{\rm mid} = \rho_{\rm mid} c_s^2 = (\Sigma/h) c_s^2$. Then we have $\eta = -2.75$ and the second bracket in equation (4.4) is $25/24$. It is worth to note that $M_{\rm iso}$ obtained from 2D simulations is scaled down by a factor of 1.5 due to the different treatments of the surface density profile (Bitsch et al., 2018, Appendix B). In this study, we nevertheless adopt $M_{\rm iso,3D}$ as the pebble isolation mass as we think it is more reliable while applying to real systems.

After reaching the pebble isolation mass, the gas envelop around the planet starts cooling, which triggers the run-away gas accretion that marks the beginning of the second stage. At this stage, the planet grows quickly via gas accretion and becomes a gas giant. As the planet continues to grow, it carves a deeper gap in the disk, and the gas accretion rate is slowed down. The accretion eventually stops when the PPD is dispersed due to both stellar accretion and photoevaporation.

4.3.2 Planetary mass estimation

The planetary formation picture illustrated in Figure 4.1 states that a planet opens a gap when it is massive enough. Since the properties of the gap is determined by the planet-disk interaction, one may infer the mass of the embedded planet from the parameters characterizing the gap morphology. Indeed, Kanagawa et al. (2016) performed a series of hydrodynamical simulations in the gas-gap open case, and found the following empirical relation for the mass of the embedded planet:

$$M_{\rm p,gas}(R_{\rm gap}) = 175 M_\oplus \left(\frac{M_*}{M_\odot}\right) \left(\frac{\Delta_{\rm gap}/R_{\rm gap}}{0.5}\right)^2 \left(\frac{h_{\rm gap}/R_{\rm gap}}{0.05}\right)^{3/2} \left(\frac{\alpha}{10^{-3}}\right)^{1/2}, \tag{4.5}$$

where $\Delta_{\rm gap}$, $h_{\rm gap}$ and $R_{\rm gap}$ are the width, scale-height and location of the gap. The empirical formula, equation (4.5), has been basically confirmed by Dong & Fung (2017).

It is important to note that $\Delta_{\rm gap}$ in equation (4.5) is defined for the gas profile in the original study. Therefore, while applying this mass prediction formula to those gaps observed in dust continuum, we need to assume that the gas gap has already opened, and its width roughly matches that of the dust gap due to good gas-dust coupling.

Zhang et al. (2018) carried out gas–dust hydrodynamic simulations and investigated the scaling relation between the planet mass and the width of the gap like equation (4.5). Overall their fitting is consistent to Equation (4.5) , though it is slightly deviated due to the decoupling between gas and dust when $St \gtrsim 10^{-2}$. Due to this deviation, Equation (4.5) may overestimate the planet mass. To take this difference into account, we include an uncertainly factor for the estimated mass as will be discussed in section 4.3.3. Also as will be seen in section 4.3.2, the estimated mass given by equation (4.5) agrees with that estimated by Zhang et al. (2018) within this level of uncertainly.

Before reaching the pebble-isolation mass, no significant gas gap is expected to form and only a dust gap is visible as described in section 4.3. Equation (4.5) is not relevant in order to estimate the mass of the embedded planet in such a dust-only gap regime. For instance, Figure 12 of Zhang et al. (2018) exhibits a large scatter of the range of small planetary mass (or small K'), which may possibly indicate the transition of the different scaling between the dust-only gap regime and gas gap regime that we assumed in this chapter. In the dust-only gap regime, the width of the dust gap would be better described by the Hill radius scaling, instead of equation (4.5).

The Hill radius model suggests that the gap width $\Delta_{\rm gap}$ is proportional to the the planetary Hill radius $R_{\rm H}$ at the gap location $R_{\rm gap}$. This relation can be rewritten for the planetary mass as

$$M_{\rm p,dust}(R_{\rm gap}) = 6.01 M_\oplus \left(\frac{C}{5.5}\right)^{-3} \left(\frac{M_*}{M_\odot}\right) \left(\frac{\Delta_{\rm gap}/R_{\rm gap}}{0.1}\right)^3, \tag{4.6}$$

where C is the proportional constant and previous studies indicate that $4.5 < C < 7$ (Rosotti et al., 2016). Following Lodato et al. (2019), we set $C = 5.5$ in this study.

The formulation of Zhang et al. (2018) is different from equation 4.5, but this different is mainly due to their own measurement of the gap width.

While equations (4.5) and (4.6) should connect to each other, the connection might not be smooth. Indeed, Rosotti et al. (2016) investigated both the dust-only gap case and relatively deep gas gap case and found the gap width can be nicely scaled by a single Hill radius (see Figure 16 of Rosotti et al. (2016)). Although their scaling result does not explicitly depend on any gas parameters, it implies that equation (4.6) may be valid even in the gas-gap opening regime for some specific setup. Investigation of the connection between the two scaling relations is beyond the scope of this thesis and should be taken care in the future work.

The above argument indicates that equation (4.5) is applicable only for a gaseous planet embedded in a disk with both dust and gas gaps, while equation (4.6) may be more relevant for a low mass planet with a dust gap alone. Unfortunately, the high-resolution disk substructure is available only for the dust component due to the difficulty of resolving the line emission from gas. Therefore, it is not easy to observationally distinguish between the two different predictions for the mass of embedded planets.

According to the planetary formation picture described in section 4.3.1, however, the pebble isolation mass $M_{\rm iso}$ may be used as a reasonable threshold of the planetary mass that is consistent with the presence or absence of the unobservable gas gap; if the predicted planetary mass is greater than $M_{\rm iso}$, the gas gap is likely to be opened as well.

Equation (4.5) implies that $M_{\rm p,gas} > M_{\rm iso}(R_{\rm gap})$ is translated into the lower limit of $(\Delta_{\rm gap}/R_{\rm gap})$:

$$\left(\frac{\Delta_{\rm gap}}{R_{\rm gap}}\right)_{\rm gas} > 0.189 \left[\frac{M_{\rm iso}(R_{\rm gap})}{25M_\oplus}\right]^{1/2} \left(\frac{M_*}{M_\odot}\right)^{-1/2} \left(\frac{h_{\rm gap}/R_{\rm gap}}{0.05}\right)^{-3/4} \left(\frac{\alpha}{10^{-3}}\right)^{-1/4}. \tag{4.7}$$

Thus, if $(\Delta_{\rm gap}/R_{\rm gap})$ of the observed *dust* gap satisfies the above inequality (4.7), the gap is likely expected to be associated with the *gas* gap of the similar value of $(\Delta_{\rm gap}/R_{\rm gap})_{\rm gas}$. Thus equation (4.5) provides a reasonably good mass estimate of the embedded planet.

Similarly, equation (4.6) implies that $M_{\rm p,dust} < M_{\rm iso}(R_{\rm gap})$ is rewritten as

$$\left(\frac{\Delta_{\rm gap}}{R_{\rm gap}}\right)_{\rm dust} < 0.161 \left[\frac{M_{\rm iso}(R_{\rm gap})}{25M_\oplus}\right]^{1/3} \left(\frac{M_*}{M_\odot}\right)^{-1/3}. \tag{4.8}$$

If a dust gap satisfies the inequality (4.8), it is likely to be a dust-only gap, and equation (4.6) may be preferred to predict the mass of the embedded planet.

The above argument offers a possibility to distinguish between the presence and absence of the gas gap with the similar profile of the observed dust gap. In reality, however, the mass predictions suffer from significant uncertainties for multiple reasons. The major uncertainty comes from the gap width $\Delta_{\rm gap}$. Rosotti et al. (2016) found that the gap profile in their simulations changes in a time-dependent fashion, and the observed gap width would vary accordingly, which leads to a factor of 2-3 uncertainty for the planetary mass prediction. Also equation (4.5) derived by Kanagawa et al. (2016) depends on the coupling strength between dust and gas components in the disk, which would affect its overall normalization. Furthermore, the definitions of the inner and outer boundaries of the gap are not unique, and vary among different papers. Finally, the host stars in PPDs are generally young, and their luminosities and masses cannot be well constrained from the stellar evolution model. Therefore, we have to keep in mind such uncertainties in

	C1	C2	Interpretation	Mass adopted	Number of gaps		
					$\alpha = 10^{-2}$	$\alpha = 10^{-3}$	$\alpha = 10^{-4}$
Group I	Yes	No	Dust only gaps	$M_{\rm p,dust}$	18	21	36
Group II	No	Yes	Dust/Gas gaps	$M_{\rm p,gas}$	11	19	19
Group III	Yes	Yes	Indistinguishable	$M_{\rm p,dust}$, $M_{\rm p,gas}$	26	15	0
Group IV	No	No	Non-planetary?	-	0	0	0

Table 4.2: Criteria to classify the gaps into four groups.

interpreting inequalities (4.7) and (4.8).

4.3.3 Gap classification for improved mass prediction

Due to various uncertainties of the observed dust profiles, we introduce fudge factors in the planetary mass predictions. Specifically, we impose the following criteria (hereafter "C1" and "C2") for the dust only gap and for the gas gap, respectively:

$$\textit{C1}\ \text{(dust gap)}: \quad \frac{M_{\rm p,dust}}{M_{\rm iso}} < F_1 \tag{4.9}$$

$$\textit{C2}\ \text{(gas gap)}: \quad \frac{M_{\rm iso}}{M_{\rm p,gas}} < F_2, \tag{4.10}$$

where F_1 and F_2 are the fudge factors. Substituting equations (4.3), (4.5) and (4.6), inequalities (4.9) and (4.10) are rewritten as the relations between $\Delta_{\rm gap}/R_{\rm gap}$ and $h_{\rm gap}/R_{\rm gap}$:

$$\textit{C1}: \quad \log\left(\frac{\Delta_{\rm gap}}{R_{\rm gap}}\right) < \log\left(\frac{h_{\rm gap}}{R_{\rm gap}}\right) + \frac{1}{3}\log f(\alpha) + \frac{1}{3}\log F_1 + 0.507 \tag{4.11}$$

$$\textit{C2}: \quad \log\left(\frac{\Delta_{\rm gap}}{R_{\rm gap}}\right) > 0.75\log\left(\frac{h_{\rm gap}}{R_{\rm gap}}\right) + \frac{1}{2}\left[\log f(\alpha) - 0.5\log\alpha\right] - \frac{1}{2}\log F_2 - 0.498, \tag{4.12}$$

According to the two criteria C1 and C2, the observed gaps are classified into four groups on $h_{\rm gap}/R_{\rm gap} - \Delta_{\rm gap}/R_{\rm gap}$ plane, as schematically illustrated in Figure 4.2 and summarized in Table 4.2. While the relevant choice of the fudge factors is not clear, we adopt $F_1 = F_2 = 2$ below, just for simplicity.

On the basis of the classification, we can interpret the nature of the gap. Group I implies that the observed dust gap is not associated with a gas gap, and equation (4.6) is preferred for the planetary mass estimate. Group II, on the other hand, implies that the disk has a gas gap as well, and equation (4.5) is a reasonable estimate for the embedded gas planet. Gaps in group III are consistent with both interpretations and we cannot distinguish between the two possibilities $M_{\rm p,dust}$ and $M_{\rm p,gas}$, unless the presence or absence of the gas gap is clarified observationally.

Finally, gaps in group IV are inconsistent with either interpretation. Such gaps may be of non-planetary origin, or it may simply point to a possible inaccuracy or limitation of the mass prediction models that we adopted here. In this context, it is interesting to note that there is no gap classified as group IV in our sample. More details of the

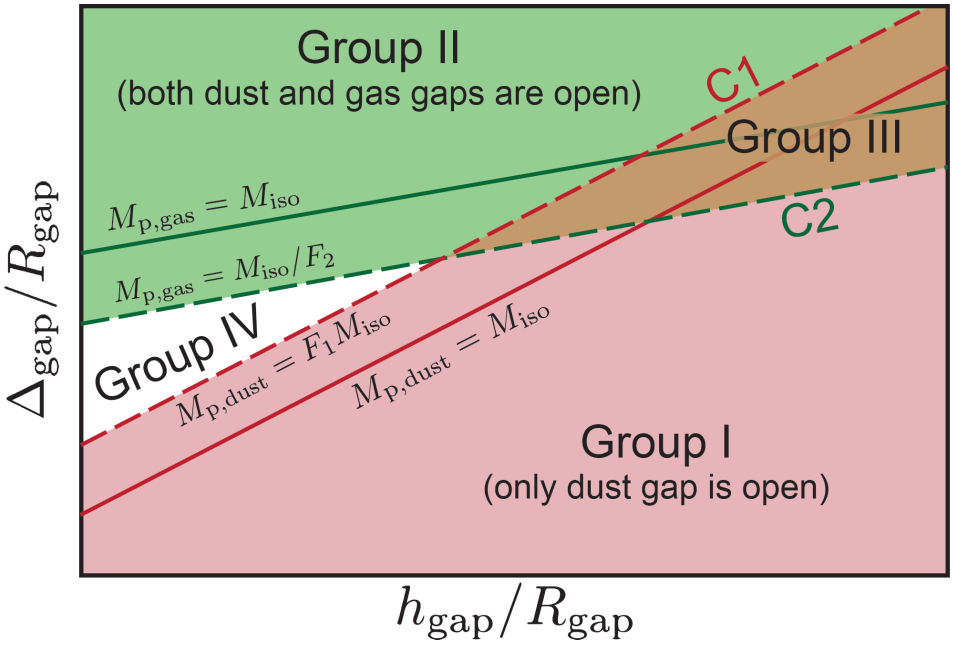

Figure 4.2: Schematic illustration of the gap classification

interpretation of the groups will be be discussed in the next subsection, where we show how the gap width varies with planetary mass at three different locations of a disk.

4.3.4 Interpretation of gap classifications at fixed locations

In this subsection, we schematically illustrate the relation between observed gap width $\Delta_{\rm gap}$ and planetary mass $M_{\rm p}$ at three different locations of a disk, and show how the relation corresponds to the interpretations of the different gap groups. As shown by Figure 4.3 (a), we choose three different $h_{\rm gap}/R_{\rm gap}$ values that correspond to three fixed locations A, B and C on a disk. At each location, we consider how $\Delta_{\rm gap}$ varies with the $M_{\rm p}$, as plotted in Figure 4.3 (b), (c) and (d).

According to the planetary formation scenario that we assumed, if $M_{\rm p}$ is smaller than $M_{\rm iso}$, the gap is considered to be dust-only gap and $M_{\rm p} = M_{\rm p,dust} \propto \Delta_{\rm gap}^3$ (red solid line) given by equation (4.6); otherwise, the gap is considered to open in both the gas and dust disks, therefore $M_{\rm p} = M_{\rm p,gas} \propto \Delta_{\rm gap}^2$ (green solid line) as described by equation (4.7). The uncertainty of the predicted mass is also taking into account: the red dashed line extends to the upper limit of the mass prediction if the gap is in the dust gap regime, and the green dashed line extends to the lower limit of the mass prediction if the gap is in the gas gap regime. From Figure 4.3 (b), (c) and (d), the relative positions of the red line and green line are different at different disk locations.

In case A, the projections of the red and green lines onto the y-axis do not span the whole range of $\Delta_{\rm gap}$. Therefore, any gap width within the grey region does not correspond to any planetary mass. In other words, if a gap is observed at such a width, we can exclude it from the planetary origin, which implies the interpretation of the group IV. This conclusion is the direct consequence if we apply our mass prediction formulae and

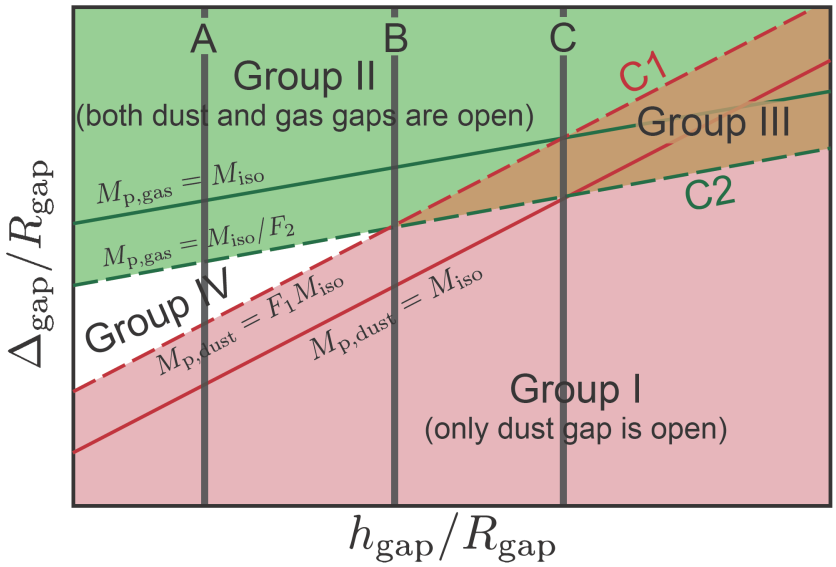

(a)

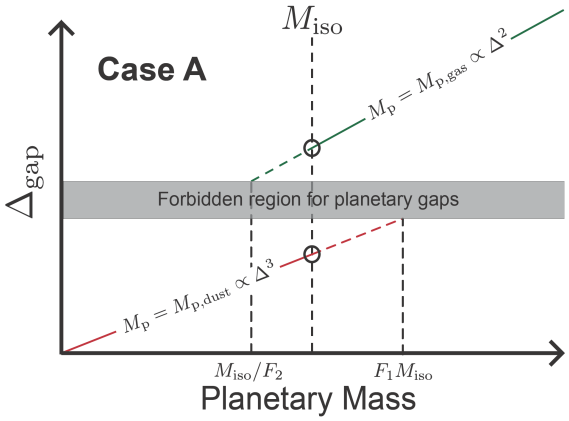

(b)

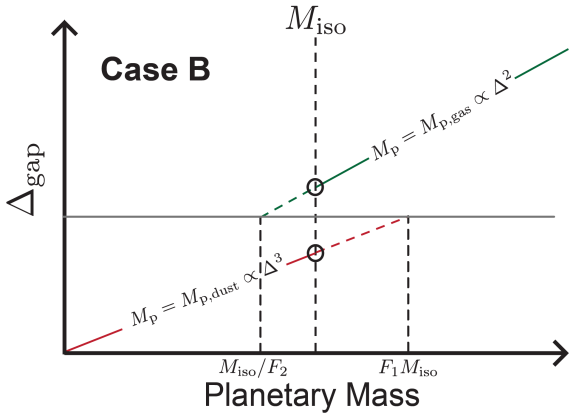

(c)

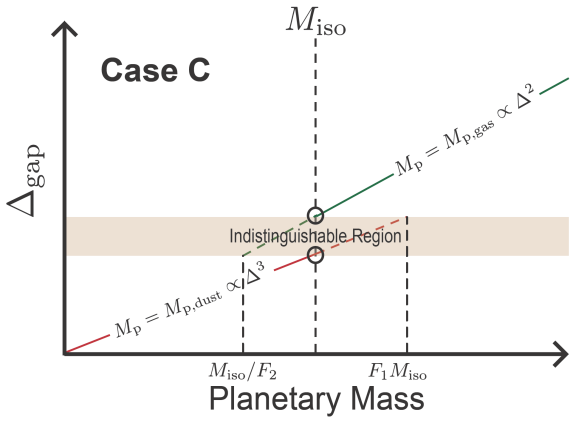

(d)

Figure 4.3: (a) Same as figure 4.2 but with A, B, C lines indicting three fixed locations at the same disk. (b)(c)(d): Gap width against planetary mass at location A, B and C. The axis of the plots are in arbitrary units and do not have the same scale.

adopt the planetary formation picture in section 4.3.1. It is possible that this zero-th order discontinuity of the $\Delta_{\rm gap}$-$M_{\rm p}$ relation is not physical but simply due to our poor knowledge of how the gap width changes around $M_{\rm iso}$. In reality, the sudden shift around $M_{\rm iso}$ may be replaced by a continuous curve that smoothly connects two regimes. In this case, the planetary interpretation of the gap is not excluded.

In case B, the projections of the red and green lines onto the y-axis span the entire range of y-axis without any overlapping. This case contains no degeneracy, as an arbitrary gap width can always be uniquely explained by a planetary mass, and thus there is no ambiguity about how to interpret the nature of the gap.

In case C, although the projections of the red and green lines onto the y-axis together cover the entire range of y-axis, there is an overlap that corresponds to the indistinguishable region. If we observe a gap whose width falls into this region, there are two possible mass predictions corresponding to dust gap alone interpretation and gas gap interpretation respectively. Gaps in this indistinguishable region are classified as group III gaps.

4.4 Results

4.4.1 Classification of the gaps at $\alpha = 10^{-3}$

According to C1 and C2, we classify the gaps into groups I to IV as shown in Figure 4.4. The red and green regions correspond to group I (dust-gap only) and group II (gas-gap opened) gaps respectively, and the overlapped region (light-brown) bounded by equations (4.9) and (4.10) is group III in which both interpretations are possible. We adopt the fiducial value of the viscosity, $\alpha = 10^{-3}$. The relations of $M_{\rm p,dust} = M_{\rm iso}$ and $M_{\rm p,gas} = M_{\rm iso}$ are plotted in red and green lines, respectively. The quoted error-bars of each symbol along the y-axis is estimated from the 1σ uncertainties of $R_{\rm gap}$ and $\Delta_{\rm gap}$ listed in previous studies. If they are not available, we do not plot the error-bar.

The result shows that out of 55 gaps, there are 21 gaps in group I, 19 gaps in group II and 15 gaps in group III, i.e., more than two-thirds (73%) of the gaps are classified as either dust-only gaps or gas gaps according to our criteria. The majority (52%) of the gaps in single-gap disks are classified as dust-only gaps, which are also the dominant group in the multi-gap disks. It should be noted that when the predicted planetary mass is close to $M_{\rm iso}$, the gap classification becomes sensitive to the adopted model of temperature and aspect ratio. Only one gap is below the dashed line $\Delta_{\rm gap} = h_{\rm gap}$, which is the minimum dust gap width for the Stokes number $St = 1$. If this gap is opened by a planet, the coupling between the dust and gas should be weak with $St > 1$ (Dipierro & Laibe, 2017; Lodato et al., 2019). While we give mass predictions to this gap as well, it may be of non-planetary origin.

The distribution of the gaps from both single-gap disks and multi-gap disks shows that gaps with small aspect ratios (and thus at the inner region) are more likely to be gaps that are opened in both gas and dust disks. In the outer region where the aspect ratio is larger, the gaps are more likely to be dust alone. This trend is more clearly seen in the

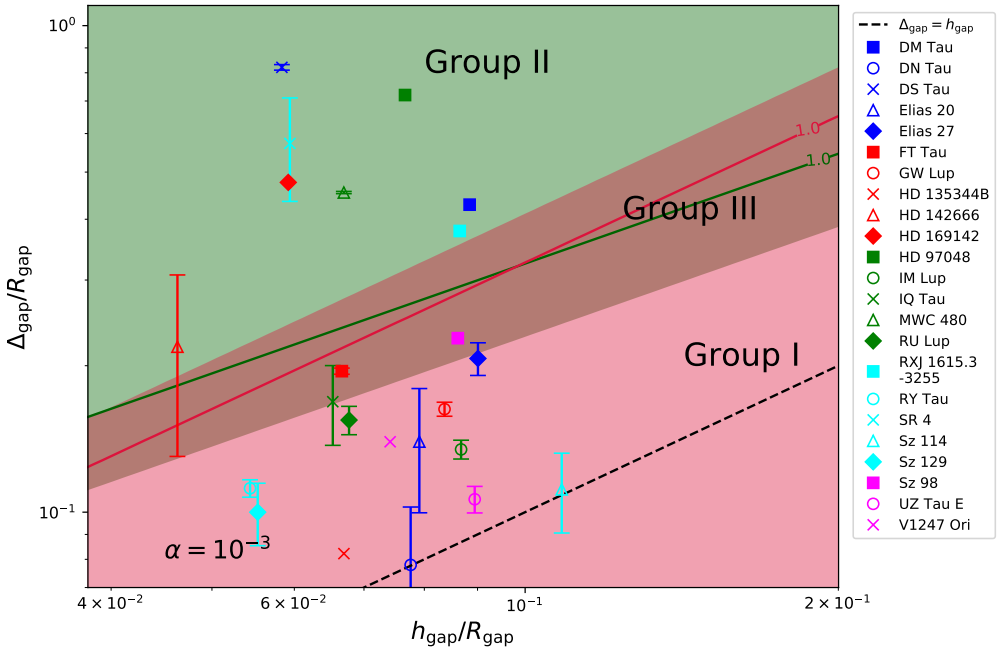

(a) Single-gap disk systems

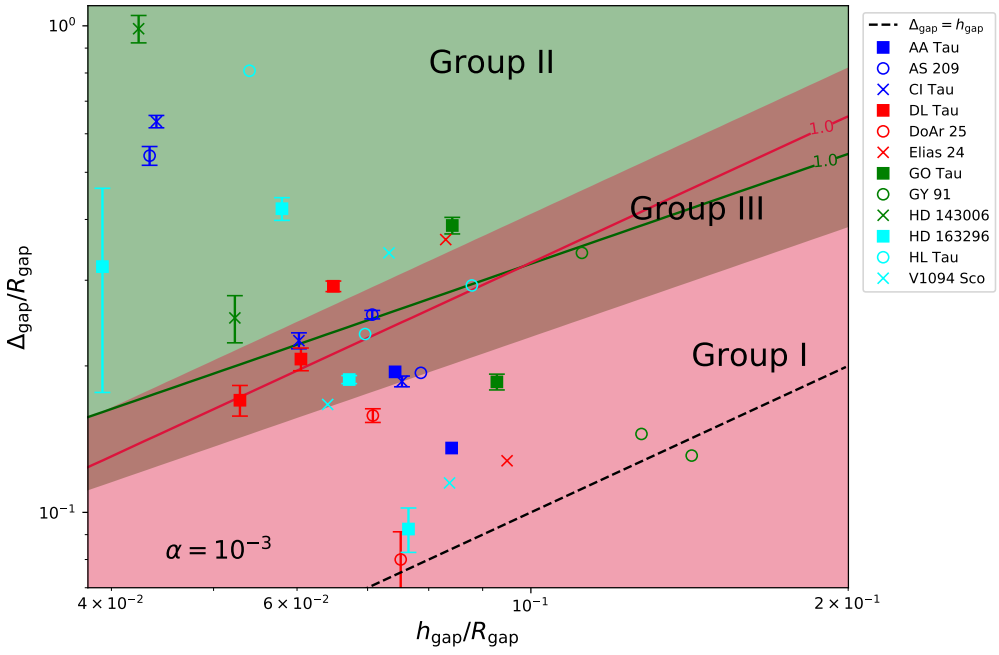

(b) Multi-gap disk systems

Figure 4.4: Classification of the gaps at $\alpha = 10^{-3}$. Figure above shows the gaps from single-gap systems, and figure below show those from multi-gap systems. Group I, II and III correspond to red, green and brown regions. There is no group IV region at the given range of the data. The red line represents $M_{\rm p,dust}/M_{\rm iso} = 1.0$. The green line represents $M_{\rm p,gas}/M_{\rm iso} = 1.0$. The black dashed line represents $\Delta_{\rm gap} = h_{\rm gap}$. The brown region is bounded by criteria C1 (equation 4.9) and C2 (equation 4.10).

case of multi-gap disks (bottom panel of Figure 4.4), which may be attributed to presence of the planet-planet interaction in a multi-planetary system.

4.4.2 Planetary mass predictions

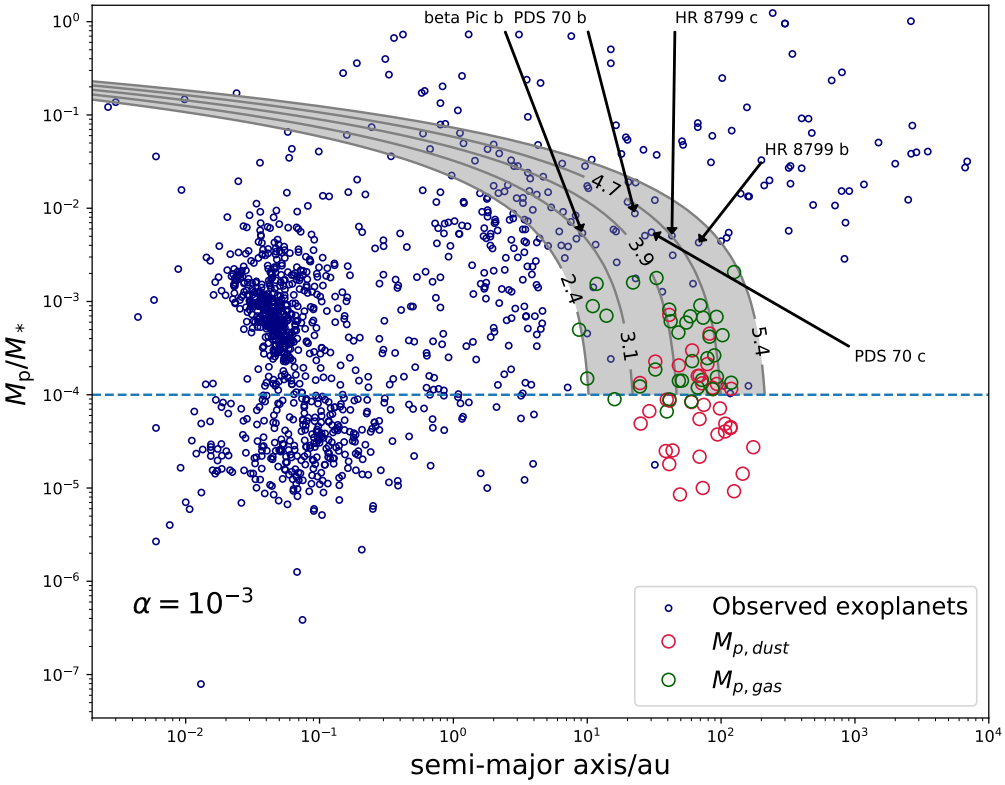

Figure 4.5: Compare the predicted masses ($\alpha = 10^{-3}$) with the observed population of exoplanets whose semi-major axis and mass are both confirmed. The red dots are $M_{\rm p,dust}$ when only dust gap is opened, while green dots are $M_{\rm p,gas}$ when both gas/dust gaps have been opened. If a gap is in group III (indistinguishable), both predictions are plotted. The grey lines are the evolution tracks introduced by Tanaka et al. (2020), and the number labels are constants $\mathcal{C}$ in equation (4.13). Since the evolution model is only applicable to gas accretion planets, we set the lower limit of the evolution tracks to be 10^{-4}.

We estimate planetary masses in the observed disk gaps according to our gap classification, assuming that planets are fully responsible for creating the gap substructures, and gaps and planets are in one-to-one correspondence. The mass prediction result is summarized in Table 4.3. In the case of group III, we list both $M_{\rm p,dust}$ and $M_{\rm p,gas}$.

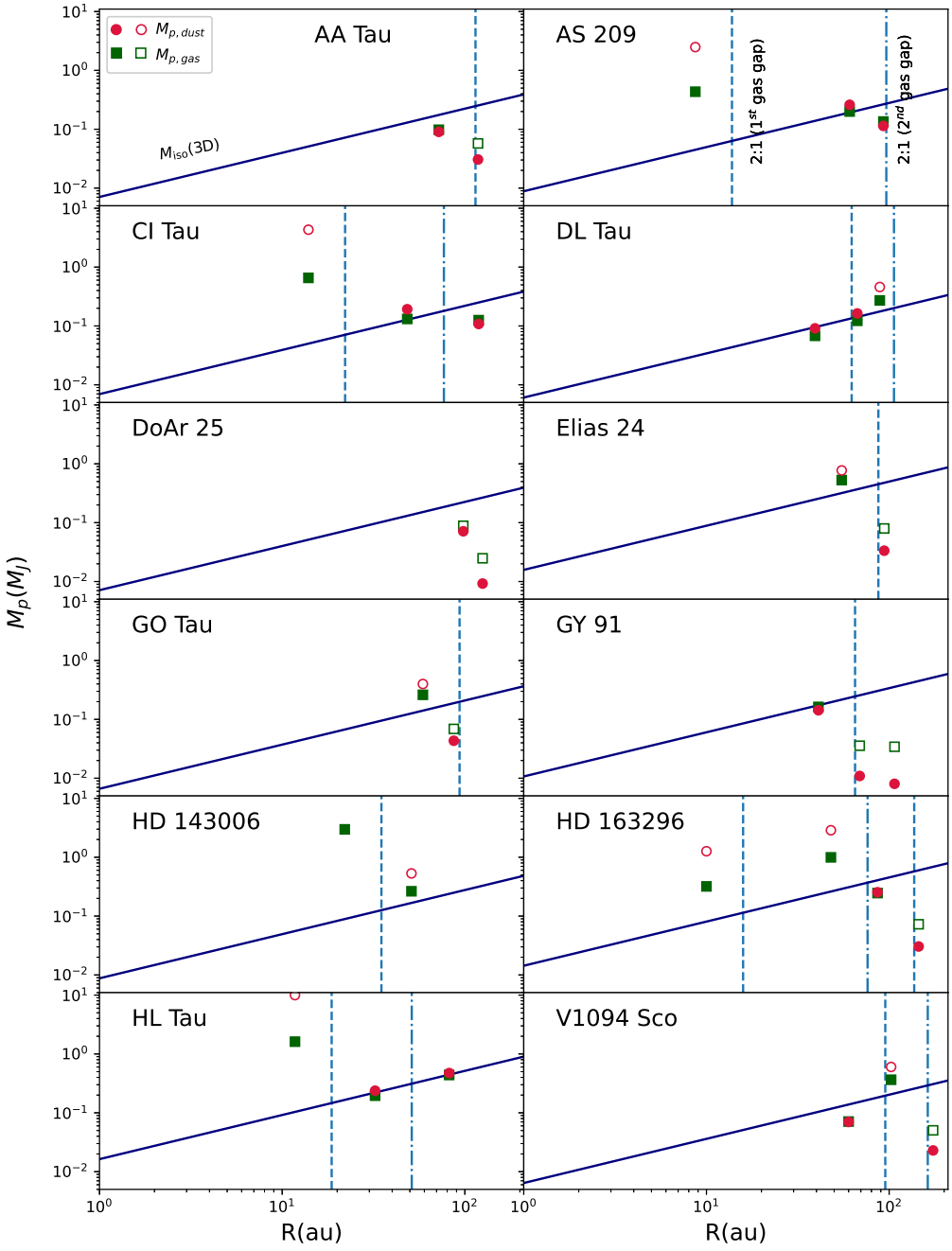

Figure 4.6: Configuration of the predicted planetary systems of the multi-gap disks ($\alpha = 10^{-3}$). The solid and dashed blue line shows the pebble isolation mass obtained from 3D simulations (Bitsch et al., 2018). If the predicted mass does not satisfy the corresponding criterion, an empty marker is used; otherwise, a filled marker is used. The dashed vertical lines indicate the position of the outer 2:1 period ratio for inner planets that have opened gas gaps. We use two line styles to denote the 2:1 lines from different planets.

Disk	Gap index	$\alpha = 10^{-2}$			$\alpha = 10^{-3}$			$\alpha = 10^{-4}$		
		Group	$M_{\rm p,dust}(\rm M_J)$	$M_{\rm p,gas}(\rm M_J)$	Group	$M_{\rm p,dust}(\rm M_J)$	$M_{\rm p,gas}(\rm M_J)$	Group	$M_{\rm p,dust}(\rm M_J)$	$M_{\rm p,gas}(\rm M_J)$
Single-gap systems										
DM Tau	1	III	0.520	1.052	II	-	0.333	II	-	0.105
DN Tau	1	I	0.005	-	I	0.005	-	I	0.005	-
DS Tau	1	II	-	3.429	II	-	1.084	II	-	0.343
Elias 20	1	I	0.025	-	I	0.025	-	I	0.025	-
Elias 27	1	III	0.082	0.353	I	0.082	-	I	0.082	-
FT Tau	1	III	0.048	0.138	III	0.048	0.044	I	0.048	-
GW Lup	1	I	0.037	-	I	0.037	-	I	0.037	-
HD 135344B	1	I	0.016	-	I	0.016	-	I	0.016	-
HD 142666	1	III	0.313	0.470	II	-	0.149	II	-	0.047
HD 169142	1	II	-	3.557	II	-	1.125	II	-	0.356
HD 97048	1	II	-	15.062	II	-	4.763	II	-	1.506
IM Lup	1	I	0.041	-	I	0.041	-	I	0.041	-
IQ Tau	1	III	0.045	0.148	III	0.045	0.047	I	0.045	-
MWC 480	1	II	-	4.241	II	-	1.341	II	-	0.424
RU Lup	1	III	0.044	0.165	I	0.044	-	I	0.044	-
RXJ 1615.3-3255	1	III	0.614	1.360	II	-	0.430	II	-	0.136
RY Tau	1	I	0.054	-	I	0.054	-	I	0.054	-
SR 4	1	II	-	1.415	II	-	0.447	II	-	0.141
Sz 114	1	I	0.005	-	I	0.005	-	I	0.005	-
Sz 129	1	I	0.016	-	I	0.016	-	I	0.016	-
Sz 98	1	III	0.134	0.490	III	0.134	0.155	I	0.134	-
UZ Tau E	1	I	0.009	-	I	0.009	-	I	0.009	-
V1247 Ori	1	I	0.100	-	I	0.100	-	I	0.100	-
Multi-gap systems										
AA Tau	1	III	0.090	0.310	III	0.090	0.098	I	0.090	-
AA Tau	2	I	0.031	-	I	0.031	-	I	0.031	-
DoAr 25	1	III	0.071	0.280	I	0.071	-	I	0.071	-
DoAr 25	2	I	0.009	-	I	0.009	-	I	0.009	-
Elias 24	1	III	0.772	1.673	II	-	0.529	II	-	0.167
Elias 24	2	I	0.033	-	I	0.033	-	I	0.033	-
GO Tau	1	III	0.399	0.827	II	-	0.262	II	-	0.083
GO Tau	2	I	0.043	-	I	0.043	-	I	0.043	-
HD 143006	1	II	-	9.415	II	-	2.977	II	-	0.942
HD 143006	2	III	0.531	0.836	II	-	0.264	II	-	0.084
AS 209	1	II	-	1.373	II	-	0.434	II	-	0.137
AS 209	2	III	0.260	0.632	III	0.260	0.200	I	0.260	-
AS 209	3	III	0.114	0.428	III	0.114	0.135	I	0.114	-
CI Tau	1	II	-	2.075	II	-	0.656	II	-	0.208
CI Tau	2	III	0.192	0.416	III	0.192	0.132	I	0.192	-
CI Tau	3	III	0.108	0.397	III	0.108	0.125	I	0.108	-
DL Tau	1	III	0.091	0.215	III	0.091	0.068	I	0.091	-
DL Tau	2	III	0.163	0.387	III	0.163	0.122	I	0.163	-
DL Tau	3	III	0.459	0.858	II	-	0.271	II	-	0.086
GY 91	1	III	0.143	0.515	III	0.143	0.163	I	0.143	-
GY 91	2	I	0.011	-	I	0.011	-	I	0.011	-
GY 91	3	I	0.008	-	I	0.008	-	I	0.008	-
HL Tau	1	II	-	5.116	II	-	1.618	II	-	0.512
HL Tau	2	III	0.238	0.618	III	0.238	0.195	I	0.238	-
HL Tau	3	III	0.474	1.389	III	0.474	0.439	I	0.474	-
V1094 Sco	1	III	0.070	0.225	III	0.070	0.071	I	0.070	-
V1094 Sco	2	III	0.602	1.153	II	-	0.365	II	-	0.115
V1094 Sco	3	I	0.023	-	I	0.023	-	I	0.023	-
HD 163296	1	II	-	1.010	II	-	0.320	II	-	0.101
HD 163296	2	II	-	3.147	II	-	0.995	II	-	0.315
HD 163296	3	III	0.254	0.779	III	0.254	0.246	I	0.254	-
HD 163296	4	I	0.030	-	I	0.030	-	I	0.030	-

Table 4.3: Planetary mass estimated from the gaps

Case with fiducial $\alpha = 10^{-3}$

The predicted planetary mass ranges from $1.6\,\mathrm{M}_\oplus$ to $4.8\,\mathrm{M}_\mathrm{J}$, but with significant diversities. Figure 4.5 plots the distribution of the planets, M_p/M_* against the semi-major axis for $\alpha = 10^{-3}$. We also plot the observed exoplanet population (extracted from exoplanet.eu, as of March 2021) with confirmed planetary mass, semi-major axis and stellar mass for comparison. We specifically label several widely-separated giant planets observed by direct imaging including HR 8799, β Pictoris and PDS 70, which would be relevant to compare with our prediction.

Figure 4.5 indicates that our predicted planets are located in a fairly distinct region relative to that of the observed population. It may imply that these observed planets have experienced significant inward orbital migration before the disk dispersal due to disk-planet interaction (Zhang et al., 2018; Lodato et al., 2019). Furthermore, their mass should have increased via accretion during the migration. A possible model of such evolutionary tracks is introduced by Tanaka et al. (2020), which suggests the following relation between mass and semi-major axis:

$$\ln\left(\frac{R_p}{1\,\mathrm{au}}\right) + \frac{2}{3}\left(\frac{M_p}{0.011 M_*}\right)^{2/3} = \mathcal{C}, \tag{4.13}$$

where $\mathcal{C}$ is a constant. Just for reference, we plot examples of the tracks with the range of $\mathcal{C}$ values that match our predicted planets. While a fraction of observed planets is consistent with the evolutionary tracks, a majority of them is far outside of the region that the simply model predicts. At this point, the reason of the discrepancy is not clear, and more detailed study of their evolution is necessary, which we plan to show elsewhere.

The architecture of the planets predicted from the multi-gap systems is shown in Figure 4.6. Mass predictions based on $M_{\mathrm{p,dust}}$ and $M_{\mathrm{p,gas}}$ are plotted in circles and squares, respectively. The filled (open) symbols indicate that they are consistent (inconsistent) with the criteria C1 and C2. The pebble isolation mass is also indicated by a straight line. As mentioned before, the planetary mass of most disks generally decreases against R, except the cases of DL Tau, HD 163296, HL Tau and V1094 SCO: the masses of the three planets in the DL Tau system increase with R; for the rest of the systems, there exist at least one pair of planets that does not follow the trend. We found planets that violate this trend are always gas-gap planets. If an outer planet forms first and later approaches the inner planet via inward migration, it may start runaway gas accretion earlier than the inner planet and quench its growth by shielding the gas flow. This implies that the architecture of a multi-planetary system is sensitive to its initial configuration.

Figure 4.6 also plots the locations of the outer 2:1 resonance period for the inside gas-gap planets (including marginal ones in group III) in dashed vertical lines. In many systems (i.e. AA Tau, AS 209, GY 91, Elias 24, DL Tau, GO Tau, HD 163296 and V1094 SCO) the gas-gap planet has a dust-gap planet close to its 2:1 period ratio. It may be due to the fact that the dust-gap planet is likely to form at the 2:1 resonance place of the gas-gap (or relatively large) planet. Alternatively, such a configuration can be the consequence of the combination of planetary migration and resonance trap. These mass orders may be related to alternative formation scenarios of planets, which will be discussed in the next section.

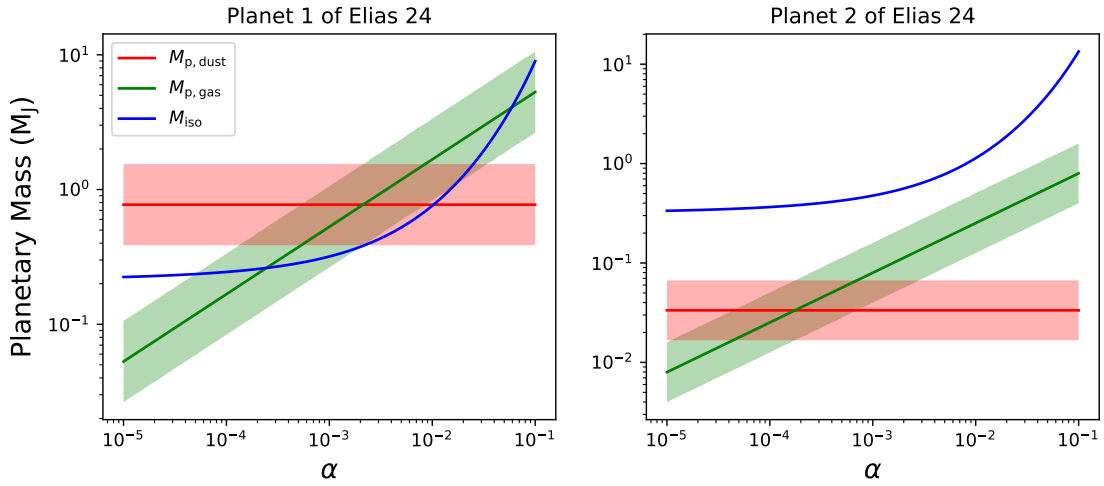

Figure 4.7: $M_{\rm p,dust}$ (red line), $M_{\rm iso}$ (blue line) and $M_{\rm p,gas}$ (green line) against α in Elias 24 disk. The shaded region covers a factor of two uncertainty of the mass prediction.

The α dependence

So far we have adopted the fiducial α value 10^{-3}. In fact, however, both $M_{\rm p,gas}$ and $M_{\rm iso}$ depend on α, and different values of α affect both classification criteria and the predicted mass. To investigate the α dependence, we calculate the planetary masses when $\alpha = 10^{-4}$ and 10^{-2} in addition to the fiducial value and list the results in Table 4.3. We also present the gap classification results plotted by figure 4.8. When the α is lower, C2 is less likely to be satisfied as $M_{\rm p,gas}$ is scaled by $\alpha^{1/2}$, so more gaps are classified as dust-only gaps (group I). As α increases, in contrast, $M_{\rm p,gas}$ increases and $M_{\rm p,dust}/M_{\rm iso}$ decreases, therefore both C1 and C2 are easier to be satisfied, and the number of indistinguishable gaps (group III) increases.

To illustrate the α-dependence, we choose Elias 24 as an example. Figure 4.7 shows how the mass changes for the gaps in Elias 24 system by varying α. For gap 1 (innermost gap), when $5 \times 10^{-5} < \alpha < 2 \times 10^{-3}$, $M_{\rm p,dust}/2 < M_{\rm iso}$ is not satisfied, while $2M_{\rm p,gas} > M_{\rm iso}$ is satisfied. Therefore, only the gas gap interpretation is valid and the gap is in group II. In the range $2 \times 10^{-3} \leq \alpha$, both dust gap and gas gap interpretations are valid, therefore the gap is in group III. However for gap 2 (outer gap), the condition $M_{\rm iso} > 2M_{\rm p,gas}$ holds for all range of α, therefore the gap cannot be interpreted as a gas gap and is always in group I. Note that the original viscosity range in Bitsch et al. (2018) is $10^{-4} \leq \alpha \leq 10^{-2}$. Outside of this range, the prediction of $M_{\rm iso}$ becomes an extrapolation of Bitsch et al. (2018) that may be not accurate.

We note that while $M_{\rm p,dust}$ defined by equation (4.6) does not exhibit any explicit dependence on α, it should depend on α in reality. In the strong coupling limit, the dust particles would depend on α similar as the gas, *i.e.*, $\propto \alpha^{1/4}$ indicated by equation (4.5). If the dust grains are only weakly coupled to the gas, on the other hand, the α-dependence should vanish for large St (in the limit $\alpha/{\rm St} \to 0$) as indicated by Dipierro & Laibe (2017). The dust particles visible in the ALMA band fall within these two limits, and therefore the α-dependence of $M_{\rm p,dust}$ should be small and does change our current result. Moreover, $M_{\rm p,dust}$ should depend on the Stokes number St as well as α. In a weakly coupled

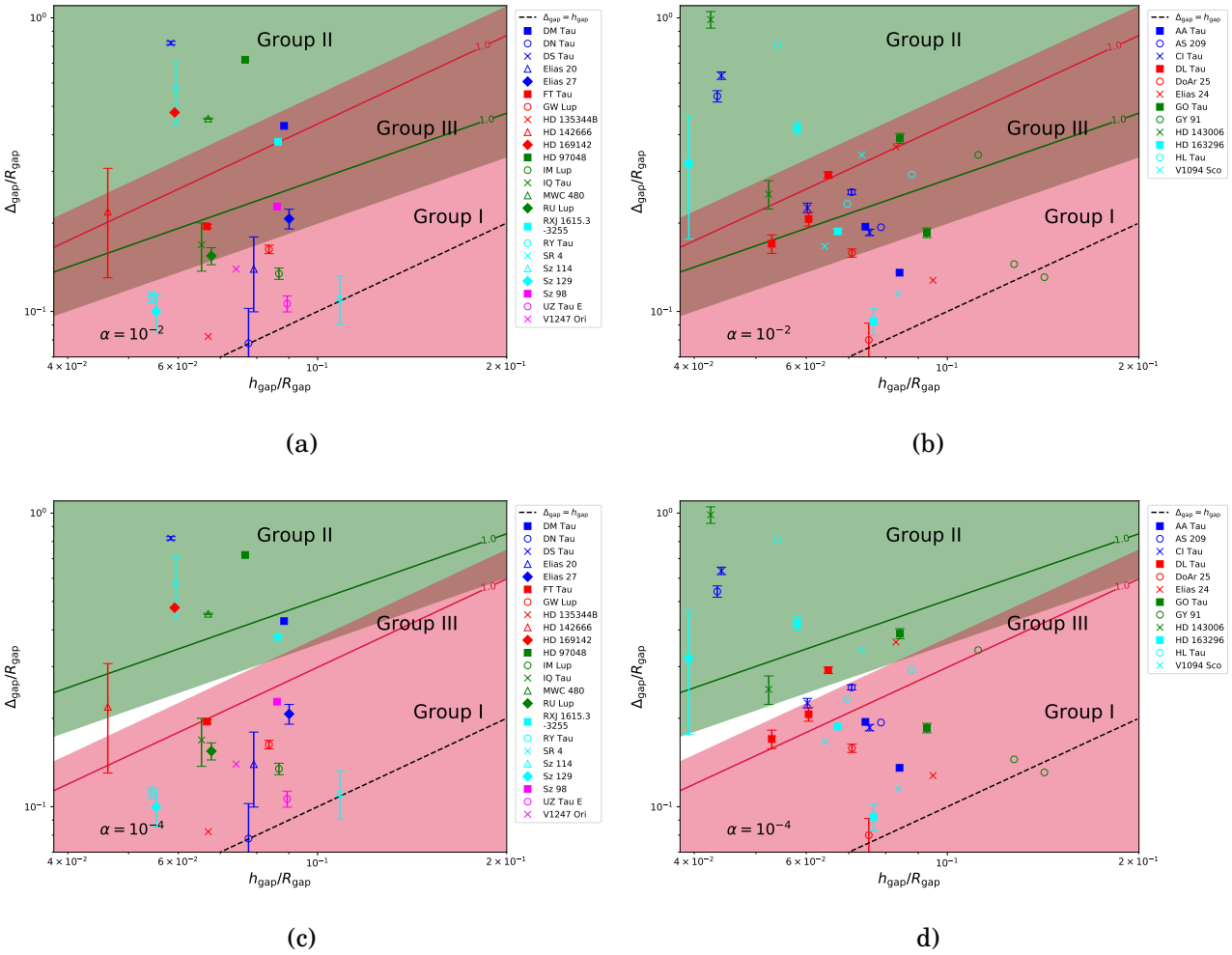

(a) (b)

(c) d)

Figure 4.8: (a)(b): Same as Figure 4.4 but with $\alpha = 10^{-2}$. (c)(d): Same as Figure 4.4 but with $\alpha = 10^{-4}$.

dust regime, Dipierro & Laibe (2017) suggest that the dust gap width only weakly depends on $St^{1/4}$, so the planetary mass can still be fairly well constrained even if an order of magnitude variance of St is taken into account.

4.5 Discussion

4.5.1 Comparison with previous studies

Our sample disks are largely identical to those adopted by Zhang et al. (2018) and Lodato et al. (2019), and thus we compare the results to see the agreement. Zhang et al. (2018) carried out gas-dust two-fluid hydrodynamical simulations and developed a more sophisticated method to derive the gas gap width by considering three different dust models (DSD1, '1mm', DSD2). Compared with their study, our study simply assumes that the gas gap width matches that of the dust gap due to strong gas-dust coupling, which is not necessarily valid if the coupling between dust and gas is weak. In principle, if the dust

grains are decoupled from the gas (Zhu et al., 2012; Weber et al., 2018), the dust gap should be wider than its associated gas gap. Therefore, the planetary masses predicted by the well-coupled DSD1 model of Zhang et al. (2018) are supposed to be comparable to ours, while those predicted by the less-coupled DSD2 model should be smaller.

At $\alpha = 10^{-3}$, the majority of the predictions given by DSD1 model from Zhang et al. (2018) are similar to ours within a factor of two (it is the same level of the uncertainly that we used), such as first planet of Elias 24 (45%), Elias 27 (31%) and GW Lup (21%). However, Zhang et al. (2018) gave significant larger predictions than ours for the inner or wide gaps: for instance, the predicted masses of the innermost gaps in HD 143006 and SR 4 differ by nearly a factor of five, and even the masses given by the 'DSD2' model are larger than ours. This discrepancy may be attributed to the difference in measurement of the gap width and computation time between Kanagawa et al. (2016) and Zhang et al. (2018). The predictions of Zhang et al. (2018) are based on fitting of gaps at 1000 planetary orbits, while the result of Kanagawa et al. (2016) is based on stationary shape of gaps in long-term simulations. Also the computational time required to reach the stationary shape is longer for a wider gap (see Figure 14 of Kanagawa et al. (2017)). If the gap width does not reach the stationary value within 1000 orbits, Zhang et al. (2018) may give a larger planet mass as compared with our predictions. In the case of the innermost gap of HD 143006, the stellar age ($\sim 4\,\mathrm{Myr}$) corresponds to $\sim 55\,000$ orbits at the location of the innermost gap ($21\,\mathrm{au}$), and hence the simulation time could be insufficient for the gap to reach its stationary width.

We also compare our results with those of Lodato et al. (2019). When a gap is classified as dust-only gaps (group I), we adopt the same Hill radius scaling relation as Lodato et al. (2019), and thus our predicted planetary mass for group I gaps most agree with those from Lodato et al. (2019) within 50% uncertainty level, such as RY Tau (35%) and the second planet of GO Tau (48%). This deviation is mainly due to the different stellar masses and gap widths adopted. Nevertheless, the planetary mass predicted from group II gaps in our study is significantly smaller than that in their study. For example, Lodato et al. (2019) predicted mass of the first gap of CI Tau to be $15.7\,\mathrm{M_J}$, while the same planet is predicted to be $0.85\,\mathrm{M_J}$ in our fiducial case with $\alpha = 10^{-3}$. Apart from the different gap width data we adopted, it is because $M_{\mathrm{p,gas}}$ given by equation (4.5) scales with Δ_{gap}^2, while $M_{\mathrm{p,dust}}$ based on the Hill radius relation scales with Δ_{gap}^3. Physically, it means that in the gas gap regime the dominant planet-gas interaction can create a wider gap than that expected by the Hill radius argument. Therefore, the planetary mass in this regime may be overestimated if equation (4.6) is used. It should be noted that in most cases, the width of the gas gap given by equation (4.5) is wider than that of the dust gap predicted by equation (4.6).

We would like to point out that theoretically, it is possible that the dust gap is wider than the gas gap; the dust gap width, Δ_{gap} in equation (4.6), is independent of the gas parameters, while the gas gap width, Δ_{gap} in equation (4.5), is scaled with viscosity as $\alpha^{-1/4}$, and with scale height as $(h/R)^{-3/4}$. Therefore, for a given planetary mass $M_p > M_{\mathrm{iso}}$, it is always possible to find a set of gas disk parameters (i.e. large enough α, h/R) with which the dust gap width by equation (4.6) is wider than that of the gas gap by equation (4.5). In such cases, $M_{\mathrm{p,dust}}$ is larger than M_{iso}, but the edge of the dust gap may be apart from the gas pressure bump. Thus it might be appropriate to still use equation (4.6) to estimate the planet mass.

Having said so, however, the parameter ranges for such cases (roughly $\alpha > 0.01$ and $h/R > 0.1$) are fairly different from those commonly adopted by previous studies. Moreover, the dust grains have to be decoupled from the gas; if the dust is strongly coupled to the gas, the width of the dust gap should well match that of the gas gap. In this case, the dust gap width expected by equation (4.6) is an overestimate. In the intermediate regime between the strongly-coupled and the decoupled cases, the dust gap width roughly agrees with the gas gap width, and equation (4.5) is still a good approximation in the gas gap regime.

4.5.2 Implications on planetary formation

Our classification of the observed gaps has shown gaps at inner region of the disk are mostly gas gaps (group II), while those at the outer region are mostly dust gaps (group I). The cores at the inner region of the disk undergo faster accretion due to high surface densities of both pebbles and gas, so they more likely become gas giants that can open wider gas gaps. On the other hand, planets at outer region of the disk undergo slow accretion because of insufficient material, and runaway gas accretion is also harder to be triggered because the larger aspect ratio leads to larger pebble isolation mass. In effect, it is harder for planets to open gaps in both gas and dust profiles at the outer region.

The abundance of dust gaps at the outer region also implies that the outer planets are in fact small in general, suggesting these distant planets are not those formed via gravitational instability, which should be much more massive and open gas gaps instead (Mayer et al., 2002). However, it remains unclear that how the cores of the outer planets form at such a large distance to the star, since the formation of the solid cores via collision at the outer region is very inefficient due to low density and temperature. It is also possible that cores are not formed *in situ*: they may form at the inner dust-rich region first, then migrate outwards and inward again after growing up (e.g. Paardekooper & Mellema, 2006; Paardekooper et al., 2011).

The configurations of the multi-planetary systems shown by Figure 4.6 suggest in general the planetary mass decreases with the radius. In a single-planetary systems, the planet can migrate freely inward and grow quickly at the inner region. In multi-planetary systems, if a gas giant is formed first at the interior, the strong 2:1 orbital resonance will prevent the outer planet from migrating further inwards, therefore in this case the inner planet always grows faster than the outer planets and the mass order is retained.

However, there are four disks out of this trend, namely DL Tau, HD 163296, HL Tau and V1094 SCO. For these four disks, it is possible that the outer planet is initially larger than the inner planet. As a result, it migrates to the current position and starts gas accretion earlier, which shields the inner planets from accessing accretion materials and therefore quenches its growth (also see Wang et al. (2020)). Therefore, the fate of an individual planet strongly depends on its birth place and time relative to other planets. While investigating the evolution of a multi-planetary system, it is important to consider the coupling between planets, as the planet-planet interaction can effectively shape the orbital and mass configuration.

We also found that in half of our sample disks, the outermost gas-gap is accompanied with a dust-gap planet close to its outer 2:1 mean motion resonance. The resonant trap

is one of the possible explanations: the dust-gap planet migrates inwards faster via type I migration, while the migration speed of the inner gas-gap planet is slower due to the gap-opening effect (Kanagawa et al., 2018). Once the outer planet approaches the inner planet, it will be captured due to resonance and start co-migration (e.g. Mustill & Wyatt, 2011; Deck & Batygin, 2015). An alternative explanation is that the density of large pebbles or planetesimals may be enriched at the resonance sites (e.g. Wyatt, 2003), therefore a planet is preferred to form near the resonance. Further investigations are required to discuss the possibilities of the respective scenario.

Finally, the evolution tracks on Figure 4.5 do not pass through the region of the observed hot Jupiters. This implies that those gas-gap opening planets in our predicted population are unlikely to be the origin of the hot Jupiters, at least before the dispersal of the disk. It is still possible for low mass planets to become hot Jupiters, but it depends on whether there exist a inner gas giant in the disk that can stop the inward migration of low mass planet via resonance capture. Alternatively, if the configuration of the planetary system is dynamically unstable, hot Jupiters can be formed via later stage scattering followed by tidal circularization (e.g. Nagasawa et al., 2008). Therefore, the stability of the planetary systems is crucially important to determine the final configurations, and that will be covered in the next chapter.

4.6 Summary

The scaling relations found by previous studies can be used to deduce the planetary mass from the shape of the gap. In order to make appropriate predictions, it is necessary to know whether the gap exists in both the gas/dust profiles or only exist in the dust profile. In this chapter, we purpose a method of solving this degeneracy by considering the core accretion scenario of planetary formation. Since the pebble isolation mass is always associated with a deep gas gap, if the predicted planetary mass is larger than pebble isolation mass, it can be regarded as a gap in both gas/dust profiles. Otherwise, the gap is considered as only a dust gap. By translating these mass criteria to gap classification criteria using two mass scaling relations, we can classify the observed gaps into four groups, and then predict the planetary mass according to the grouping. Based on our analysis of 35 disks with 55 gaps, our main results are:

1. For our fiducial value of $\alpha(= 10^{-3})$, 21 out of 55 gaps are classified as dust-only gaps, 19 are gas gaps, and 15 remain indistinguishable (table 4.2). Our criteria can distinguish between dust-only and dust-gas gaps for the majority of the observed gaps (73%). The viscosity α can significantly change the interpretation of the gaps, as discussed in section 4.4.2. As α increases, the number of indistinguishable gaps also increases. We show a particular example of α dependence in Figure 4.7 and the predictions are summarized in table 4.3.

2. Distribution of gaps in multi-gap systems shows that inner gaps are mostly gas gaps, while the outer gaps are mostly dust-only gaps. The predicted planetary mass in general decreases with increasing orbital radius. As discussed in section 4.5.2,

this trend can be explained by the difference of the accretion rates and pebble isolation mass at inner and outer disk regions, and is consistent with the core accretion scenario.

3. The predicted planetary mass ranges from $1.6\,\mathrm{M}_\oplus$ to $4.8\,\mathrm{M}_\mathrm{J}$. The evolution tracks for single planets suggest our predicted planets have potential to be the origin of the widely separated giant planets, such as planets in HR 8799 and PDS 70 (Figure 4.5). We also found that observed hot Jupiters are not located on the evolution tracks associated with planets that we predict. As discussed in section 4.5.2, it may imply that the dynamical instability is required to form hot Jupiters. Alternatively, their origin is different from those gap opening planets observed in PPDs.

4. Closely outside of the 2:1 resonance line of the inner planet that opens gas gap, there often exist a small planet that opens only a dust gap (Figure 4.6). As discussed in section 4.5.2, it can be related to the resonance capture due to convergent migration. Alternatively, the orbital resonance may be causally related to the planetary core formation.

Our results suggest that the core accretion scenario is consistent with the the observed gap structure, and the planet-planet interaction in the multi-planetary systems plays an important role to shape their architecture. In the next chapter, we will focus on multi-planetary systems and carry out N-body simulations based on the initial conditions that we have obtained. Before the dispersal of the disk, we will implement both migration and accretion with different disk parameters. After the disk dispersal, we will continue integrating the systems with gravitational force to Gyr timescale to assess the dynamical stability of the configuration. Eventually we will compare our synthesized systems with the observed exoplanetary population and see to what extent we can connect the observed disks to the diversity of the observed exoplanets.

Chapter 5

Planetary systems predicted from multiple ALMA disks II: evolution and long-term orbital stability

5.1 Introduction

In Chapter 4 (hereafter Paper I), we present our criteria to break the degeneracy of the dust-only gaps and the gas gaps, and give the mass predictions of the embedded planets based on the gap classifications that are consistent with the core accretion scenario. Upon comparison of the predicted planetary population with the observed exoplanetary population, we found that the two populations have little overlap in mass and semi-major axis distribution. Though this discrepancy may partially originate from the observation bias, the most important factor to consider here is that the planets embedded in the PPDs may significantly interact with the disk via orbital migration and mass accretion, as we show in Chapter 3.

Since the PPDs are generally young and expected to survive for a few millions of years before the dispersal, the current planetary architecture deduced from the disk substructure may be strongly shaped by the disk in terms of both semi-major axis and mass. Furthermore, even after the disk dispersal, the planetary system continues evolving via mutual gravity, and stochastic perturbations may also exist if there are planetesimals remaining. Therefore, in order to predict the final architecture of the planetary systems, it is crucial to quantitatively understand how the planets evolve with the disk, and whether the configurations are stable against the mutual gravity as well as the perturbation after the disk dispersal.

The main purpose of the this chapter (Paper II) is to follow the evolution of the 12 embedded multi-planetary systems starting from the observational motivated initial conditions, predict their evolution outcomes, and compare with the architecture of the observed exoplanetary systems. This approach has been attempted earlier for the HL Tau

This chapter is mainly based on the modified version of the manuscript Wang et al. (2021b) that was submitted to the Astrophysical Journal.

system in Chapter 3 (hereafter W20), in which its prominent three gaps have been assumed to be carved by three protoplanets with masses exceeding the pebble isolation mass. W20 found that the resulting planetary systems are basically stable over 10 Gyrs, and the planetary systems resemble several widely-separated giant planets observed by direct imaging such as HR 8799, β Pictoris and PDS 70. In this chapter, we extend W20 to the 12 ALMA disks with the multiple-gap substructure, which allows us to interpret the result of W20 in a more general context, not particular to the specific case of the HL Tau.

The rest of the chapter is organized as follows. Section 5.2 provides an overview of our investigation and summarises the results of Paper I that the masses and locations of the possible protoplanets embedded in the 12 ALMA disks, which serve as the initial conditions for the simulations in the present chapter. Section 5.3 describes our disk-planet interaction model including the pebble and gas accretion and orbital migration The results of simulations at the end of the disk-planet interaction stage are presented in section 5.4, and are employed as the initial conditions for the purely N-body simulations after the disk dispersal performed in section 5.5. In particular, we include the stochastic perturbative force due to residual planetesimals so as to examine the fate of few-body protoplanetary systems in a more realistic manner. The stability of such systems is presented in section 5.6, and section 5.7 discusses the validity, consistency and implications of the results. Finally section 5.8 is devoted to the summary and conclusion of the chapter.

5.2 Simulation and initial conditions

5.2.1 Overview

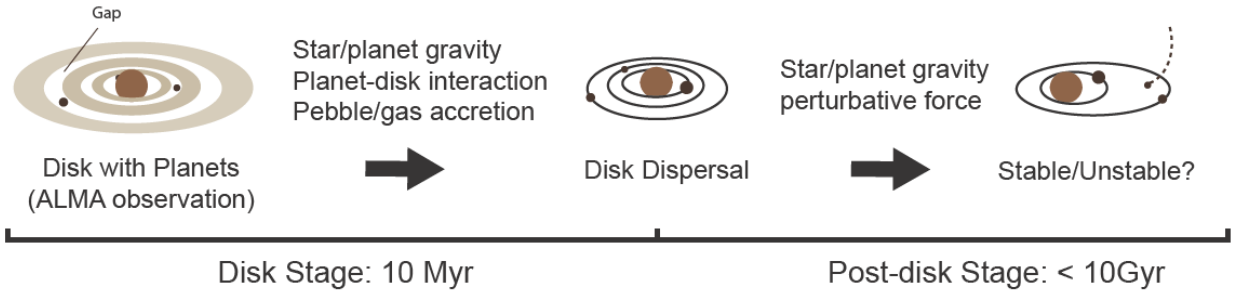

Figure 5.1: Schematic illustration of our simulation starting from the observed ALMA disks.

Figure 5.1 illustrates the overall picture of our simulation presented in this chapter. During the evolution of the primordial disk around a protostar, protoplanets form and open clear gap and ring structures in the dust disk as identified by ALMA. The locations and masses of those embedded planets are estimated in Paper I from the observed disk properties, as described in the next subsection. The initial conditions for our simulation are based on these predictions.

Similar to W20, our simulation consists of two different stages. First at the disk stage, we compute the evolution of the system by taking account of the mutual gravity among the central star and other planets, planet-disk interaction, and the resulting migration and mass accretion of each planet. The evolution model and the results are described in sections 5.3 and 5.4, respectively. After the gas component of the disk is dispersed, we switch to the second stage simulation, in which we consider the gravitational interaction among the star and planets, and neglect planet-disk interaction.

The above two-stage simulation method is basically the same as that adopted by W20, but with improvements in several aspects. Firstly, we predict the mass of the planet embedded in the observed gap using a more sophisticated method that considers the different gap-opening mechanisms in the gas and dust disks, as presented in Paper I. Secondly, we take account of the pebble accretion for planets below the pebble-isolation mass during the disk stage simulation. Finally, in the post-disk stage simulation, we introduce the stochastic perturbations due to numerous planetesimals around each planet, in addition to the mutual gravity among the star and other planets.

5.2.2 Initial condition for protoplanets embedded in the observed ALMA disk systems

In Paper I, we found that the mass of protoplanets embedded in the ALMA disks sensitively depends on the assumption whether or not the unobserved gas component has the similar gap structure as the dust component. The difference leads to fairly different predictions for the final outcome of the planetary systems. Therefore, we briefly summarize the main conclusion of Paper I here, and present how we assign initial conditions for the 12 ALMA disks that we consider in the present analysis.

The estimated planetary masses in Paper I are based on the observed gap substructures in PPDs reported by Long et al. (2018a), the Disk Substructures at High Angular Resolution Project (DSHARP) (Andrews et al., 2018), and van der Marel et al. (2019). In this chapter, we select all disks (twelve in total) that exhibit multiple-gaps in Paper I; out of the 12 disks, five disks have two gaps, six disks have three gaps, and the remaining one (HD 163296) has four gaps. The parameters for those disks are listed in Table 1 of Paper I.

We list the mass and outer radius of the disks in Table 5.1, which are relevant for determining the initial surface density in section 5.3.4. The outer radius of the disk is based on the disk radius at millimetre wavelength given by van der Marel et al. (2019) and Huang et al. (2018b). The total disk mass is also adopted from the the respective reference if provided, otherwise it is calculated from the $1300\,\mu\mathrm{m}$ flux using the relation provided in Cieza et al. (2008):

$$M_{\rm disk} = 1.7 \times 10^{-4}\,\mathrm{M}_\odot \left(\frac{F_{1300\mu\mathrm{m}}}{\mathrm{mJy}}\right)\left(\frac{d}{140\,\mathrm{pc}}\right)^2. \tag{5.1}$$

For the HL Tau disk, we adopt the disk mass estimated by Kwon et al. (2015), same as we adopted in W20.

Here we briefly show the method that Paper I proposed to predict planetary mass by classifying the gaps into three groups (there is no gap corresponding to Group IV in our selected ALMA disks). There are three characteristic mass scales relevant in the present analysis. If the planet is embedded in a dust gap alone in which the gas component does not open a significant gap, the corresponding planet is expected to have the mass (e.g., Lodato et al., 2019):

$$M_{\rm p,dust}(R_{\rm gap}) = 6.01 M_\oplus \left(\frac{M_*}{M_\odot}\right) \left(\frac{\Delta_{\rm gap}/R_{\rm gap}}{0.1}\right)^3, \tag{5.2}$$

where $R_{\rm gap}$ and $\Delta_{\rm gap}$ are the radius and width of the observed gap, and M_* is the mass of the central star. In contrast, if the gas component exhibits the same gap structure as observed for the dust component, the mass of such a planet is predicted and empirically given by Kanagawa et al. (2016) as

$$M_{\rm p,gas}(R_{\rm gap}) = 175 M_\oplus \left(\frac{M_*}{M_\odot}\right) \left(\frac{\Delta_{\rm gap}/R_{\rm gap}}{0.5}\right)^2 \left(\frac{h_{\rm gap}/R_{\rm gap}}{0.05}\right)^{3/2} \left(\frac{\alpha}{10^{-3}}\right)^{1/2}, \tag{5.3}$$

where α is the assumed disk viscosity.We follow Dong et al. (2018b) and estimate the gas scale height $h_{\rm gap}$ at $R_{\rm gap}$ the stellar temperature model, assuming a locally isothermal disk and ideal gas equation of state (see section 2, Paper I). Adopting this model results in a vertically flared disk with the flaring index equal to 0.25

$$\frac{h}{R} = \left(\frac{h}{R}\right)_{100\,\rm au} \left(\frac{R}{100\,\rm au}\right)^{0.25}. \tag{5.4}$$

The important scale that distinguishes between the above two cases is the pebble isolation mass $M_{\rm iso}$. When a planet becomes more massive than $M_{\rm iso}$, it starts to open a shallow gas gap that generates a pressure maxima at its vicinity. Thus the pebble accretion is terminated, and instead, run-away gas accretion onto the planet is triggered by the cooling. The planet grows quickly in mass to open a deep gap in both the gas and dust disks. Therefore, $M_{\rm p,dust} < M_{\rm iso}$ and $M_{\rm p,gas} > M_{\rm iso}$ should essentially correspond to the conditions for the dust-only gaps and both dust and gas gaps, respectively.

We adopt a fitting formula by Bitsch et al. (2018) for the pebble isolation mass at R:

$$M_{\rm iso}(R) = 25 M_\oplus \left(\frac{M_*}{M_\odot}\right) \left(\frac{h/R}{0.05}\right)^3 f(\alpha,\eta), \tag{5.5}$$

$$\tag{5.6}$$

where

$$f(\alpha,\eta) = \left[0.34\left(\frac{-3.0}{\log\alpha}\right)^4 + 0.66\right]\left(1 - \frac{\eta+2.5}{6}\right), \tag{5.7}$$

with $\eta = \partial \ln P/\partial \ln R$ being the logarithmic pressure gradient.

In reality, however, the values of $M_{\rm p,dust}$, $M_{\rm p,gas}$ and $M_{\rm iso}$ suffer from fairly large theoretical and observational uncertainties. Therefore, in Paper I we allow a fudge factor of two for the estimated masses, and classify the observed ALMA gaps into the three groups:

	$M_{p,dust} < M_{iso}$	$M_{iso} < M_{p,dust} < 2M_{iso}$	$M_{p,dust} > 2M_{iso}$
$M_{p,gas} < 1/2M_{iso}$	$M_{p,dust}$(D)	M_{iso}(P)	None
$1/2M_{iso} < M_{p,gas} < M_{iso}$	$M_{p,dust}$(D), M_{iso}(P)	M_{iso}(P)	M_{iso}(P)
$M_{p,gas} > M_{iso}$	$M_{p,dust}$(D), $M_{p,gas}$(G)	M_{iso}(P), $M_{p,gas}$(G)	$M_{p,gas}$(G)

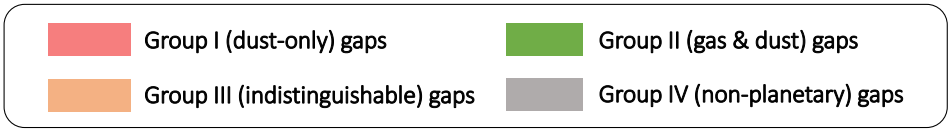

Figure 5.2: Criteria for the planetary mass assignment and gap classification. Groups I gaps only open in the dust disk; Group II gaps open in both the gas and dust disk; Group III gaps are indistinguishable gaps that can be interpreted as either dust-only gaps or gas gaps; Group IV gaps have non-planetary origin. No gap belongs to Group IV in our sample.

Group I (dust-only), Group II (gas & dust) and Group III (indistinguishable) gaps. The gap classification criteria are summarised in in Figure 5.2.

In this chapter, since our migration and accretion recipes are determined by whether the planetary mass is above or below $M_{\rm iso}$ without the fudge factor of two, we further refine the mass assignment of Paper I to make the evolution of the respective gap interpretation consistent with $M_{\rm iso}$. The respective criteria for the mass assignment are also summarised in Figure 5.2. For example, for Group I gaps, we adopt $M_{\rm p,dust}$ as the initial planetary mass only if $M_{\rm p,dust} < M_{\rm iso}$; otherwise, $M_{\rm iso}$ is adopted instead. Similar rule is also applied to Group II gaps, and for Group III gaps it is possible to have two possible initial mass assignments. For convenience, in this chapter, we use symbols D (dust), G (gas), and P (pebble-isolation mass) to indicate that the mass of the planet is set to be $M_{\rm p,dust}$, $M_{\rm p,gas}$, and $M_{\rm iso}$ at the initial epoch of our simulations. Note that here we do not consider Group IV (non-planetary origin) because no gap belongs to this group in Paper I.

Table 5.1 shows all sets of the initial planetary mass adopted when α is the fiducial value 10^{-3}. If one or more gaps in a disk system have two mass interpretations, we explore all the possible combinations of mass assignments. For example, both gap 2 and gap 3 in CI Tau are Group III gaps and have two mass assignments ('PG' and 'DP'), therefore there are in total four combinations ('GPD','GPP','GGD','GGP') for CI Tau. The adopted α can change both the classification of the gaps and the predicted planetary masses, especially when the predicted planetary mass is close to the respective $M_{\rm iso}$.The planetary masses are estimated assuming each gap is opened by a single planet, and planets are located at the mid-points of the corresponding gaps. Note that the planetary masses adopted for HL Tau in Table 5.1 are about two times as large as those adopted in W20, mainly because of the different α values that we adopted ($\alpha = 10^{-3}$ in Table 5.1, but $\alpha < 6 \times 10^{-4}$

Disk(set)	$M_{\rm disk}$	$R_{\rm out}$	Planet 1 Location(au)		Planet 2 Location(au)		Planet 3 Location(au)		Planet 4 Location(au)	
	($M_\odot$)	(au)	Type	Mass($M_{\rm J}$)	Type	Mass($M_{\rm J}$)	Type	Mass($M_{\rm J}$)	Type	Mass($M_{\rm J}$)
AA TAU	0.0162	150		72		118				
AA TAU(DD)			D	0.090	D	0.031				
AA TAU(PD)			P	0.175	D	0.031				
AS 209	0.0366	139		8.7		61		93		
AS 209(GPD)			G	0.434	P	0.193	D	0.114		
AS 209(GPP)			G	0.434	P	0.193	P	0.265		
AS 209(GGD)			G	0.434	G	0.200	D	0.114		
AS 209(GGP)			G	0.434	G	0.200	P	0.265		
CI TAU	0.0308	174		14		48		119		
CI TAU(GPD)			G	0.656	P	0.127	D	0.108		
CI TAU(GPP)			G	0.656	P	0.127	P	0.250		
CI TAU(GGD)			G	0.656	G	0.132	D	0.108		
CI TAU(GGP)			G	0.656	G	0.132	P	0.250		
DL TAU	0.0374	147		39		67		89		
DL TAU(DPG)			D	0.091	P	0.142	G	0.271		
DL TAU(PPG)			P	0.095	P	0.142	G	0.271		
DoAr 25	0.0406	165		98		125				
DoAr 25(DD)			D	0.071	D	0.009				
Elias 24	0.0506	150		55		94				
Elias 24(GD)			G	0.529	D	0.033				
GO TAU	0.0098	144		59		87				
GO TAU(GD)			G	0.262	D	0.043				
GY 91	0.0191	140		41		69		107		
GY 91(DDD)			D	0.143	D	0.011	D	0.008		
GY 91(PDD)			P	0.174	D	0.011	D	0.008		
HD 143006	0.0139	82		22		51				
HD 143006(GG)			G	2.977	G	0.264				
HD 163296	0.0633	169		10		48		86		145
HD 163296(GGDD)			G	0.320	G	0.995	D	0.254	D	0.030
HD 163296(GGPD)			G	0.320	G	0.995	P	0.406	D	0.030
HL TAU	0.105	80		12		32		82		
HL TAU(GPP)			G	1.618	P	0.221	P	0.445		
V1094 SCO	0.0401	290		60		103		174		
V1094 SCO(DGD)			D	0.070	G	0.365	D	0.023		
V1094 SCO(PGD)			P	0.138	G	0.365	D	0.023		

Notations for adopted planetary mass: G: $M_{\rm p,gas}$, P: $M_{\rm iso}$, D : $M_{\rm p,dust}$.
References. Huang et al. (2018b);Long et al. (2018a); van der Marel et al. (2019).

Table 5.1: Disk parameters and initial planetary mass at fiducial $\alpha = 10^{-3}$.

in W20). If adopting the same value of α, we obtain the similar masses as W20.

5.3 Evolution of protoplanets in a gas disk: orbital migration and mass accretion

At the disk stage indicated in Figure 5.1, the embedded protoplanets interact with the disk, in addition to the mutual gravitational interaction with the central star and other planets. While the detailed evolution needs to be studied with intensive hydrodynamical simulations, we decided to adopt an empirical parametrized model to describe the planet-disk interaction (W20). Specifically, we employ a cylindrical coordinate, and compute the

position vector of the i-th planet from

$$\ddot{\boldsymbol{R}}_i = \boldsymbol{f}_{\mathrm{grav,i}} + \boldsymbol{f}_{\mathrm{a,i}} + \boldsymbol{f}_{\mathrm{e,i}}, \tag{5.8}$$

where $\boldsymbol{f}_{\mathrm{grav,i}}$ is the gravity exerted by the central star and other planets, $\boldsymbol{f}_{\mathrm{a,i}}$ is the migration force, and $\boldsymbol{f}_{\mathrm{e,i}}$ is the eccentricity damping force, acting on the i-th particle per unit mass. The latter two forces represent the planet-disk interaction, and are discussed further in section 5.3.1.

We simultaneously compute the evolution of the planetary mass due to the accretion of pebbles and gas from the disk. We describe how we model these accretion processes in section 5.3.2, followed by the disk surface density model in section 5.3.3.

5.3.1 Planetary migration model

We adopt the same migration model as implemented in W20. Based on the hydrodynamical simulation results of Kanagawa et al. (2018), this model considers the gas depletion effect due to the gap opening and empirically parameterizes the planetary migration in terms of a dimensionless factor K_i that characterizes to the depth of the i-th gap

$$\frac{\Sigma_{\mathrm{min,i}}}{\Sigma_g(R_i)} = \frac{1}{1+0.04K_i}, \tag{5.9}$$

where Σ_{min} and Σ_g are the minimum gas surface density inside the gap and unperturbed surface density.

The factor K_i is written as (e.g. Kanagawa et al., 2016, 2018)

$$K_i = \left(\frac{M_i}{M_*}\right)^2 \left(\frac{h_i}{R_i}\right)^{-5} \alpha^{-1}, \tag{5.10}$$

where M_i is the time-dependent mass of the i-th planet, and h_i/R_i is the aspect ratio at its location.

Then the migration timescale of the i-th planet is empirically approximated as

$$\tau_{a,i} = \frac{1+0.04K_i}{\gamma_{L,i} + \gamma_{C,i}\exp(-K_i/K_t)} \tau_{0,i}(R_i), \tag{5.11}$$

where $\gamma_{C,i} = \Gamma_{C,i}/\Gamma_{0,i}$ and $\gamma_{L,i} = \Gamma_{L,i}/\Gamma_{0,i}$, with $\Gamma_{C,i}$, $\Gamma_{L,i}$, and $\Gamma_{0,i}$ being the co-rotation, Lindblad, and characteristic torques for the i-th planet (Paardekooper et al., 2010). Further details can be found in section 3.2 of W20.

5.3.2 Mass accretion onto planets

Pebble accretion and gas accretion are the two major channels for the mass growth of protoplanets. The standard core accretion theory states that a planet forms a rocky core via pebble accretion first (e.g., Ormel & Klahr, 2010). After the planetary mass

exceeds $M_{\rm iso}$, the run-away gas accretion process sets in. Since our present simulation considers the initial mass of planets ranging from $10^{-3}\,{\rm M_J}$ to $\sim$ a few $\rm M_J$, we take account of both pebble and gas accretion processes. On the other hand, the pebble accretion is not considered in W20, because W20 assume that the embedded planets in the HL Tau system have opened gas gaps with initial masses larger than $M_{\rm iso}$.

Pebble accretion

When a planet is small, its gravity is too weak to capture the gas, and therefore its mass grows mainly through the accretion of pebbles. We follow Lambrechts & Johansen (2012), and assume that the pebbles can accrete on the i-th planet only within the effective radius $r_{\rm acc,peb}$ from its location R_i:

$$r_{\rm acc,peb}(R_i) = \left(\frac{St}{0.1}\right)^{1/3} R_H(R_i), \tag{5.12}$$

where $R_H(R_i)$ is the Hill radius of the planet at R_i and St is the Stokes number of the pebbles. Also we assume a non-stratified disk with the turbulent diffusivity comparable to the turbulent (kinematic) viscosity. In this case, the pebble scale height $h_{\rm peb}$ is approximately written in terms of the gas scale height h (Youdin & Lithwick, 2007) as

$$h_{\rm peb}(R_i) = \sqrt{\frac{\alpha}{St}} h(R_i). \tag{5.13}$$

If $r_{\rm acc,peb} > h_{\rm peb}$ ($r_{\rm acc,peb} < h_{\rm peb}$), the accretion effectively proceeds in two (three) dimensions. Thus we adopt the following mass growth rate (e.g. Lambrechts & Johansen, 2012; Ormel, 2017; Johansen et al., 2019):

$$\dot{M}_{\rm peb,i} = \begin{cases} 2\Omega_{k,i}[r_{\rm acc,peb}(R_i)]^2 \Sigma_{\rm peb}(R_i) & \text{for } r_{\rm acc,peb}(R_i) > h_{\rm peb}(R_i) \\ 6\pi\Omega_{k,i}[r_{\rm acc,peb}(R_i)]^3 \rho_{\rm peb}(R_i) & \text{for } r_{\rm acc,peb}(R_i) < h_{\rm peb}(R_i) \end{cases} \tag{5.14}$$

where $\Omega_{k,i}$, $\Sigma_{\rm peb}(R_i)$ and $\rho_{\rm peb}(R_i)$ are the Keplerian angular velocity, pebble surface density and mid-plane pebble density at R_i, respectively. The mid-plane pebble density $\rho_{\rm peb}(R_i)$ is computed from the pebble surface density $\Sigma_{\rm peb}(R_i)$ using the relation $\rho_{\rm peb}(R_i) = \Sigma_{\rm peb}(R_i)/(\sqrt{2\pi} h_{\rm peb}(R_i))$.

We note that the above two expressions are discontinuous at $r_{\rm acc,peb}(R_i) = h_{\rm peb}(R_i)$ because they correspond to the respective asymptotic limits of 2D and 3D pebble accretion regimes, strictly speaking. An interpolation between the two may be adopted to describe the transition of accretion regimes, but it does not change the results in practice. Therefore, we adopt these discontinuous expressions of equation (5.14), same as the original expression in the previous literature (e.g., Ormel, 2017).

The pebble accretion process continues until the planetary mass exceeds the pebble isolation mass $M_{\rm iso}$, at which the planet is massive enough to generate a pressure bump that prevents the pebbles from approaching the planet by effectively trapping them. Therefore, after the outer planet reaches its pebble isolation mass, the pebble flux onto the inner planet is also inhibited due to the presence of the pressure bump. This pebble

shielding effect is incorporated by setting $\dot{M}_{\rm peb} = 0$ in the region interior to the planet that reaches pebble-isolation mass, and we turn off the pebble accretion of the inner planets.

Gas accretion

When the planetary mass exceeds $M_{\rm iso}$, the planet grows only via gas accretion. Tanigawa & Tanaka (2016) investigated the gas accretion from the disk and found out the accretion occurs effectively at certain places around two Hill radii from the planet. Their model expresses the accretion rate as the product of the accretion area per unit time D and the surface density around the planet (approximately the minimum surface density inside the gap $\Sigma_{\rm min}$):

$$\dot{M}_{\rm gas,i} = D_i \Sigma_{{\rm min},i}, \tag{5.15}$$

where $\Sigma_{{\rm min},i}$ is given by equation (5.9) in terms of the gas surface density profile $\Sigma_g(R_i)$, and

$$D_i = 0.29 \left(\frac{h_i}{R_i}\right)^{-2} \left(\frac{M_i}{M_*}\right)^{4/3} R_i^2 \Omega_{K,i}, \tag{5.16}$$

with M_i being the mass of the i-th planet.

5.3.3 Gas and pebble surface density profiles in the disk

Gas surface density profile

We adopt the same model of gas surface density profile hosting multiple planets as W20. For a quasi-steady gas disk with the star and each planet taking in mass and angular momentum via gas accretion, the gas surface density $\Sigma_g(R)$ between the nth and $(n+1)$th planets is given by

$$\Sigma_g(R) = \frac{\dot{M}_{\rm gas,*}}{3\pi\nu(R)} \left(1 - \sqrt{\frac{R_*}{R}}\right) + \sum_{i=1}^{n} \frac{\dot{M}_{\rm gas,i}}{3\pi\nu(R)} \left(1 - \sqrt{\frac{R_i}{R}}\right) \tag{5.17}$$

where $R_n \leq R < R_{n+1}$, $\dot{M}_{\rm gas,*}$ and $\dot{M}_{\rm gas,i}$ are the gas accretion rates of the star and the i-th planet, $\nu(R) \equiv \alpha c_s(R) h(R)$ is the kinematic viscosity with c_s being the sound speed. The stellar accretion rate $\dot{M}_{\rm gas,*}$ is the remaining gas flux after the global gas influx $\dot{M}_{\rm glob}$ is consumed due to the gas accretion of all relevant planets:

$$\dot{M}_{\rm gas,*} \equiv \dot{M}_{\rm glob} - \sum_{i=1}^{N} \dot{M}_{\rm gas,i}. \tag{5.18}$$

If the mass of the i-th planet is below $M_{\rm iso}$ and undergoes pebble accretion, we set $\dot{M}_{\rm gas,i} = 0$. The mass and location of all the planets determine how the global gas influx $\dot{M}_{\rm glob}$ is distributed among planets and stars: strong gas accretion of the outer planet consumes

a large fraction of the $\dot{M}_{\rm glob}$ and thus lower the surface density at the inner region, effectively quenching both migration and mass growth of the inner planet. Such an effect is important and will be further discussed in section 5.4.2.

To account for the decay of the disk due to both photoevaporation and accretion, we set the the global accretion rate exponentially decay with the e-folding gas dispersal timescale of $\tau_{\rm disk}$:

$$\dot{M}_{\rm glob}(t) = \dot{M}^{\rm ini}_{\rm glob} e^{-t/\tau_{\rm disk}}, \tag{5.19}$$

with $\tau_{\rm disk}$ fixed throughout each realization. As will be shown in section 5.3.4, $\dot{M}^{\rm ini}_{\rm glob}$ is determined by the observed disk size and mass given in table 5.1. Thus, when R is sufficiently larger than the radius of the outermost planet, the surface density profile $\Sigma_g(R) \simeq \dot{M}_{\rm glob}/(3\pi\nu)$ is reduced to the unperturbed disk profile given by e.g., Pringle (1981).

Pebble surface density profile

The pebble surface density $\Sigma_{\rm peb}$ at the location of the i-th planet is given from the flux of the pebbles as

$$\Sigma_{\rm peb,i} = \frac{\dot{M}_{\rm peb,glob}}{2\pi R\,|v_{{\rm drift},i}|}, \tag{5.20}$$

where $\dot{M}_{\rm peb,glob}$ is the global pebble accretion rate and $v_{{\rm drift},i}$ is the pebble drifting speed. Unlike the gas profile, we neglect the feedback of pebble accretion of an individual planet on the global pebble profile. We further assume that $\dot{M}_{\rm peb,glob}$ is proportional to $\dot{M}_{\rm glob}$:

$$\dot{M}_{\rm peb,glob} = \chi \dot{M}_{\rm glob}(t), \tag{5.21}$$

where the proportional constant χ is set to the global pebble to gas ratio (we adopt $\chi = 0.01$).

The pebble-drifting speed $v_{{\rm drift},i}$ can be expressed in terms of the Stokes number (Weidenschilling, 1977):

$$v_{\rm drift,i} = -\frac{2\Delta v_{{\rm sub},i}}{St + St^{-1}} + \frac{u_{R,i}}{1+St^2}, \tag{5.22}$$

where $\Delta v_{\rm sub}$ is the relative velocity between pebbles and sub-Keplerian gas, u_R is the radial drifting speed of the gas, which are given respectively by (e.g. Birnstiel et al., 2012; Ormel, 2017; Johansen et al., 2019)

$$\Delta v_{{\rm sub},i} = -\frac{1}{2}\frac{h_i^2}{R_i}\frac{\partial \ln P_i}{\partial \ln R_i}\Omega_{K,i} \tag{5.23}$$

$$u_{R,i} = -\frac{3}{2}\alpha\frac{h_i^2}{R_i}\Omega_{K,i}. \tag{5.24}$$

Equation (5.22) suggests that pebble drifting speed strongly depends on the Stokes number, i.e., the aerodynamical property of the pebbles. Ormel (2017) pointed out that $St \sim 10^{-3} - 10^{-1}$ is the optimal range for efficient pebble accretion, since pebbles with very small $St(< 10^{-5})$ or $St \sim 1$ are difficult to be accreted onto the planet: aerodynamically small pebbles well couple with the gas and thus hard to settle to the planet, while

Notation	Meaning	Value*
α	Viscosity	$5 \times 10^{-4}, \underline{10^{-3}}, 2 \times 10^{-3}$
$\tau_{\rm disk}$	Disk decay lifetime	$\underline{2\,\mathrm{Myr}}, 3\,\mathrm{Myr}$
f	Flaring index	0.25
St	Stokes Number	0.01
χ	Pebble-to-gas ratio	0.01

*the underscored is the fiducial value

Table 5.2: Summary of the disk parameters

pebbles with $St \sim 1$ is hard to be captured due to its fast drifting speed. For simplicity, we adopt a constant St in each simulation run and set the fiducial St value to be 10^{-2}.

5.3.4 Numerical simulations and disk parameters

Our simulations are performed using the public n-body code `rebound` (Rein, 2012) and its extension `reboundx` (Tamayo et al., 2020). As already introduced in section 5.2.1, our simulation consists of two stages: the disk stage and post-disk stage. At the disk stage, the `ias15` integrator (Rein & Spiegel, 2014) is used, and the planetary migration is computed taking account of both planet-disk interaction and mass accretion (see sections 5.3.1 and 5.3.2).

We list all the disk parameters that are fixed constant throughout each simulation in Table 5.2. To be consistent with the temperature model that we adopted for the mass prediction, the flaring index is fixed to 0.25 (equation 5.4). The Stokes number St and pebble-to-gas ratio χ are only relevant to the pebble accretion. We found the architecture were not sensitive to both St and χ since the migration strongly outperforms the pebble accretion when the planetary mass is small, and thus we fix these two parameters and focus on the impact of others. For each ALMA disk system, we have surveyed different initial mass assignments, α viscosities and disk lifetime. The planets are initialised with co-planar and nearly-circular orbits with the initial eccentricity of 10^{-7}. We stop the simulation at $5\tau_{\rm disk}$ to ensure that the disk has sufficiently dispersed.

We adopt a constant α model that is independent of time and position. The initial value of $\dot{M}_{\rm glob}$ is normalised by the total disk mass:

$$\dot{M}^{\rm ini}_{\rm glob} = \frac{3}{2}\nu_{\rm 1au}\left(\frac{M^{\rm ini}_{\rm disk}}{1\,\mathrm{au}^2}\right)\left[\left(\frac{R_{\rm out}}{1\,\mathrm{au}}\right) - \left(\frac{R_{\rm in}}{1\,\mathrm{au}}\right)\right]^{-1}, \tag{5.25}$$

where $M^{\rm ini}_{\rm disk}$ is the initial disk mass, $\nu_{\rm 1au} = \nu(R = 1\,\mathrm{au})$ is the kinematic viscosity at $1\,\mathrm{au}$.

We assume the outer edge of the dust disk is the same as that of the gas disk. The inner edge of the disk is often poorly resolved, so we simply set the inner edge to be $0\,\mathrm{au}$, except for AA Tau, whose inner edge is set to be the outer boundary of its inner cavity.

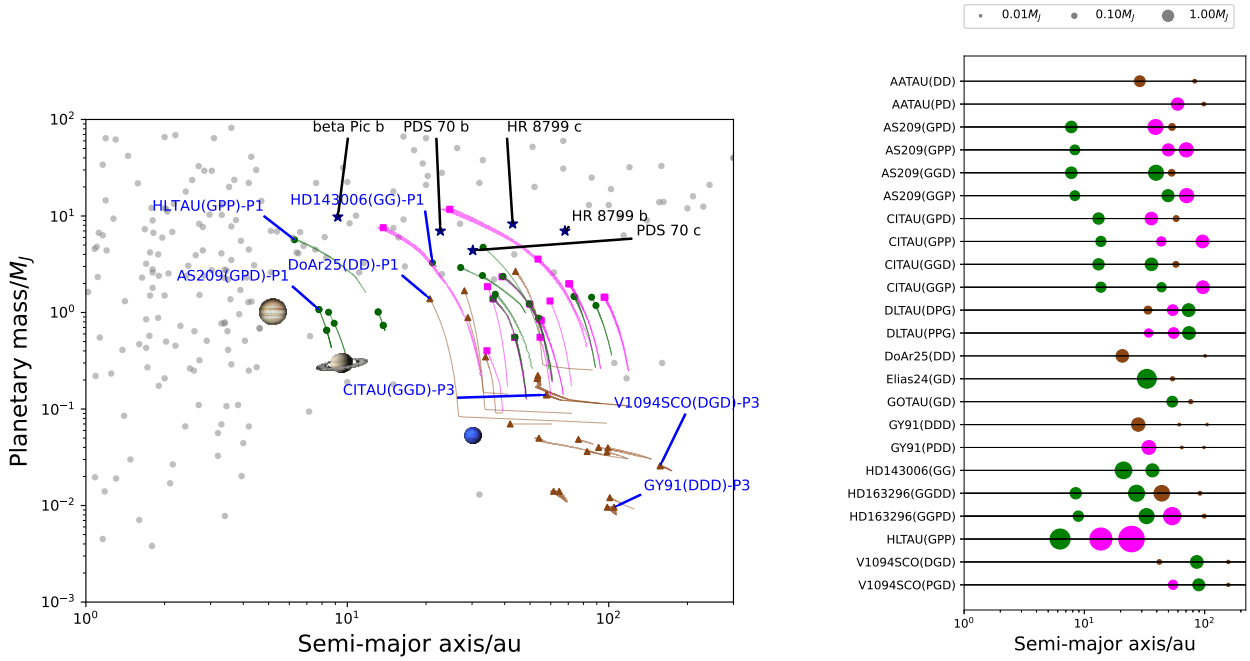

(a) (b)

Figure 5.3: (a) Final mass and semi-major axis of the simulated planetary systems evolved with fiducial $\alpha = 10^{-3}$, as well as the observed exoplanetary population in grey dots (data extracted from `exoplanet.eu`, 2021). Green, magenta, and brown color denote $M_{\rm gas}$, $M_{\rm iso}$, $M_{\rm dust}$ adopted as initial planetary mass. The blue text tags some example planets. The respective color lines show the evolution track. Jupiter, Saturn, Uranus (cyan) and Neptune (dark blue) are also plotted. (b) Configuration of planetary systems at the end of disk dispersal at $\alpha = 10^{-3}$. The marker size is proportional to $M_{\rm p}^{2/3}$. The different colours denote the interpretation of the initial planetary mass assigned: brown indicates $M_{\rm p,dust}$, magenta indicates $M_{\rm iso}$ and green indicates $M_{\rm p,gas}$.

5.4 Architecture of planetary systems at the end of the disk stage

In this section, we compute the evolution of planetary systems through the disk-planet interaction, and present their architecture at the end of the disk stage. The majority of planets has significantly migrated inwards and/or increased the mass, and their final architecture varies much when a different set of initial conditions and disk parameters are employed. In the following subsections, we will compare the resulting configurations of the planetary systems against the observation, by emphasizing the dependence on the disk parameters and initial planetary mass assignments.

5.4.1 Overall results at the disk stage

Figure 5.3 shows the evolution of mass and semi-major axis of the planetary systems at the disk stage for the fiducial disk parameters listed in Table 5.2. In Figure 5.3(a), solid

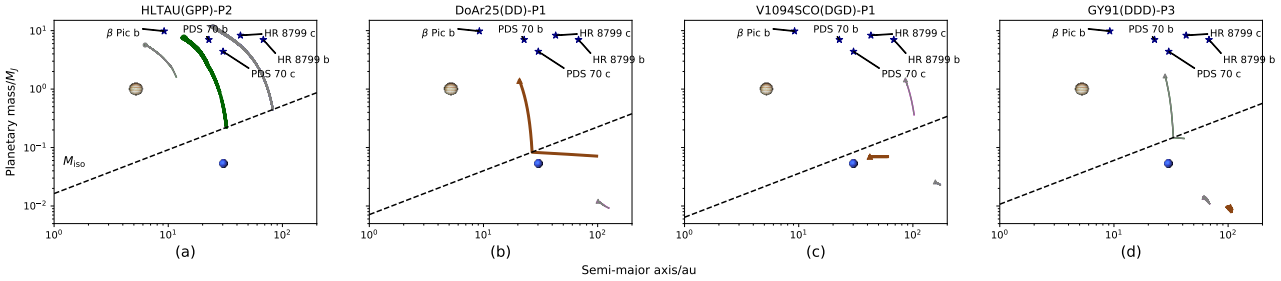

Figure 5.4: Example evolution of planets from four different groups. Evolution of other planets in the same system are also plotted in grey colour.

symbols indicate the positions and masses of the simulated planets at the end of the disk stage; different colours correspond to the type of initial planetary mass (G: green circles, P: magenta squares, and D: brown triangles), and lines associated with each symbol are evolution tracks of the planets. For reference, the locations of the observed planets are plotted in grey dots, as well as those of Jupiter, Saturn and Neptune in the Solar system. Figure 5.3(b) shows the final mass and semi-major axis of planets for each system.

While most of the planets are initially located far away from the observed population, during the disk-stage evolution the planets migrate inwards and grow larger. Although the majority of the resulting systems do not cover the range of observed planets, a fraction of them turn out to be very close to the systems observed via direct imaging, such as β Pic b, PDS 70b, PDS 70c, HR 8799b, and HR 8799c. Those planets that are initialised with mass equal or larger than $M_{\rm iso}$ (magenta and green) undergo gas accretion throughout the simulation, and their evolution tracks are well-consistent with the predictions of Tanaka et al. (2020) (See figure 4 of Paper I).

We divide the simulated planets roughly in four different groups whose typical evolution tracks are plotted in Figure 5.4. Although the planetary systems contain multiple planets, the initial mass and location are still the most important factors for the disk stage evolution as well as the final configuration, rather than the presence of other planets. Hence, we simply highlight the planet corresponding to the respective category, while the rest of planets in the same system are plotted in grey colour just for reference. In the following, we briefly summarise the feature of planets in each category.

1. **Distant giant planets (Figure 5.4a):** a fraction of our simulated planets including HL Tau(GPP), HD 143006(GG), and Elias 24 Planet 1(G) end up with $0.5-3$ Jupiter-mass planets or even more massive brown dwarfs with semi-major axis between $30\,{\rm au}$ and $100\,{\rm au}$. Most of these planets start with gas accretion and fail to move to the inner region due to the slow migration. The most massive ones resemble those widely-separated systems discovered via direct imaging, HR 8799, β Pictoris and PDS 70 systems.

2. **Jupiter-like planets (Figure 5.4b):** around 10 planets have final masses around $1-2$ Jupiter masses with semi-major axis less than $30\,{\rm au}$. A few of them are initially far away ($>50\,{\rm au}$) with mass slightly below $M_{\rm iso}$, e.g., AA Tau Planet 1(D), DoAr 25 Planet 1(D), GY 91 Planet 1(D). These planets first migrate significantly via the fast Type I migration, followed by the run-away gas accretion at the inner region of the disk, as illustrated by the L-shape brown tracks in Figure 5.3(a). The rest of

the planets (e.g., AS 209 Planet 1(G), HD 163296 Planet 1(G)) are initially around $10\,\mathrm{au}$, which are close to the orbits of Jupiter and Saturn. Due to their large initial mass, they never experience strong migration nor accretion in the later stage.

3. **Neptune-like planets (Figure 5.4c):** several planets (e.g. CI Tau Planet 3(D)) do not enter or barely enter the run-away gas accretion phase due to the combination of surface density drop and resonance block from the inner gas planet; they migrate very slowly without significant mass growth and stay at the region around $50\,\mathrm{au}$. V1094 SCO Planet 1(D) is close to Neptune in terms of both mass and semi-major axis.

4. **Distant small planets (Figure 5.4d):** some low mass planets with a few $\mathrm{M}_\oplus$ (e.g. GY 91 Planet 3(D)) on the lower right area in Figure 5.3(a) are too small and far away, so they do not evolve and stay at their initial locations without changing the mass.

Incidentally, our simulated systems turned out not to reproduce the observed population of Hot Jupiters. This conclusion is different from the previous claim by Lodato et al. (2019), who consider only the migration of the planets without accretion. Indeed, the inward migration of the gas giants is significantly slowed down once the planets enter the run-away gas accretion phase, because the fast growing planetary mass quickly depletes the gas gap. This effect has been pointed out by Tanaka et al. (2020) in the context of a single, isolated planet, and our simulation confirms that this is also valid for multi-planet systems. Moreover, in a multi-planetary system, once the inner planet becomes a gas giant, it blocks the outer planet from migrating further inward via resonance. In order to become a Hot Jupiter eventually, the embedded protoplanet should be less massive and locate closer to the central star, so as to experience the fast Type I migration to reach inner region followed by the substantial gas accretion. This problem may point to several possibilities including the observational bias and limitations of the current ALMA disks and/or the additional perturbations from nearby objects, which will be discussed in section 5.7.3.

5.4.2 Dependence on the different mass assignment for the embedded planets

We have shown in the previous subsection that the initial planetary mass significantly affects the subsequent evolution, and thus the final configuration of the system. To illustrate this dependence on the initial mass, we select example systems with two planets (AA Tau), three planets (CI Tau), and four planets (HD 163296). In each disk system, we explore two different mass assignments for one of the planets, considering theoretical and observational uncertainties of a mass estimate, as mentioned in Section 5.2.2. Other initial conditions, such as locations of planets and disk parameters, are kept identical. Here we focus on how the difference of the initial mass assignments affects the evolution of planetary systems.

Our results show that initial planetary mass assignments lead to different evolution outcomes, although the level of deviations depends on the individual setup. As shown

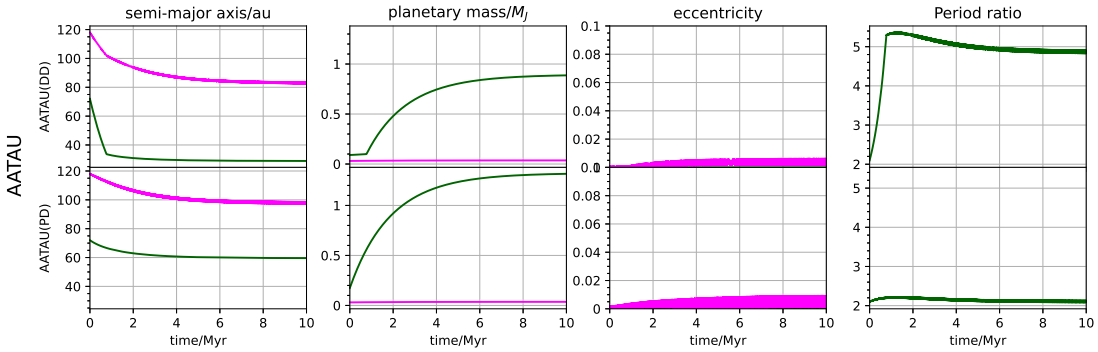

(a) AA TAU

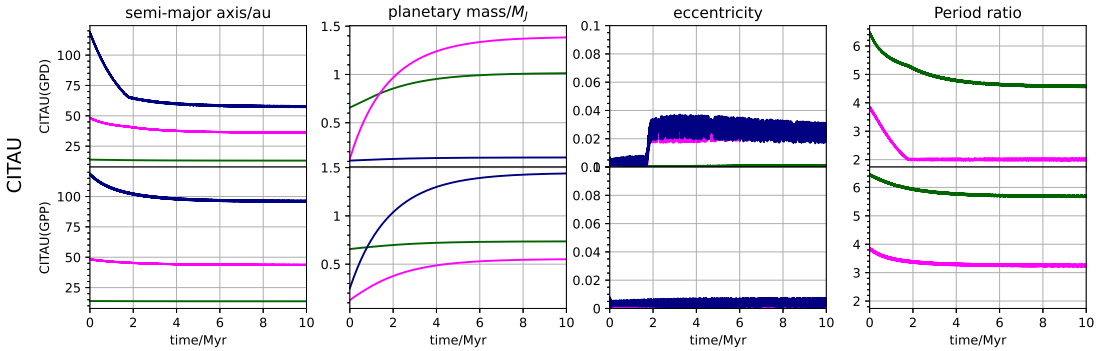

(b) CI TAU

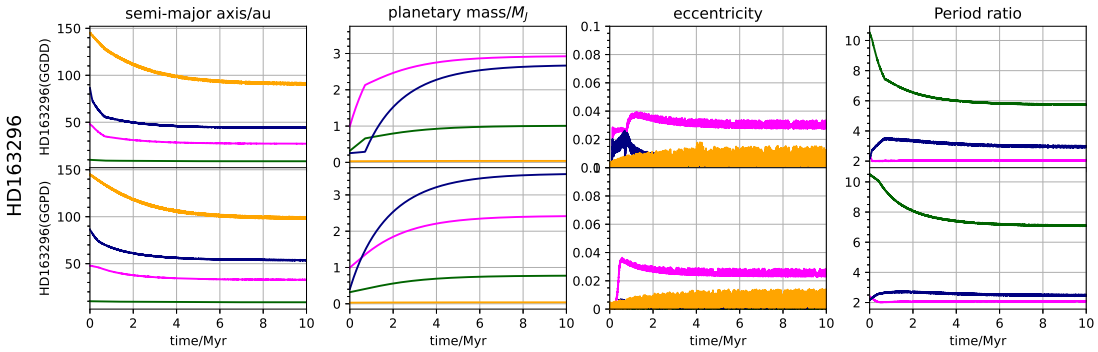

(c) HD 163296

Figure 5.5: Example evolution of semi-major axis, planetary mass,eccentricity and period ratio of adjacent pair of disk (a) AS 209 and (b) HD163296. Disk parameters are set to be the fiducial values.

in Figure 5.5 (a), in AA Tau(DD), the inner and outer planets migrate from $[72, 118]$au to $[28, 83]$au, where in AA Tau(PD) they migrate from the same initial locations to $[60, 98]$au. Similarly, Planets 1 (innermost), 2 (middle) and 3 (outermost) migrate from $[14, 48, 119]$au to $[13, 36, 58]$au in CI Tau(GPD) and to $[14, 44, 96]$au in CI Tau(GPP). Although the final position of the Planet 1 is not strongly affected by the initial mass assignment, the outer two planets of CI Tau(GPD) migrate further inward relative to those of CI Tau(GPP).

CI Tau(GPD) experiences significantly stronger migration because its Planet 3 has relatively small initial mass, and undergoes the fast Type I migration at the beginning. Such a high migration speed was sustained for around $1\,\mathrm{Myr}$ due to the inefficient pebble accretion. The fast approach between Planets 3 and 2 even excites the eccentricity of Planet 2 at around $2\,\mathrm{Myr}$. When Planet 3 further approaches Planet 2, its fast migration was hindered by both the resonance block and drop of the gas surface density due to gas accretion of of Planet 2. Consequently, both Planets 2 and 3 co-migrate with a period ratio very close to 2.0. On the contrary, in CI Tau(GPP) Planet 3 starts from gas accretion, and that lowers the surface density at the position of Planet 2. In effect, both Planet 3 and Planet 2 suffer from slower migration, and their final period ratio is larger than 3.0.

The initial mass assignment also affects the mass evolution, and in particular, results in distinct mass orders in CI Tau and HD 163296 systems. In CI Tau(GPD), Planet 3 undergoes pebble accretion throughout, while both Planets 1 and 2 start with gas accretion. The fast growing Planet 2 quenches the growth of Planet 1 by lowering the surface density at the inner side (see equation 5.17). It also prevents Planet 3 from migrating further inward via 2:1 resonance. Therefore, Planet 3 can neither grow efficiently nor migrate further inwards to trigger the gas accretion, as shown by the period ratio evolution. In the end, Planet 2 becomes the largest planet, and Planet 3 remains as a Saturn-size planet.

However, in CI Tau(GPP), Planet 3 initially starts with fast gas accretion, and its large accretion rate quenches the growth of both Planet 1 and 2. In effect, Planet 3 becomes a planet larger than Jupiter at $10\,\mathrm{Myr}$ epoch, while Planet 2 is the smallest because of the reduced gas inflow due to the gas accretion of Planet 3. The situation is similar in HD 163296(GGDD), except that Planet 3 entered the gas accretion stage late at around $1\,\mathrm{Myr}$, instead of always staying at the pebble accretion stage. Such a delay does not change the final mass qualitatively, but it is already sufficient to reverse of the mass order of Planets 2 and 3.

The period ratio evolution shows that some planet pairs can enter resonance via convergent migration. For example, the initial period ratio of the outer pair in CI Tau(GPD) is around 4.0. Due to the strong migration of Planet 3, the period ratio quickly decreases to 2.0 within $2\,\mathrm{Myr}$, entering 2:1 resonance. Since Planet 3 undergoes Type I migration throughout the disk lifetime, its migration speed can always match that of Planet 2 undergoing slower Type II migration, which ensures the period ratio always sticks to 2.0. We will discuss more about the overall period ratio distribution in section 5.4.5 and section 5.6.2 (also see Figure 5.15)

To summarise, the difference of the initial mass assignments can significantly change the orbital configuration the planetary system: when the the initial planetary mass is below $M_{\rm iso}$ (type 'D'), the planet migrates fast and its final position is much inward than those planets assigned with masses equal or larger than $M_{\rm iso}$. In general, the initial

mass assignment has less significant impact on the final planetary mass, because the fast migration of planet initially below $M_{\rm iso}$ can trigger the runaway gas accretion in a short timescale, and thus the final masses are not strongly affected. Nevertheless, in specific systems such as CI Tau (Planet 3), qualitative difference exists between the final masses, since the inner planet blocks the migration of the outer planet. Therefore, it is important to take into account of the planet-planet interaction and evolution feedbacks in such multi-planetary systems.

5.4.3 Sensitivity to α viscosity

As mentioned in section 5.2.2, the α parameter not only affects migration and accretion rates, but also changes the initial conditions, including the classification of the gaps and planetary mass estimation. To investigate the sensitivity to the α parameter, we also carried out simulations with $\alpha = 2 \times 10^{-3}$ and $\alpha = 5 \times 10^{-4}$, which differ by a factor of two with respect to the fiducial $\alpha (= 10^{-3})$. In general, as α increases, more gaps are classified as indistinguishable gaps, and vice versa. For example, for $\alpha = 10^{-3}$, the HL Tau system only has one set of mass assignment, but for $\alpha = 2 \times 10^{-3}$, there are four different sets as both Gap 2 and 3 can be interpreted as either gas gap or dust gap at larger α. Moreover, both $M_{\rm p,gas}$ and $M_{\rm iso}$ are scaled with α parameters. Therefore, while comparing the same system with different α parameters, we focus on the overall statistical trend rather than their specific case-by-case difference.

Figure 5.6 plots the final configuration of the planetary systems at the end of the disk dispersal. Both migration and accretion are enhanced when α increases. For example, while the innermost planet of HL Tau systems are located around $9\,{\rm au}$ with mass $\sim 2\,{\rm M_J}$ at $\alpha = 5 \times 10^{-4}$, they move further inward to around $3\,{\rm au}$ with mass $\sim 10\,{\rm M_J}$ at $\alpha = 2 \times 10^{-3}$. It is because the gas depth parameter K is inversely proportional to α (see equation 5.10), so increasing α effectively decreases the depth of the gas gap, therefore enhancing both rates of migration and accretion that are proportional to the gas surface density.

At $\alpha = 2 \times 10^{-3}$, planets are both massive and closer to each other, and thus their resonance overlap and systems become unstable (eccentricity > 1): three out of four mass assignment sets of HL Tau become unstable during the disk stage, and similar instability also happens to two sets of DL Tau. Details about the instability time and evolution of the unstable cases are in Figure 5.7. We plot the final configurations of the planetary systems just before they get unstable. On the same figure, we also plot the time when instability happens, as shown by the grey bars. Both sets of DL Tau become unstable at around $4\,{\rm Myr}$, while the three HL Tau sets become unstable at around $6\,{\rm Myr}$. All systems are much compact and massive than their initial states, as represented by the dashed circles.

Figure 5.7 also plots the evolution of two example planetary systems, DL Tau(DDG) and HL Tau(GGD), in terms of semi-major axis, mass, eccentricity and period ratio. Both of the systems become unstable due to the planet-planet scattering that is triggered by the close approach of the two planets. In the case of DL Tau, the instability happens at around $4\,{\rm Myr}$, with the innermost planet collide with the star. Similarly, for the HL Tau

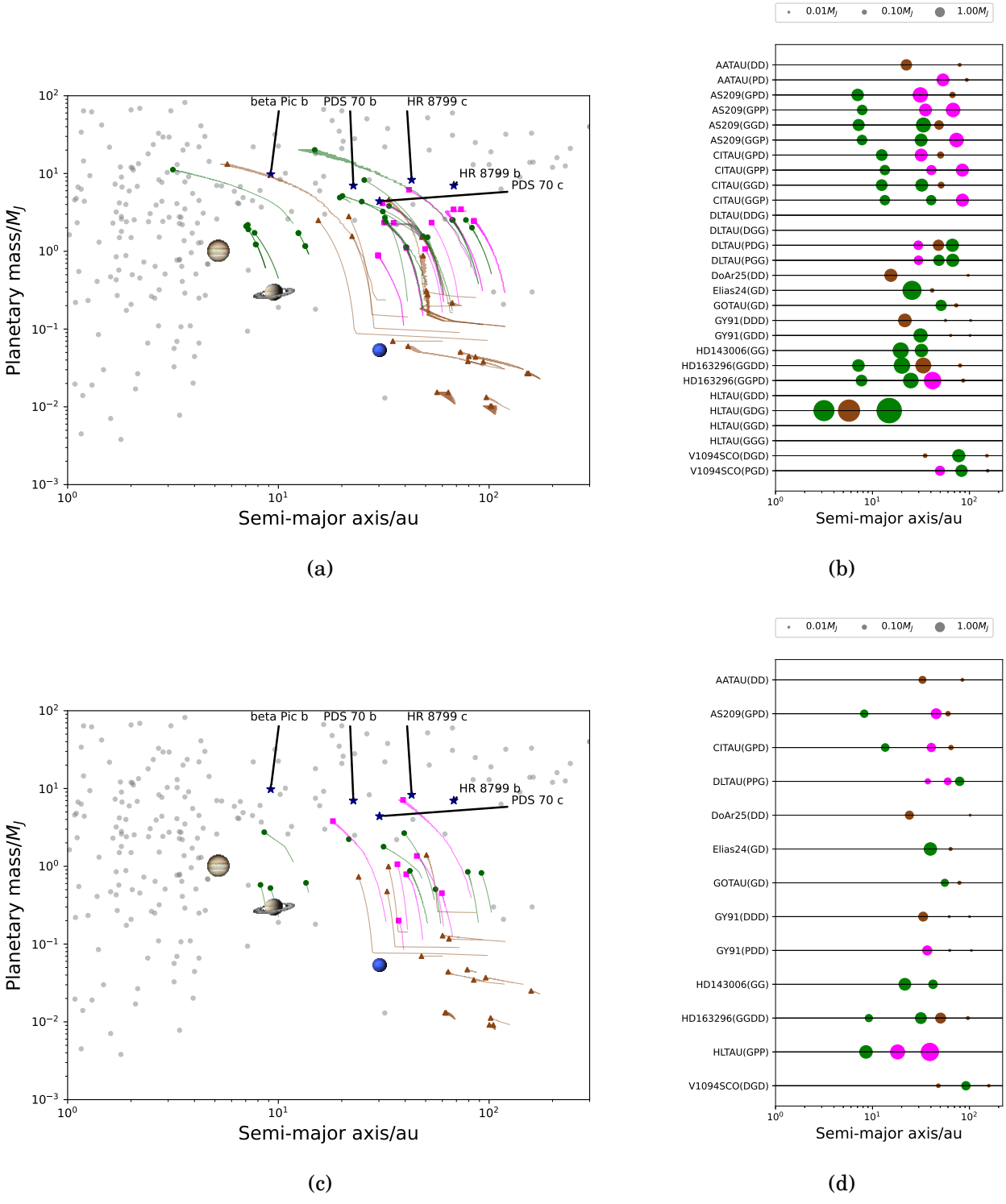

Figure 5.6: Same as Figure 5.3 but with different α viscosities. (a)(b): $\alpha = 2 \times 10^{-3}$. (c)(d): $\alpha = 5 \times 10^{-4}$.

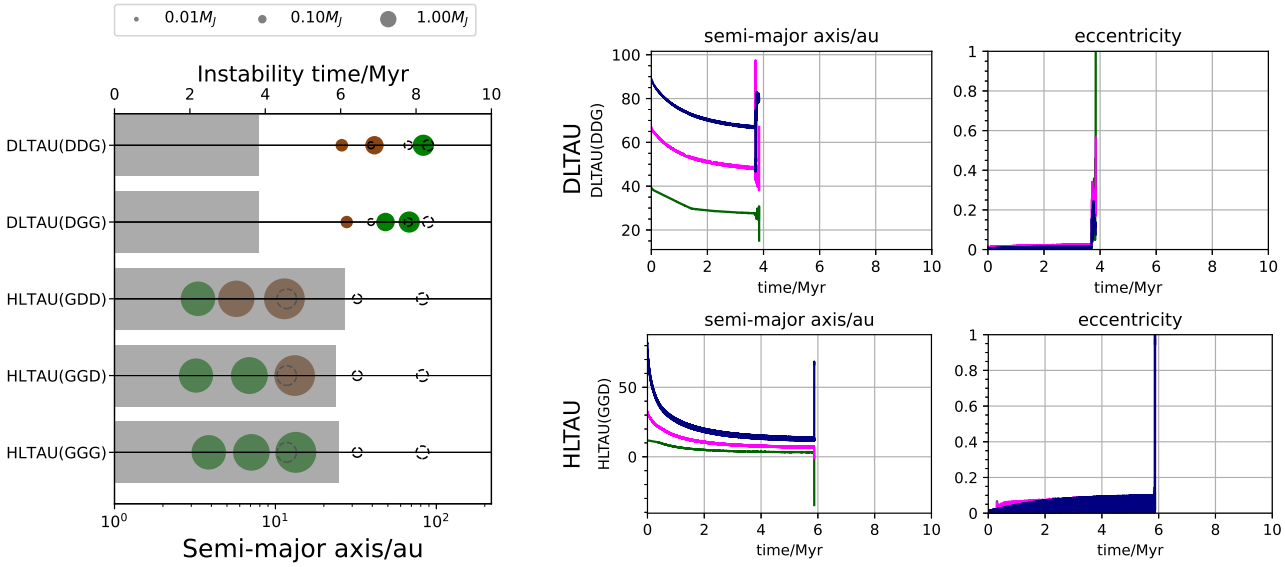

Figure 5.7: Left: configurations (just before instability) as well as the instability time of the systems that become unstable at the disk stage, when $\alpha = 2 \times 10^{-3}$. The dashed circles represent the initial location and mass of the planetary systems. Right:Evolution of DL Tau(DDG) and HL Tau(GGD), which are both unstable at the disk stage when $\alpha = 2 \times 10^{-3}$.

system, the outermost planet is scattered and ejected at around $6\,\mathrm{Myr}$. The scattering events in both systems are associated with strong excitation of eccentricity.

Since our migration and accretion models are only applicable to nearly circular orbits, we exclude these cases from the final configuration. It is worth to mention here that $\alpha = 2 \times 10^{-3}$ is much larger than the fiducial $\alpha(= 3 \times 10^{-4})$ of W20 suggested by Pinte et al. (2015), since the sharp edges of the HL Tau gap imply good dust settlement and thus weak turbulence level. Therefore, even though the majority of the HL Tau systems are unstable at $\alpha = 2 \times 10^{-3}$, this should only be interpreted as extreme cases, and the majority of the HL Tau systems are still stable.

We also plot the semi-major axis and mass evolution of planets for $\alpha = 2 \times 10^{-3}/5 \times 10^{-4}$ in Figure 5.6. Although the α parameter in principle affects all accretion and migration mechanisms, the effect is only significant for planets entering the gas accretion stage, i.e., the distant giant planets and Jupiter-like planets. These planets initially above $M_{\rm iso}$ migrate further inward and eventually become super-Jupiters or brown dwarfs when α increases, exhibiting greater overlap with the observed planetary population.

On the other hand, some planetary systems consisting of the Neptune-like planets, such as V1094 SCO, DoAr 25 and GY 91, are relatively less sensitive to α parameter since the majority of the planets always start from the pebble accretion stage. Some planets in these systems may enter gas accretion stage via inward migration, but by the time they reach $M_{\rm iso}$, the disk surface density has already decayed. Therefore, in this case changing α parameter does not affect their final configuration to a large extent. Finally, the evolution of distant low mass planets initially well below $M_{\rm iso}$ is rather insensitive to the change of α. These sub-Neptunes remain far away from the star regardless of α, and

have no counterpart in the observed population.

We can see that increasing α generally results in more compact, massive and inner planetary systems, since both migration and accretion rates are enhanced. Also for some specific planets that are close to $M_{\rm iso}$(e.g. AS 209 Planet 3), varying α changes the time when the runaway gas accretion is triggered and thus can affect the final architecture to larger extent. The planetary systems tend to become less stable at larger α, and particularly at $\alpha = 2 \times 10^{-3}$, several sets become unstable during the disk phase. At $\alpha = 5 \times 10^{-4}$, there is no unstable cases and the evolution does not change qualitatively as compared with those systems evolved with $\alpha = 10^{-3}$.

5.4.4 Effect of disk lifetime

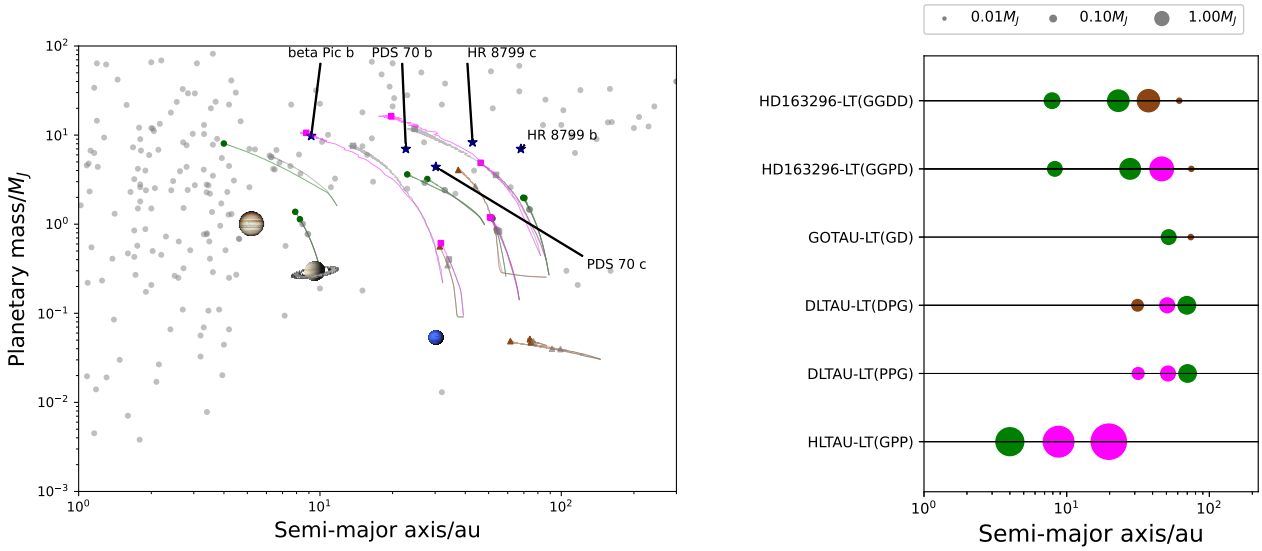

Figure 5.8: Same as Figure 5.3 but with $\tau_{\rm disk} = 3\,{\rm Myr}$. The total simulation time also changes to $15\,{\rm Myr}$. The grey dots and tracks denote the same system evolved with fiducial $\tau_{\rm disk} = 2\,{\rm Myr}$.

To investigate the impact of the disk lifetime, we select DL Tau, Go Tau, HD 163296 and HL Tau systems and re-run their simulation with longer disk lifetime $\tau_{\rm disk} = 3\,{\rm Myr}$. When the disk lifetime becomes longer, the disk surface density decays at a lower speed, therefore both the migration and accretion are expected to be enhanced, similar to increasing the α parameter.

Figure 5.8 plots the evolution of planets with longer disk lifetime. For comparison, we plot the results of the same systems evolved with our fiducial value ($\tau_{\rm disk} = 2\,{\rm Myr}$) in grey colour. Indeed, all planets migrate to more inward region and become more massive. However, unlike increasing the α viscosity, increasing the disk lifetime does cause any instabilities. We checked the evolution of the period ratios and found there is no significant difference as compared with the fiducial case, because the disk lifetime only extends the periods of the migration rather than increases the maximum migration speed. In this

sense, although the disk lifetime can boost both the migration and accretion, it cannot strongly affect on the dynamical structure of the planetary systems.

5.4.5 Period ratios of adjacent planets

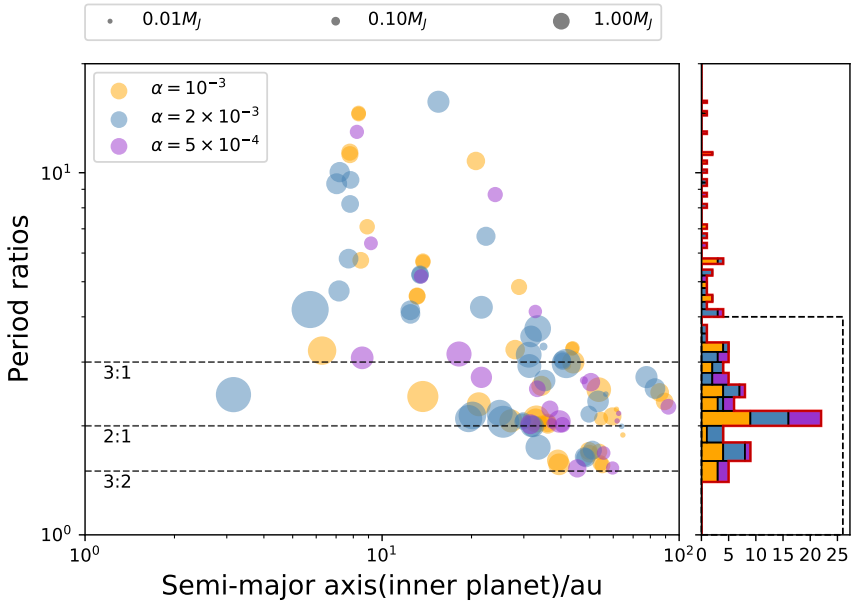

(a)

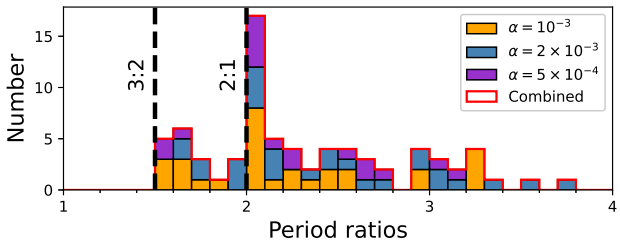

(b)

Figure 5.9: (a) Period ratios of all adjacent planet pairs against the semi-major axis of the inner planets in the pairs. Colors represent results at different α, and size of the dot is proportional to $2/3$ power of the mass of the inner planet. The histogram of the period ratios is plotted at bin-size = 0.2. (b) Enlargement of the dotted region in (a), with bin-size = 0.1.

Figure 5.5 plots the evolution of period ratios for the three systems. In this subsection, we show the period ratios of all adjacent planet pairs against the semi-major axis of the inner planet at the end of the disk dispersal, together with the corresponding histograms in Figure 5.9 (a). The majority of period ratios lie within the range from 1.5 to 4, with a long tail extending to nearly 14. The inner planets of those widely-separated planet pairs (e.g. DoAr 25) have generally small mass. They are initially sub-M_{iso} planets that undergo fast inward migration at the beginning, while the outer planets are slow-migrating planets

that are either very small (i.e., migration torque is weak) or very massive (i.e., gap is deep). Therefore, the outer planet cannot catch up with the inner planet, and the pair is gradually separated apart. As a result, the inner planets of these wide-separated pairs are located at inner region of $R_{\rm in} \lesssim 20$ au because of the significant inward migration.

Most planet pairs with relatively smaller period ratios (< 4) are distributed in the outer region with $R_{\rm in} \simeq 50$ au. Figure 5.9 (b) show that most of the rest of pairs have a period ratio < 2.8. There is a peak at 2.1, showing many planet pairs are 'trapped' outside of the strong 2:1 resonance. For those pairs initially with a sub-$M_{\rm iso}$ planet outside and a massive gas-gap-opening planet inside, due to the fast Type I migration of the outer planet, most of them reach period ratios that are close to 2.0. However, as the outer planet approaches the inner planet, the gas surface density drops because of the gas accretion of the inner planet (see equation 5.17), so the outer planet slows down.

The situation for those pairs consisting of two massive gas-gap-opening planets is similar: when two planets are far apart, the gas surface density at the location of the outer planet is higher as its accretion quenches the gas inflow, so the migration speed of the outer planet is likely to be higher than that of the inner planet, causing the outer planet to approach the inner one. As two planets get close, the difference between the gas surface density at their respective locations also decreases, so both the planets tend to co-migrate. In our simulations, we find no planet pair breaks into 2:1 resonance if the period ratio is initially above 2.

Figure 5.9 (b) also shows that around 20 planet pairs (including $\alpha = 2 \times 10^{-3}$ and 5×10^{-4} cases) are inside the main resonance zone with period ratios less than 2.0, although their initial period ratios (e.g. outer pair of DL Tau) are below 2. There is one obvious valley at 1.8, which is mainly due to 3:2 and higher order resonances. Also such closely-packed planet pairs are absent in our previous investigation concerning only the HL Tau (see Figure 8, W20). There is no planet pair in our simulation breaking into $3:2$ line, possibly because of the dense overlap of resonance zones near the $3:2$ resonance, so planet pairs close to this range experience very chaotic evolution and thus quickly become unstable if they are closer (see Fig 5.7).

To better illustrate the MMR states of the planet pairs, we plot the resonant angle evolution ($\alpha = 10^{-3}$) of the planet pairs in DL Tau and AS 209 systems in Figure 5.10. The resonant angle $\theta_{p+q:q}$ for the $p+q:p$ resonance is defined as :

$$\theta_{p+q:q} = p\lambda_{\rm in} - (p+q)\lambda_{\rm out} + q\varpi \tag{5.26}$$

where p and q are positive integers, the subscripts "in" and "out" are referring to the inner and outer planets that we considered in resonance. λ is the mean longitude and ϖ is the longitude of periastron of the inner or outer planet. Particularly, q is the order of the MMR.

Figure 5.10 shows that both 2:1 and 3:2 resonant angles of DL Tau librate around 0° with small amplitudes, implying that the inner and outer pairs of DL Tau are in good 2:1 and 3:2 MMR, and all three planets are in a chain of resonance. For AS 209 sets GPP and GGP, the outer two planets are massive and close to each other with period ratio < 2.0, causing the resonance zone to overlap. As a result, the same pair oscillates between 5:3 and 7:4 resonant states, so most of the time the respective resonant angles are librating

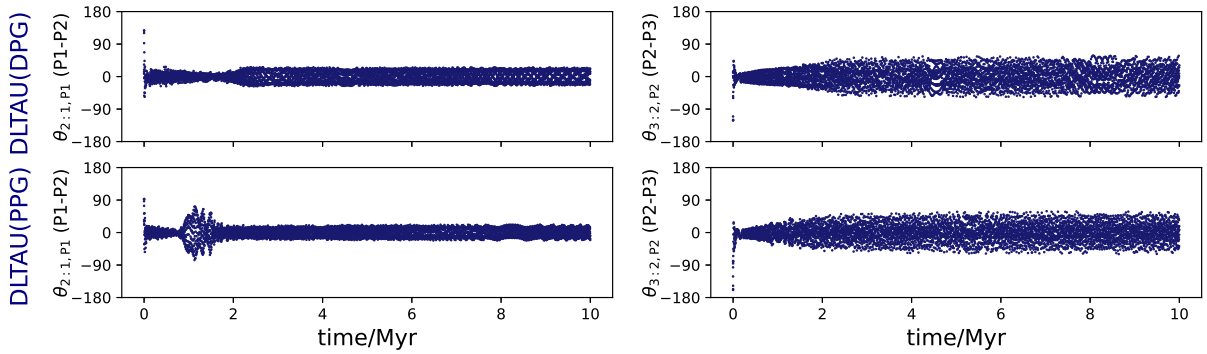

(a)

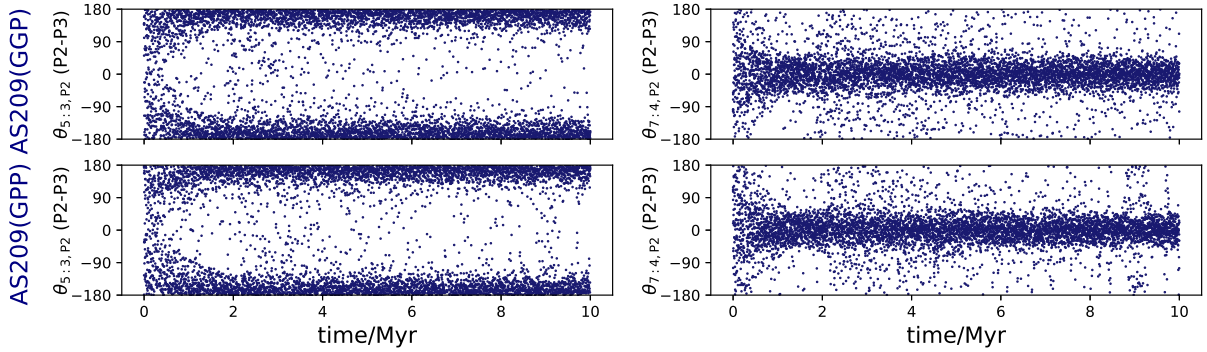

(b)

Figure 5.10: (a) 2:1 (of inner pair) and 3:2 (of outer pair) resonant angles of DL Tau system during the disk stage. (b) 5:3 and 7:4 resonant angles of Planet 2 in the outer pair in AS 209 sets GPP and GGP.

around $\pm 180°$ and $0°$.

Overall, we see that the planet pairs become more closely packed after the disk stage evolution. Moreover, the convergent migration let some closely-packed planet pairs naturally enter MMR states that in turn prevents them from closer approach. As we will show in the next section, in planetary systems such as DL Tau(PPG), the chain of MMR stabilises the configuration of against small perturbations, and they can survive for at least $10\,\mathrm{Gyr}$.

5.5 Evolution of planets after the disk dispersal under the stochastic perturbations

5.5.1 Perturbations from planetesimals

After the disk dispersal, the disk-disk interaction is practically negligible, so we continue evolving the planetary systems at the end of disk phase (§5.4) with their gravity alone in order to to examine the long-term orbital stability. This methodology has been applied in

W20, which demonstrated that planetary architectures predicted from the observed HL Tau disk are mostly stable up to $10\,\mathrm{Gyr}$. In this chapter, we further improve our previous methodology by incorporating the stochastic perturbative forces from numerous planetesimals surrounding each planet (e.g., Nelson & Papaloizou, 2004; Rein & Papaloizou, 2009; Hands et al., 2014; Chatterjee & Ford, 2015).

However, direct N-body simulations including star, planets and hundreds of planetesimals (e.g., Chatterjee & Ford, 2015) are computationally expensive, and thus it is not feasible to calculate the long-term evolution using such a full treatment. Hence, we first examine the statistical nature of the perturbative force by carrying out a simple N-body simulation consisting of a planetary system with a planetesimal disk, and then formulate our simplified implementation calibrated by the result as described in details below.

We perform direct calculation of gravitational force from the planetesimals as follows in order to calibrate the strength of the perturbative forces, mainly following Chatterjee & Ford (2015). We pick up the HD 143006 system as a representative system, which consists of two giant planets initially close to 2:1 period ratio. The initial semi-major axis ($21\,\mathrm{au}$, $37\,\mathrm{au}$) and planetary masses ($3.2\,\mathrm{M_J}, 1.5\,\mathrm{M_J}$) are the same as those at the end of the disk stage. We introduce a planetesimal disk containing 1000 planetesimal particles. The planetesimal disk extends from $a_{\rm min}$ = 1:3 period orbit inside of the inner planet to $a_{\rm max}$ = 3:1 period ratio outside of the outer planet, so as to avoid the edge effect (Chatterjee & Ford, 2015).

The left panel of Figure 5.11 shows the initial setup. All planetesimal particles have identical mass, and their initial semi-major axis follow $\propto R^{-1}$ power law distribution. The total mass of the disk is given by $3.3 \times 10^{-3}\,\mathrm{M_\oplus}(a_{\rm max}/\mathrm{au} - a_{\rm min}/\mathrm{au})$, so the mass of each particle is at the order of $\sim 10^{-4}\,\mathrm{M_\oplus}$, or roughly the mass of Ceres. In the simulation, we treat all the planetesimal particles as semi-test particles, which means they can mutually interact with the star and planets however not among themselves. The same N-body code `REBOUND` and the hybrid integrator `HERMES` are used with a typical time step equal to $0.016\,\mathrm{yr}$, and the integration finishes at 1000 orbital periods of the inner planet.

The perturbative force per unit mass of the i-th planet is computed by summing up a contribution from the k-th planetesimal at time t:

$$\boldsymbol{f}_{\mathrm{per},i}(t) = -\sum_{k\in\mathrm{planetesimals}} \frac{\mathcal{G}M_k}{|\mathbf{R}_k(t) - \mathbf{R}_i(t)|^3}\left[\mathbf{R}_k(t) - \mathbf{R}_i(t)\right], \tag{5.27}$$

where M_k and $\mathbf{R}_k$ denote the mass and the position vector of the k-th planetesimal with $\mathbf{R}_i$ being the position vector of the i-th planet.

The perturbative force is then normalised by the stellar gravity and averaged over each time interval $\Delta T = 0.16\,\mathrm{yr}$ to give the dimensionless, time-averaged strength $\bar{\eta}_{per}(t)$ as

$$\bar{\eta}_{per,i}(t) = \left|\frac{1}{\Delta T}\int_{t-\Delta T}^{t} \boldsymbol{\eta}_{per,i}(t')dt'\right| \tag{5.28}$$

Our simulation uses natural units, i.e., $\mathrm{M_\odot}$ and au, and the gravitational constant is set to be unity. Therefore, the unit time corresponds to $1/2\pi\,\mathrm{year} \sim 0.16\,\mathrm{year}$.

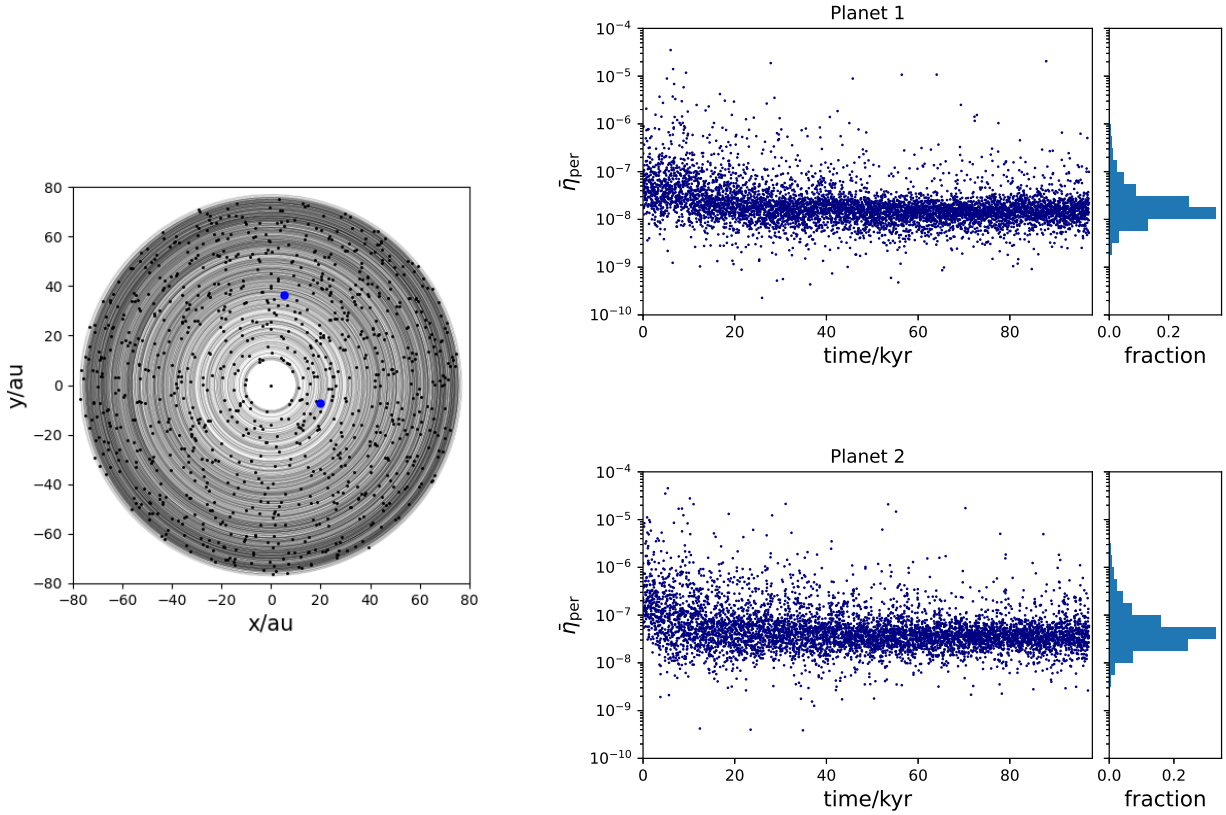

Figure 5.11: Left: Initial setup of the planets with a planetesimal disks. Black dots are planetesimals, and blue dots are the planets. The initially orbits of the planetesimals are also plotted. Right: Time-averaged $\eta_{\rm per}$ against the simulation time for both planet 1 and planet 2. The perturbative force is averaged over $0.16\,{\rm yr}$ to be consistent with our random force implementation in the previous section.

where

$$\boldsymbol{\eta}_{per,i}(t) = \frac{\boldsymbol{f}_{{\rm per},i}(t)}{f_{*,i}} = \frac{\boldsymbol{f}_{{\rm per},i}(t)}{\mathcal{G}M_* R_i^{-2}(t)}. \tag{5.29}$$

The right panels of Figure 5.11 plot the averaged dimensionless strength of the perturbative force against the time, with upper and lower panels correspond to Planets 1 and 2, respectively. Initially, $\eta_{\rm per}$ fluctuates with a relatively large amplitude. After a few hundreds orbits, the system approaches equilibrium and the fluctuation level decreases. While the total range of $\bar{\eta}_{per,i}$ covers nearly three orders of magnitude, histograms show that the majority of the data points are in the range between 10^{-7} and 10^{-8}. The histograms also indicate that the peak of $\eta_{\rm per}$ distribution is a few times larger for Planet 2 relative to Planet 1, because the stellar gravity acting on outer Planet 2 is weaker. This difference is not significant in terms of the order of magnitudes.

We also investigate the dependence of $\bar{\eta}_{per}$ on the total mass of the planetesimal disk and the particle number. The peak value of $\bar{\eta}_{per}$ is found to scale linearly with the total mass of the planetesimal disk but it is not sensitive to the number of planetesimal particles

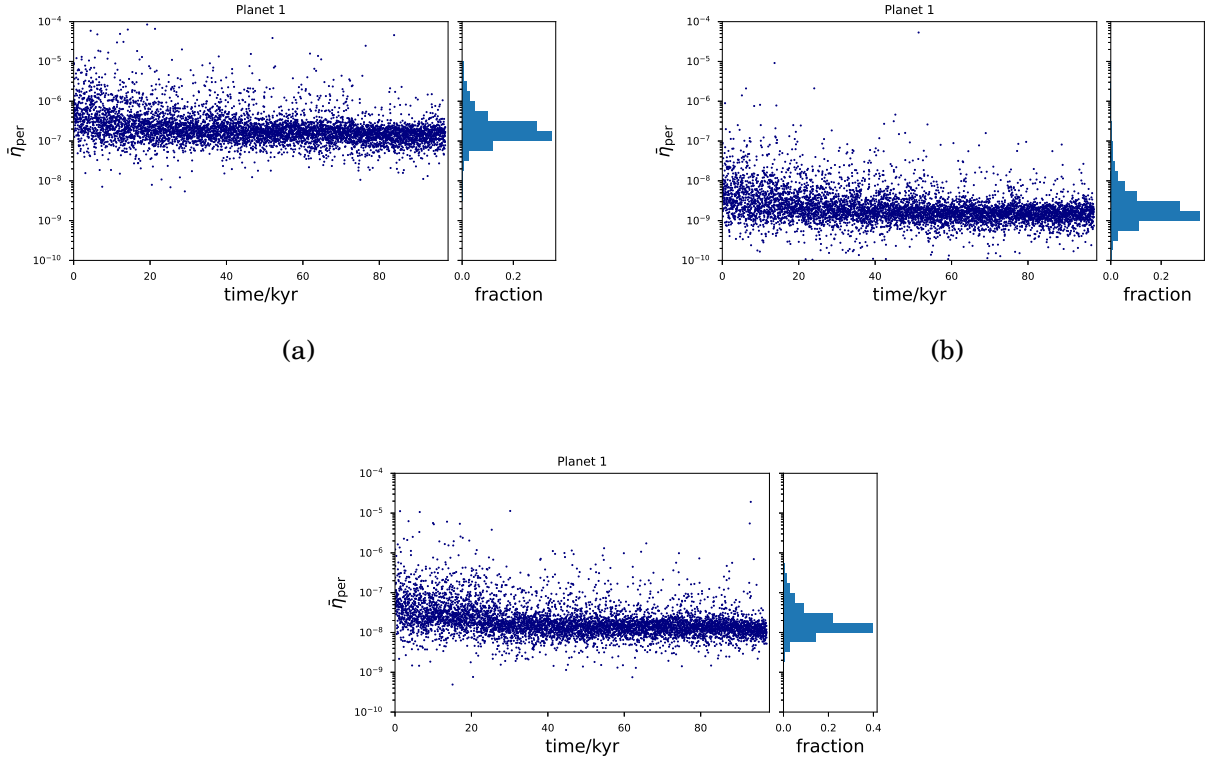

Figure 5.12: Same as Figure 5.11 (right panel) but with: (a) 10 times disk mass; (b) 10% disk mass; (c) 2000 planetesimal particles.

as long as the total disk mass is the same (see Figure 5.12). Therefore, even considering the uncertainty of the total mass of the planetesimal disk and the variation of the semi-major axis, $\bar{\eta}_{per}$ is expected to be less than $\sim 10^{-6}$. We will consider next if the planetary systems are stable against the mutual gravity and the stochastic perturbations at this level.

5.5.2 Numerical method to test the long-term stability

On the basis of the simulation run in the previous subsection, we consider a simplified model incorporating the perturbative force in the post-disk stage, and evolve the systems up to $10\,\mathrm{Gyr}$. The i-th planet now obeys the following stochastic equation of motion:

$$\ddot{\boldsymbol{R}}_i = \boldsymbol{f}_{\rm grav,i} + \boldsymbol{f}_{\rm per,i}, \tag{5.30}$$

where $\boldsymbol{f}_{\rm per,i}$ represents the perturbative force per unit mass acting on the i-th planet.

We assume that the magnitude of $\boldsymbol{f}_{\rm per}$ is given by $f_{{\rm per},i} = \eta_{\rm per} f_{*,i}$, with $\eta_{\rm per}$ being the dimensionless strength factor. In each simulation run, we fix the value of $\eta_{\rm per}$, but repeat many runs by systematically varying the value. The perturbative force is assumed to be uncorrelated beyond each time step: the direction of the perturbative force acting on

each planet is uniformly random between $0°$ and $360°$ at each time step $\Delta t = 0.16\,\mathrm{yr}$.

In this post-disk stage, we integrate the system using the `WHFAST` integrator (Rein & Tamayo, 2015). We reset the simulation epoch as $t = 0$ at the beginning of this stage. Systems are integrated by varying η_{per} from 10^{-1} to 10^{-8}. When one of the planets is ejected from the system (semi-major axis $a_p > 10^3\,\mathrm{au}$), collides with either its hosting star ($a_p < 0.01\,\mathrm{au}$) or the other planets (mutual distance $< 2\,\mathrm{R_J}$), we regard this system as unstable and stop the simulation. Otherwise, the system is integrated up to $10\,\mathrm{Gyr}$.

5.6 Stability of the resulting multi-planetary systems

5.6.1 Stability under the presence of perturbative forces

Based on the model we described in section 5.5, we examined the instability time of the multi-planetary system with random perturbative force in various magnitudes ($10^{-8} \leq \eta_{\mathrm{per}} \leq 10^{-1}$). We eliminate those systems that has already become unstable during the disk phase and only carry out stability check for the remaining systems.

Figure 5.13 plots the instability time against η_{per} for all the 23 realisations from the 12 disk systems (Table 5.1) of fiducial parameters in thin grey lines. Different panels depict six disk systems, respectively, so as to highlight their behaviour. The amplitude of the instability time is dependent on the specific architecture of the systems and varies within two orders of magnitude, but is roughly proportional to $\eta_{\mathrm{per}}^{1.5}$ for $\eta_{\mathrm{per}} > 10^{-6}$, except HL Tau. Note that we stop the run at $t = 10\,\mathrm{Gyr}$, and most of the systems survive for at least $10\,\mathrm{Gyr}$ for the realistic range of the perturbative forces, *i.e.,* $\eta_{\mathrm{per}} \leq 10^{-6}$.

As expected, systems become destabilised in general as the number of planets increases. For the same system, different initial mass assignments for planets do not significantly change the instability time that varies just within one order of magnitude. The result also shows that the minimum separation between planets plays a decisive role in the instability: sets GPP and GGP of CI Tau exhibit stronger resistance to the perturbation than their counterparts, as the minimum planet-planet separation in these two sets are larger than those of rest. As another evidence, both GY 91 and AS 209 have three planets, yet GY 91 is more stable than AS 209 because the closest pair in AS 209 (Planet 2 and 3) has smaller separation, and the planets are also more massive.

We also examine the instability time versus the perturbative strength η_{per} for planetary systems evolved with large $\alpha = 2 \times 10^{-3}$ and small $\alpha = 5 \times 10^{-4}$, as plotted in Figure 5.14. In Figure 5.14, we select three systems, CI Tau, GY 91 and HL Tau, as examples to show the α-dependence of the instability curve. In section 5.4.3 we have seen that $\alpha = 2 \times 10^{-3}$ generally boosts both the migration and accretion rates during the disk stage, therefore the planetary systems are closer to the star and become more massive. In the case of HL Tau, its stability curve moves down as α increases, showing greater instability. However, such a trend is not obvious for the rest of the systems. For GY 91, the outer two planets are dust planets, therefore their evolution are not sensitive to change of α. For CI Tau,

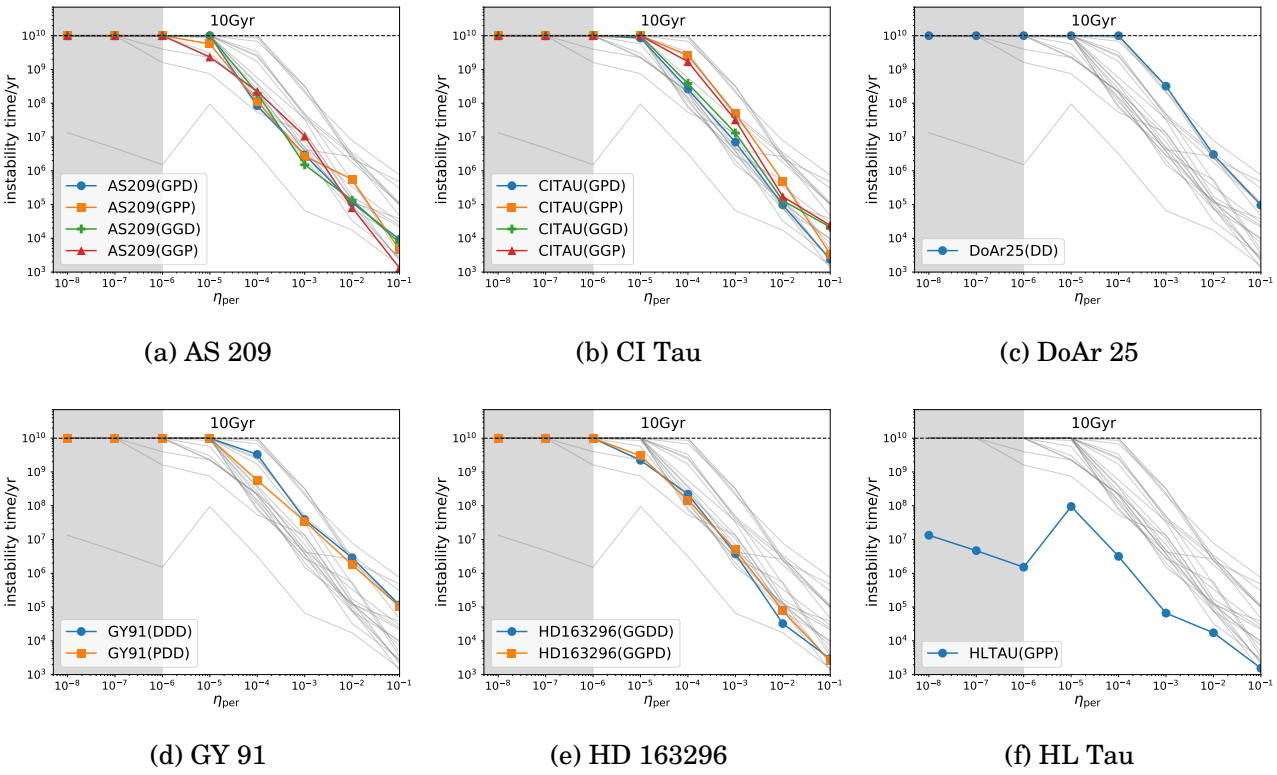

(a) AS 209 (b) CI Tau (c) DoAr 25

(d) GY 91 (e) HD 163296 (f) HL Tau

Figure 5.13: Instability time against the dimensionless magnitude of the stochastic perturbative force $\eta_{\rm per}$. Grey lines correspond to the 23 different realizations from the twelve systems (Table 5.1 for $\alpha = 10^{-3}$). The shaded region ($\eta_{\rm per} < 10^{-6}$) is the realistic range for the planetesimals. Six different panels highlight the behaviour of the selected systems, together with different initial mass assignments of the planets.

although the planetary masses increases with α, the separation between the planets do not change much due to the convergent migration, therefore the stability of the CI Tau system is not strongly affected within $10\,\mathrm{Gyr}$ range. At $\alpha = 5 \times 10^{-4}$, the majority of the systems stay stable for $10\,\mathrm{Gyr}$ when $\eta_{\rm per} \leq 10^{-5}$. Even the least stable HL systems cut-off at $\eta_{\rm per} = 10^{-7}$.

Clearly, the HL Tau system with $\alpha = 10^{-3}$ seems to be much less stable than the other systems: it becomes unstable at around $10\,\mathrm{Myr}$ after the disk dispersal regardless of the $\eta_{\rm per}$ down to 10^{-8}, indicating that its final configuration is sensitive to even minor perturbations. Compared with the conclusion of W20 that the HL Tau systems are stable in general after the disk stage, this different result is due to the α adopted: W20 adopted $2 \times 10^{-4} \leq \alpha \leq 6 \times 10^{-4}$, which are much smaller than the fiducial value $\alpha = 10^{-3}$ adopted here. As we will later discussed in section 5.6.2, the special stability behaviour of the HL Tau system ($\alpha = 10^{-3}$) is because a scattering event happening in the last Myr drives all three planets out of the resonance, leaving the system in a marginally stable states. Since no similar behaviour has been observed in other systems, this marginally stable HL Tau system can be regarded as only a serendipitous case. Nevertheless, this may be a good example to show how the stability can be affected by the resonant states.

Moreover, HL Tau systems are less stable because its initial disk mass ($0.105\,\mathrm{M}_\odot$) is the largest among all disks, and therefore the resulting planets in HL Tau are the most

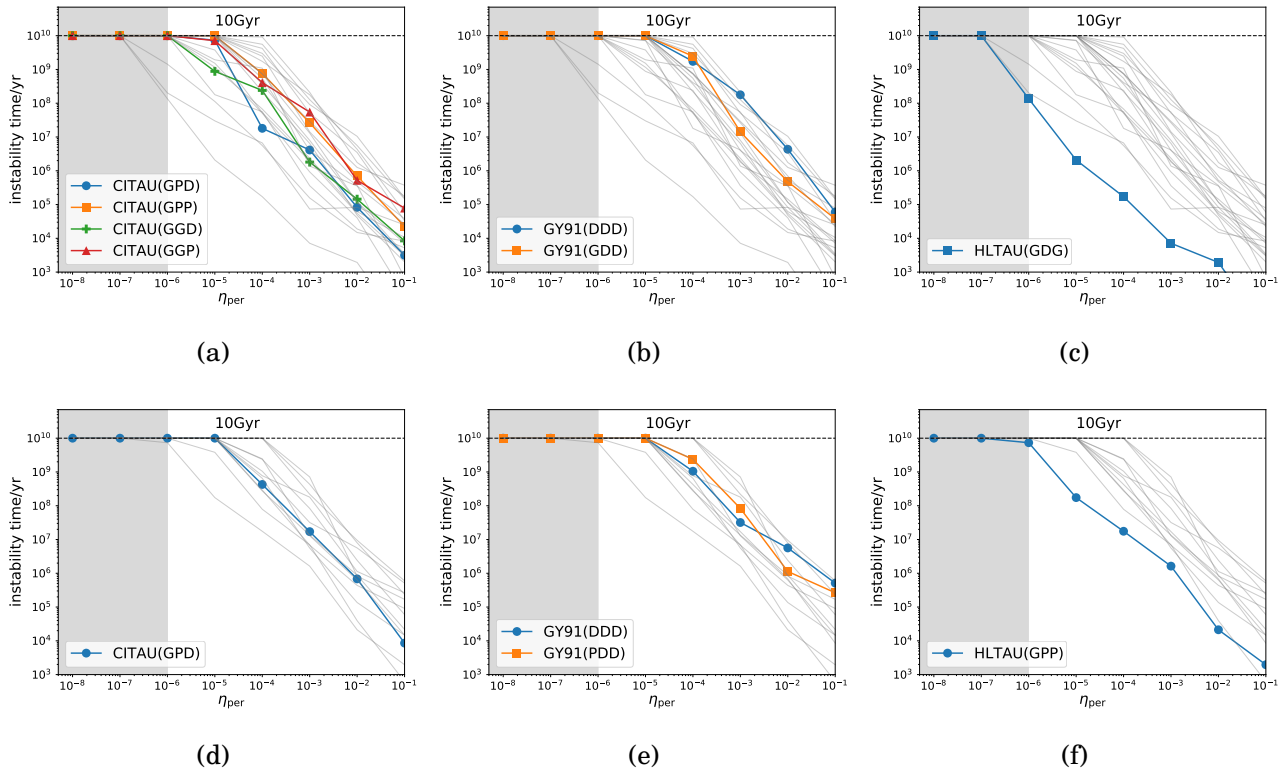

(a) (b) (c)

(d) (e) (f)

Figure 5.14: Same as Figure 5.13 but with different α. (a)(b)(c): Instability time of CI Tau, GY 91 and HL Tau systems evolved with $\alpha = 2 \times 10^{-3}$. (d)(e)(f): Instability time of CI Tau, GY 91 and HL Tau systems evolved with $\alpha = 5 \times 10^{-4}$.

massive and closest to the star in all systems. Theoretically, the semi-major axis a_p of a single, isolate planet under such stochastic perturbative forces is expected to undergo random walk with the root mean square deviation $\sqrt{\langle \Delta a_p^2 \rangle} \propto \sqrt{Dt}$, where t is the simulation time and $D \propto \eta_{\rm per}^2 M_*^2 R_p^{-4}$ is the diffusion constant (equation 46, Rein & Papaloizou, 2009). Therefore, under the perturbative force with the same $\eta_{\rm per}$, the inner planets deviate faster from their original semi-major axis and have shorter instability time, as the diffusion constant D increases with decreasing R.

Our analysis shows that given the fiducial parameters that we adopt, the perturbation from the planetesimals can only marginally affect the most massive and unstable systems. In order for the majority of the systems to be unstable, either the mass of the planetesimals have to be much larger, or additional source of perturbation (e.g., close stellar flyby) is required to significantly destabilise the configuration reached at the end of the disk dispersal. We discuss the implications in section 5.7.3.

5.6.2 Consistency with previous stability criteria

We have shown that most of the systems are stable for at least $10\,\mathrm{Gyr}$ even under the presence of stochastic perturbative forces due to planetesimals. It is interesting to check the consistency of these results with the theoretical prediction. We compute the instability time from the configuration at the end of the disk stage using the same formula Morri-

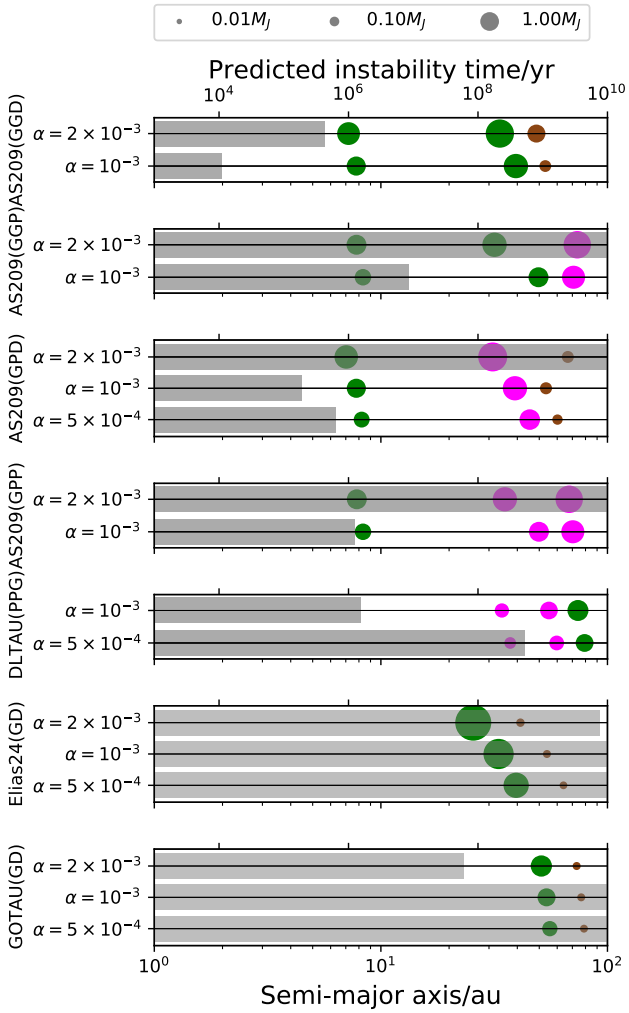

Figure 5.15: Instability time predicted by Morrison & Kratter (2016) for each system based on the configuration at the end of the disk stage with different α values.

son & Kratter (2016) that we adopted in (section 5.1, W20). It is worth to mention that the planetary configurations out of our simulation have a wide distribution over mass and semi-major axis; they are different from the theoretical initial conditions considered in Morrison & Kratter (2016), who concern the general stability criterion of equal-mass multi-planetary systems. Therefore, applying the formula of Morrison & Kratter (2016) to our systems should be interpreted as an extrapolation of their original result, and deviations are expected if the system configuration is largely different from those valid in the original context. We would also like to stress here that the instability time predicted by Morrison & Kratter (2016) neglects the possible effect of the perturbative force.

Having said so, however, we found that most of the systems are consistent with the prediction of Morrison & Kratter (2016) at the level of $10\,\mathrm{Gyr}$. Thus we focus on all the configurations that are predicted to be unstable according to the formula of Morrison & Kratter (2016). Figure 5.15 indicates the instability time of those systems (grey bars in the upper axis) together with their planetary configurations (filled circles in the same manner of the right panel of Figure 5.3). For each set, we also plot the same set initialised and evolved with different α at the disk stage whenever exist. In the same figure, the configurations at the end of the disk systems evolved with the respective α are also plot-

ted for reference. Note that we exclude the five cases that have already become unstable at the disk phase for $\alpha = 2 \times 10^{-3}$ case.

Figure 5.15 show that all the realisations that are predicted to be unstable by Morrison & Kratter (2016) have an outer planet pair with a period ratio close to or less than 2.0. Also in most of the cases, the third planet is relatively far away from the outer pair. For example, the outer pair in AS 209(GPD) and AS 209(GGD) with $\alpha = 10^{-3}$ consists of a super-Jupiter and a sub-Saturn in the outer region, while the innermost planet is around $10\,\mathrm{au}$. Since the instability time is computed from the minimum orbital separation of all planet pairs within planetary system, such configurations are predicted to be unstable for less than $1\,\mathrm{Myr}$. The predicted instability time for GO Tau(GD), Elias 24(GD), DL Tau(PPG) decreases with increasing α, because a large α value promotes both migration and accretion and results in a more compact systems. However, for AS 209 systems evolved with $\alpha = 2 \times 10^{-3}$, the scattering between Planet 2 and 3 increases the separation between them, therefore the final configurations at $\alpha = 2 \times 10^{-3}$ is more stable than those at $\alpha = 10^{-3}$.

However, this configuration is largely different from the theoretical setup investigated by Morrison & Kratter (2016) in at least two aspects. Firstly, the planetary masses in the pair are not equal in our simulation; for AS 209(GPD), the mass difference is more than 10 times. The unequal mass affects the metric that is used to normalise the orbital separation and therefore the predicted instability time. Secondly, while Morrison & Kratter (2016) consider multi-planets with equal normalised orbital separation, in our simulation the separations of planet pairs may differ by a large extent. As a result, the closest planet pair experiences much weaker influence from the third planet as compared with that investigated by Morrison & Kratter (2016). Therefore, these configurations are not in the applicable range of the prediction formula.

Besides the difference in configuration, we think the MMR may be another reason to cause the underestimate of the instability time for some systems such as DL Tau(PPG). As we show in Figure 5.10, all two planet pairs of DL Tau are in either 2:1 or 3:2 MMR. Since the planet pairs are locked in a chain of resonance, their configurations are more resistant to the small perturbations and thus can be stabilised over long time. This argument is also consistent with our previous findings in W20 that the instability time prediction based on the mutual separation can underestimate the stability when the planets are in a chain of resonance.

We noticed that the fiducial set of HL Tau is the only case whose stability is overestimated. Considering three out of four sets in the $\alpha = 2 \times 10^{-3}$ cases do not even survive the disk stage, this special set is in marginal stability that is vulnerable to even minor perturbations. Figure 5.16 plots the evolution of HL Tau at the disk stage. At around $9.5\,\mathrm{Myr}$, there is a scattering event that changes both the semi-major axis and boosts the eccentricity to the level as high as 0.1. Although the change of the semi-major axis is not significant, this scattering significantly changes the resonant states, as shown by the sudden change of the period ratios as well as the resonant angles. Before $9.5\,\mathrm{Myr}$, both 3:1 resonant angle of the inner pair and 2:1 resonant angle of the outer pair librate; however, after the scattering takes place, both resonant angles start to circulate. Since all three planets are massive, their resonant zones may overlap and once the planet is out of the resonant lock, the system becomes chaotic and unstable.

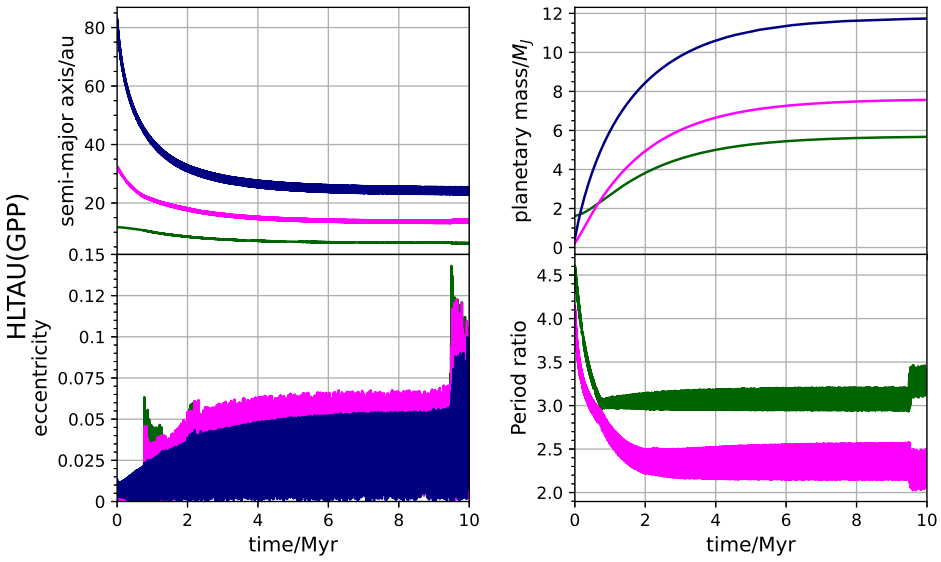

(a)

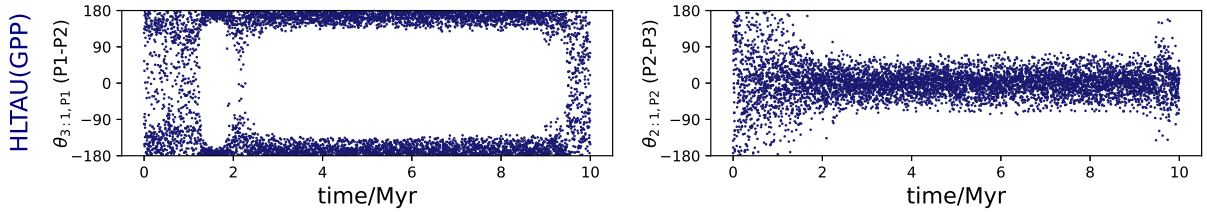

(b)

Figure 5.16: (a) Similar to Figure 5.5 but the evolution of the HL Tau system at $\alpha = 10^{-3}$. (b) 3:1 resonant angle of the inner pair and 2:1 resonant angle of the outer pair. Both angles start to circulate within the last $1\,\mathrm{Myr}$ due to a scattering event that excites the eccentricity.

5.7 Discussion

5.7.1 Result sensitivity to observation data

In our study, we deduce the initial planetary configurations as well as some disk parameters from the ALMA observation. Therefore, it is worth to discuss to what extent the final results are subject to the observational uncertainties. The initial semi-major axis of the planet suffers from the least uncertainties as the position of the gap can be directly identified on the continuum image with errors less than $1\,\mathrm{au}$. The final configuration and stability are not sensitive to such a small uncertainty, because the planetary migration in the disk stage can cause up to a few tens of au change in the semi-major axis, which is one order of magnitude larger than this uncertainty. Moreover, in many cases the final positions of the outer planets are determined by the inner planet due to the resonance chain, so the outer planet will always stop at outside of the MMR and co-migrate with the inner one. Therefore, the initial position difference will not affect the evolution outcome as well as the conclusion of the stability.

The planetary mass is deduced indirectly from the gap width, and it suffers from much larger uncertainty as compared with the gap location. The non-axial symmetric structure of the gap can affect the identification of the gap edge to a few tenths of au. The gap width is also subject to the definition of the gap edge that differ in different studies and simulations, which may be translated to a factor of two difference in the final mass prediction. In section 4.3.3, we have introduced two fudge factors to take account of these uncertainties. For the disk parameters, the reference gas scale height is calculated from the stellar luminosity. Although the luminosity L_* of the young star in PPD has a pretty large error range up to about 60%, the scale height only weakly scales with L_* to the $1/4$ power and is not sensitive to this observational error.

Due to the highly non-linear nature of the disk stage evolution, discussions about how the observational error affects the final results via planet-disk interaction can only be carried out in a semi-quantitative fashion. In terms of the accretion, if a planet has an initial mass close to $M_{\rm iso}$, a factor of two change in initial mass directly changes the time to enter the run-away gas accretion stage, which eventually leads to a factor of few or even one order of magnitude difference in final planetary mass, as shown by our simulation results (see HD 163296 in figure 5.5). In terms of the migration, although both the planetary mass and scale height deduced from the observation data can affect the migration speed in terms of the K factor (see equation 5.10), the final positions of the planets are mostly determined by the inner planets due to the resonance chain, and therefore the final orbital configuration is not strongly affected. Only when the change is applied to the innermost planet, it may cause a factor of few difference in the final semi-major axis (see AATAU in figure 5.5). However, in terms of stability, none of the change in semi-major axis or initial mass qualitatively changes the final stability of the systems, as the MMR always keeps the outer planet at a safe distance as long as the convergent migration happens. The decisive factor is still the viscosity of the disk or the migration recipe that determines how close two planets can approach each other.

To summarise, the impact of the observational error to the final results is limited to quantitative differences in the architecture. In particular, the stability of the final configurations is predominantly affected by the planet-disk interactions that are specified by the disk parameters (e.g., viscosity) and models, rather than the uncertainties of initial conditions due to the observational error.

5.7.2 Comparison with the previous result concerning the HL Tau system

Our previous study W20 investigates the evolution of HL Tau system at the disk stage, assuming that all the three planets have opened gas gaps. Although the fiducial disk parameters and adopted initial masses are different, in both studies the HL Tau system evolve to become a widely-separated planetary system consisting of three super-Jupiters at the end of the disk stage. However, due to the relatively larger viscosity adopted here ($\alpha = 10^{-3}$ in contrast to $2 \times 10^{-4} \leq \alpha \leq 6 \times 10^{-4}$ in W20), the final masses of the HL Tau planets are a few times larger. The resulting HL Tau system at $\alpha = 10^{-3}$ is only marginally stable. If we adopt $\alpha = 2 \times 10^{-3}$, three out of four initial mass assignment sets become unstable during the disk stage. We note that only one out of 75 sets in W20

becomes unstable during the disk stage.

For the rest of the ALMA disks, overall the final architecture exhibits greater diversity in terms of semi-major axis and masses, partially due to their diverse initial conditions and different gap interpretations. The semi-major axis of the planets ranges from around $10\,\mathrm{au}$ to over $100\,\mathrm{au}$, and some planet pairs are in 3:2, 5:3 and 7:4 MMR with period ratios less than 2.0, which are absent in previous HL Tau study. While the final planetary masses of some systems (e.g., HD 163296, CI Tau, AS 209) are similar to HL Tau, some planets are strongly quenched in mass growth due to both inefficient pebble accretion at the outer disk and failure to trigger the run-away gas accretion. These planets remain as Neptune-sized planets and co-migrate with the inner planets until the end of the disk dispersal.

Despite the diversities of the architecture, the dynamical structure of the systems are consistent with what we found in W20. Most systems naturally enter good MMR states because of the convergent migration, and under the resonance lock they can stay stable for at least $10\,\mathrm{Gyr}$ with even minor perturbations. Our conclusion in W20 still holds for other ALMA disks that the final configuration of the planetary systems is significantly stabilised by the planet-disk interaction. Once the systems survive the disk stage without being gravitationally excited, it is hard to induce instabilities afterwards unless significant level of perturbation ($\eta_{\mathrm{per}} > 10^{-6}$) is present.

5.7.3 Implications possible scenarios of close-in planet formation

our results show that those planetary systems predicted from the disks are likely to be stable. The stable configuration due to the convergent migration may indicate that the production of Hot Jupiters or planets with large spin-orbit misalignment via instability is not efficient. However, we see that given large viscosity at the disk stage and/or strong enough perturbation $\eta_{\mathrm{per}} > 10^{-5}$ after the disk dispersal, the system can be disturbed and become unstable in short time scale, which may eventually lead to the formation of Hot Jupiters via tidal circularisation of eccentric orbit caused by planet-planet scattering (e.g., Rasio & Ford, 1996; Nagasawa et al., 2008).

Due to the relatively weak perturbations from the planetesimals, an external source of strong perturbation may be critical to generate short-period giant planets. Such perturbative source might be realised by stellar flyby (e.g., Rodet et al., 2021), as recent observations have revealed that stars in a cluster are likely to have a short period planets including Hot Jupiters, as compared to field stars (Winter et al., 2020). Other mechanisms, such as interaction with free floating planets (Varvoglis et al., 2012; Goulinski & Ribak, 2018), can also result in loosely bounded planetary orbits at high eccentricity. These possibilities motivate future observation to better constrain the viscosity in a PPD, possible sources as well as the realistic ranges of the possible perturbations.

5.8 Summary

Despite numerous important and interesting progresses in theoretical and observational understanding of exoplanetary systems over the last couple of decades, there is no accepted formation scenario that explains their universality and diversities simultaneously. One of the main difficulties that hinder establishing the successful scenario is the lack of the realistic initial conditions at the protoplanetary disk phases. Most of past theoretical studies have tried to construct exoplanetary systems simply by adopting somewhat artificial initial conditions. Given a lot of uncertainties in the physical processes in the formation and evolution of protoplanetary disks, the limitation due to the approach is inevitably large.

This difficulty is expected to be less serious thanks to recent discoveries of ring and gap substructures in many dust disks by ALMA. Following a conventional planetary interpretation for the substructures, one can bypass the uncertainties of the initial conditions, perform numerical simulations, and confront the resulting architecture of the planetary systems.

In this chapter, we perform two-stage N-body simulations, and investigate the outcomes of 12 ALMA disks, the initial conditions of which are based on the orbital and mass prediction in Paper I (section 5.2.2). During the disk stage, we include the planetary migration (section 5.3.1) as well as pebble/gas accretion (section 5.3.2) schemes to mimic the interaction between the planet and the disk. After the disk dispersal, we examine the long term orbital stability of the configurations by integrating the systems up to $10\,\mathrm{Gyr}$.

W20 applied the above strategy for the HL Tau, and concluded that the resulting three-planet systems are mostly stable up to $10\,\mathrm{Gyr}$ from its current epoch. This chapter generalized and improved the work by W20 in four major aspects. First, we take into account different mass assignment possibilities for embedded planets following Paper I. Second, we consider the pebble accretion, in addition to the gas accretion, during the planet-disk interaction phase. Third, we examine the stability of planetary systems by including the effect of perturbative gravity due to surrounding planetesimals after the disk dispersal, in addition to those from the central star and other planets. Finally, we apply the methodology to twelve ALMA disks with clear multi-gap structures.

Our main findings of this chapter are summarized as follows.

1. After the disk stage evolution, the planet population exhibits a wide distribution in both semi-major axis and mass (Figure 5.3) and starts to overlap with the observed planets. Based on their evolution tracks, the planets can be roughly categorised into four groups (Figure 5.4). (i) A large fraction of planets with initial mass greater than $M_{\rm iso}$ experience efficient mass growth however inefficient migration. These planets become distant super Jupiters or larger brown dwarfs with semi-major axis greater than $30\,\mathrm{au}$, which resemble planets in HR 8799, β Pictoris and PDS 70 systems discovered via direct imaging. (ii) Planets with mass slightly below $M_{\rm iso}$ undergo faster inward migration first followed by rapid run-away gas accretion. They eventually become Jupiter or Saturn size planets around $20\,\mathrm{au}$. (iii) Some sub-$M_{\rm iso}$ planets failed to trigger run-away gas accretion and thus migrates inward without significant mass growth. A few planets in these group are close

to the Neptune in terms of orbits and mass. (iv) Planets that are initially small ($\sim$ a few $\mathrm{M}_\oplus$) and distant ($\sim 100\,\mathrm{au}$) suffer from both inefficient migration and accretion, and they remain largely unchanged.

2. We found both initial planetary mass assignments and α viscosity are important in shaping the architecture of the planetary systems. Planetary systems initialised with the same orbits but different planetary masses can result in distinct final configurations with qualitative difference in semi-major axis and mass (section 5.4.2, Figure 5.5). Increasing the α parameter also results in more massive, compact and inner planetary systems due to enhanced migration and accretion (section 5.4.3, Figure 5.6). The planetary systems also tend to become less stable at the disk stage when α increases.

3. At the end of the disk stage, the majority of the adjacent planet pairs have period ratios smaller than four, and a small fraction of the pairs have period ratio smaller than two (section 5.4.5). Pairs with large period ratios has a small inner planet that undergoes fast migration first and then cause the pair to separate apart (Figure 5.9). The evolution of the resonant angles show that planets in compact planetary systems (e.g., DL Tau) are in a chain of MMR due to the convergent migration and higher order MMR (Figure 5.10).

4. Our stability analysis shows most of the systems can stay stable for at least $10\,\mathrm{Gyr}$ when the perturbative strength $\eta_{\mathrm{per}} < 10^{-6}$ (Figure 5.13). Majority of our results are consistent with the predicted instability time given by Morrison & Kratter (2016) (section 5.6.2). The stabilities of a few planetary systems, particularly AS 209 and DL Tau, have been underestimated largely because of the far-away third planet from the closest planet pair as well as the chain of MMR (Figure 5.15).

We also discuss the implication of our results on future observations. Our predictions suggest the potential existence of a large number of distant gas giants that resemble the observed giant planetary systems (e.g., HR 8799), which may be observed by the next generation telescope such as the upcoming *JWST*. Our results also suggest that additional protoplanets may exist in the inner disk region in order to explain the formation of close-in gas giants via migration and accretion, whose signatures may be resolved by future ALMA observation or *ngVLA* on the nearby PPDs.

Chapter 6

Conclusion and future prospects

Over the last few decades, it has been revealed that the exoplanetary population exhibits a significant diversity with a broad distribution over semi-major axis, planetary mass, etc. The unexpected diversity spurred the formulation of new formation and evolution theories to explains the architecture of the exoplanetary systems that are distinct from our solar system, yet the success of these theories was largely built on the artificial initial conditions that were biased towards the desired outcomes, such as the orbital instability. It therefore poses a need to justify the predictions of these theoretical models on a realistic basis.

As birthplaces for exoplanets, the protoplanetary disks (PPDs) are tightly related to the primordial configurations of the planetary systems, which serve as realistic initial conditions. Nevertheless, prior to the ALMA observation, deducing such initial conditions from the bulk properties of the PPDs involves large uncertainties, since no robust theoretical model can consistently explain the early-stage formation of the planetary core from the dust. The ALMA observation bypasses this fundamental difficulty by resolving the disk substructures on the disks, which are commonly recognised as signatures of protoplanets. Following the planetary interpretation, we can constrain the location and mass of the protoplanets from the disk substructures and connect the observed initial conditions to the observation by evolving the planetary systems with the protoplanetary disk.

In this thesis, based on the initial configurations extracted from protoplanetary disks observed with ALMA, we carry out numerical simulations to investigate the evolution outcomes and examine the long term orbital stability of the planetary systems. Our work are mainly summarised below as:

- We develop mass criteria to classify the gaps into dust-only/dust-and-gas gaps, then give predictions to the planetary masses that are consistent with the core accretion scenario.
- Starting from the realistic initial configurations deduced from the gap structures in ALMA disks, we evolve the planetary systems with consideration of the interaction between the planet and the disk before the disk dispersal. In addition to mutual gravity between star and planets, we include orbital migration, pebble/gas accretion and a gas profile that is adaptive to the feedbacks of the planetary evolution.

- After the disk stage evolution, we continue evolving the planetary systems to examine their long term orbital stability. At this stage, we remove all the disk-related interactions and include both mutual gravitational interactions among stars and planets as well as stochastic perturbations.

Our major findings and conclusions are highlighted below.

- The majority of the gaps in the observed protoplanetary disks can be classified into either dust-only gap and dust-and-gas gap (section 4.4.1). The planetary masses predicted from the gaps range from a few $M_\oplus$ to a few M_J. The predicted planetary masses decrease with the distance from the hosting star, which are consistent with the planetary formation scenario (section 4.4.2).
- During the disk stage, both the orbital migration and planetary accretion can strongly shape the architecture of the planetary systems within a few million years. Generally, the planetary systems become more inner, compact and massive at the end of the disk stage, as compared with their initial configurations. Our synthesised planetary population overlaps with only a fraction of the observed planets, particularly widely separated giant planetary systems discovered via direct imaging. The majority of the observed exoplanets, including the Hot Jupiters, are still outside of the range of the synthesised population.
- We found most of the planetary systems that survive the disk stage remain stable for at least $10\,\mathrm{Gyr}$ (section 5.6), even under perturbations within a reasonable range. The disk evolution stabilises the configuration by letting planets naturally enter orbital mean-motion resonance due to the convergent migration, and the co-migration prevents the planet pair from closer approach. The stability time of the planetary systems mostly agree with the theoretical prediction (section 3.4.1, section 5.6.2).

The above findings have several important implications on future research and observation. First of all, the stable configurations of planetary systems evolved with the disk implies that a stronger perturbation source is needed to generate the instability required by the dynamical evolution models to explain the observed diversity. Since our results in Chapter 5 have already shown that the perturbation from the planetesimal disk alone is not sufficient, other external perturbation sources, such as stellar flybys, are crucial to destabilise the planetary systems after the disk stage. This encourages future observation to better constrain the strength of the available perturbation sources, for example, the closest approach during the stellar flyby.

As we have seen in the simulation, a very turbulent disk with large α viscosity is also possible to destabilise the planetary system at the disk stage. At large α, closer encounter between two adjacent planet is possible due to stronger migration, and the planet-planet scattering event may happen afterwards, which excites the inclination or eccentricity. The eccentric/inclined orbits are prerequisites for tidal circularisation to take effects and eventually produce close-in Hot Jupiters (e.g., Nagasawa et al., 2008). They are also important in producing planets with large spin-orbit misalignment at later stage via Lidov-Kozai oscillation (e.g., Pu & Lai, 2021). In addition, large initial eccentricity is also required for tidal circularization to take effects. Our current numerical model cannot

accommodate such a scattering event occurs at the disk stage. It is therefore encouraged for future simulation (e.g., 2D(3D) hydrodynamical simulations with multiple planets) to incorporate the planet-disk interaction at high eccentricities so as to further investigate the outcome of such unstable cases.

It is also worth to note that our conclusions drawn from the simulation results are based on several assumptions. We adopt a one-to-one correspondence between the gap and embedded planet, which may overestimates the number of planets if multiple planets share a common gap or a single planet creates multiple gaps (Dong et al., 2017; Bae et al., 2017). Moreover, we assume the number of planets does not change with time by neglecting the formation of any new planet in the dust-rich region before the disk dispersal. We also neglect the potential small planets that cannot create observable disk substructure observable to ALMA. The participation of these additional planets may affect the final dynamical architecture due to the coupled nature of the multi-planetary system evolution. A more complete simulation framework in the future should take these factors into account by introducing additional planets at all possible locations.

Furthermore, we would like to stress that the current sample of ALMA disks are inevitably biased towards massive disks that may favour formation of distant, widely-separated giant planetary systems. In smaller disks, formation of close-in and closely-packed terrestrial planets may be more common, and the orbital instability may be easier to be triggered in such systems if the resonance chain breaks during the migration process (McNally et al., 2019). Therefore, it is possible that our conclusion will be revised by the future disk observation focusing on less massive disks.

The similarities between the planetary systems discovered via direct imaging and our synthesised giant planetary systems may imply potential connections between the two. Indeed, the similarity is not only limited to the mass and semi-major axis, but also the dynamical structure: Goździewski & Migaszewski (2014, 2018, 2020) found the planet pairs in HR 8799 are in good 2:1 resonant states, and such orbital resonance can stabilise the system for Gyr timescale. Winn & Fabrycky (2015) also concludes that the observed giant gas planets are close to 2:1 period ratios. As a natural consequence of the convergent migration, the 2:1 resonance appears in many of our planet pairs, without any fine tuned planet or disk parameters. We have found not only the HL Tau system, but also other ALMA disks such as HD 163296 and DL Tau, can evolve to systems alike. The selection bias of the current ALMA disks may be a possible reason, since DSHARP only selects the brightest and most massive nearby disks for the sake of the resolution, which may only favour the formation of massive planets. Having said so, the relative abundance the disks implies that multiple giant planet systems in wide separation like HR 8799 may not be rare, and they may be detected in the future by for example James Webb Space Telescope (*JWST*).

The relatively small overlap between the simulation-synthesised planetary population and the observed exoplanets, particularly those short-period exoplanets observed by Kepler and TESS, can be a motivation for both the disk and exoplanet observation in the future. Firstly, the abundance of the distant planets in our simulation suggests there are potentially more exoplanets to be observed, even in planetary systems that have already been discovered. Secondly, contrary to the evolution picture believed by some previous studies (e.g., Lodato et al., 2019), the orbital migration cannot bridge the difference of semi-major axis distribution between the observed population and the planetary systems

deduced from the observed PPDs. Therefore, in order to reproduce the current observed planetary population, a large number protoplanets have to be formed closer to the star ($< 10\,\mathrm{au}$) at the first place, which are not reflected in the current disk observation due to insufficient resolution. The potential presence of more planetary signatures at the inner region of the disk may be confirmed by the future observation such as the Next-Generation Very Large Array (*ngVLA*) to explore the inner disk substructure with higher resolving power.

Bibliography

Alibert, Y., Mordasini, C., Benz, W., & Winisdoerffer, C. 2005, A&A, 434, 343

Andrews, S. M. 2020, ARA&A, 58, 483

Andrews, S. M., Huang, J., Pérez, L. M., et al. 2018, ApJ, 869, L41

Armitage, P. J. 2009, Astrophysics of planet formation (Cambridge: Cambridge University Press), 1

Bae, J., Zhu, Z., & Hartmann, L. 2017, ApJ, 850, 201

Birnstiel, T., Klahr, H., & Ercolano, B. 2012, A&A, 539, A148

Bitsch, B., Morbidelli, A., Johansen, A., et al. 2018, A&A, 612, A30

Bodenheimer, P. & Pollack, J. B. 1986, Icarus, 67, 391

Boley, A. C. 2017, ApJ, 850, 103

Borucki, W. J., Koch, D., Basri, G., et al. 2010, Science (80-.)., 327, 977

Boss, A. P. 2011, ApJ, 731, 74

Brogan, C. L., Pérez, L. M., Hunter, T. R., et al. 2015, ApJ, 808, L3

Cameron, A. G. 1978, Moon Planets, 18, 5

Chambers, J. E., Wetherill, G. W., & Boss, A. P. 1996, Icarus, 119, 261

Charbonneau, D., Brown, T. M., Latham, D. W., & Mayor, M. 2000, ApJ, 529, L45

Chatterjee, S. & Ford, E. B. 2015, ApJ, 803, 33

Chauvin, G., Lagrange, A. M., Dumas, C., et al. 2004, A&A, 425, 29

Cieza, L. A., Swift, J. J., Mathews, G. S., & Williams, J. P. 2008, ApJ, 686, L115

Cieza, L. A., Casassus, S., Pérez, S., et al. 2017, ApJ, 851, L23

Crida, A., Morbidelli, A., & Masset, F. 2006, Icarus, 181, 587

Deck, K. M. & Batygin, K. 2015, ApJ, 810, 119

Deck, K. M., Payne, M., & Holman, M. J. 2013, ApJ, 774, 129

Dipierro, G. & Laibe, G. 2017, MNRAS, 469, 1932

Dipierro, G., Laibe, G., Price, D. J., & Lodato, G. 2016, MNRAS Letters, 459, L1

Dipierro, G., Price, D., Laibe, G., et al. 2015, MNRAS Letters, 453, L73

Dong, R. & Fung, J. 2017, ApJ, 835, 146

Dong, R., Li, S., Chiang, E., & Li, H. 2017, ApJ, 843, 127

Dong, R., Najita, J. R., & Brittain, S. 2018a, ApJ, 862, 103

Dong, R., Zhu, Z., & Whitney, B. 2015, ApJ, 809, 93

Dong, R., Liu, S.-y., Eisner, J., et al. 2018b, ApJ, 860, 124

Fabrycky, D. C. & Murray-Clay, R. A. 2010, ApJ, 710, 1408

Facchini, S., Birnstiel, T., Bruderer, S., & Van Dishoeck, E. F. 2017, A&A, 605, A16

Flock, M., Ruge, J. P., Dzyurkevich, N., et al. 2015, A&A, 574, A68

Gillon, M., Triaud, A. H. M. J., Demory, B.-O., et al. 2017, Nature, 542, 456

Gladman, B. 1993, Icarus, 106, 247

Goldreich, P. & Schlichting, H. E. 2014, AJ, 147, 32

Goldreich, P. & Tremaine, S. 1979, the Excitation of Density Waves At the Lindblad and, Tech. rep.

—. 1980, ApJ, 241, 425

Götberg, Y., Davies, M. B., Mustill, A. J., Johansen, A., & Church, R. P. 2016, A&A, 592, A147

Goulinski, N. & Ribak, E. N. 2018, MNRAS, 473, 1589

Goździewski, K. & Migaszewski, C. 2014, MNRAS, 440, 3140

—. 2018, ApJL, 238, 6

—. 2020, ApJ, 902, L40

Guilloteau, S., Dutrey, A., Piétu, V., & Boehler, Y. 2011, A&A, 529, A105

Haffert, S. Y., Bohn, A. J., de Boer, J., et al. 2019, Nat. Astron., 3, 749

Hands, T. O., Alexander, R. D., & Dehnen, W. 2014, MNRAS, 445, 749

Hashimoto, J., Muto, T., Dong, R., et al. 2021, ApJ, 908, 250

Hayashi, C., Nakazawa, K., & Nakagawa, Y. 1985, Protostars planets II (A86-12626 03-90). Tucson, AZ, Univ. Arizona Press, 159

Henry, G. W., Marcy, G. W., Butler, R. P., & Vogt, S. S. 2000, ApJ, 529, L41

Hirose, S. & Turner, N. J. 2011, ApJL, 732, 30

Hu, X., Zhu, Z., Okuzumi, S., et al. 2019, ApJ, 885, 36

Huang, J., Andrews, S. M., Dullemond, C. P., et al. 2018a, ApJ, 869, L42

Huang, J., Andrews, S. M., Pérez, L. M., et al. 2018b, ApJ, 869, L43

Ida, S. & Lin, D. N. C. 2004, ApJ, 604, 388

Ikoma, M., Nakazawa, K., & Emori, H. 2000, ApJ, 537, 1013

Jin, S., Li, S., Isella, A., Li, H., & Ji, J. 2016, ApJ, 818, 76

Johansen, A., Ida, S., & Brasser, R. 2019, A&A, 622, A202

Kanagawa, K. D., Muto, T., Tanaka, H., et al. 2016, PASJ, 68, 1

Kanagawa, K. D., Tanaka, H., Muto, T., & Tanigawa, T. 2017, PASJ, 69, 1

Kanagawa, K. D., Tanaka, H., Muto, T., Tanigawa, T., & Takeuchi, T. 2015, MNRAS, 448, 994

Kanagawa, K. D., Tanaka, H., & Szuszkiewicz, E. 2018, ApJ, 861, 140

Kanagawa, K. D., Hashimoto, J., Muto, T., et al. 2021, ApJ, 909, 212

Keppler, M., Benisty, M., Müller, A., et al. 2018, A&A, 617, A44

Kley, W., Peitz, J., & Bryden, G. 2004, A&A, 414, 735

Kudo, T., Hashimoto, J., Muto, T., et al. 2018, ApJ, 868, L5

Kurtovic, N. T., Pérez, L. M., Benisty, M., et al. 2018, ApJ, 869, L44

Kwon, W., Looney, L. W., & Mundy, L. G. 2011, ApJ, 741, 3

Kwon, W., Looney, L. W., Mundy, L. G., & Welch, W. J. 2015, ApJ, 808, 102

Lambrechts, M. & Johansen, A. 2012, A&A, 544, A32

Lambrechts, M., Johansen, A., & Morbidelli, A. 2014, A&A, 572, A35

Lee, M. H. & Peale, S. J. 2002, ApJ, 567, 596

Lin, D. N. C. & Papaloizou, J. 1979, MNRAS, 186, 799

Lin, D. N. C. & Papaloizou, J. C. B. 1993, in Protostars Planets III, ed. E. H. Levy & J. I. Lunine, 749

Lissauer, J. J. 1993, ARA&A, 31, 129

Lodato, G., Dipierro, G., Ragusa, E., et al. 2019, MNRAS, 486, 453

Long, F., Pinilla, P., Herczeg, G. J., et al. 2018a, ApJ, 869, 17

Long, Z. C., Akiyama, E., Sitko, M., et al. 2018b, ApJ, 858, 112

Marois, C., Macintosh, B., Barman, T., et al. 2008, Science (80-.)., 322, 1348

Marois, C., Zuckerman, B., Konopacky, Q. M., Macintosh, B., & Barman, T. 2010, Nature, 468, 1080

Marzari, F. & Weidenschilling, S. J. 2002, Icarus, 156, 570

Mayer, L., Quinn, T., Wadsley, J., & Stadel, J. 2002, Science (80-.)., 298, 1756

Mayor, M. & Queloz, D. 1995, Nature, 378, 355

McNally, C. P., Nelson, R. P., & Paardekooper, S.-J. 2019, MNRAS Letters, 489, L17

Mizuno, H. 1980, Prog. Theor. Phys., 64, 544

Morbidelli, A. & Nesvorny, D. 2012, A&A, 546, A18

Mordasini, C., Alibert, Y., & Benz, W. 2009, A&A, 501, 1139

Morrison, S. J. & Kratter, K. M. 2016, ApJ, 823, 118

Murray, C. D. & Dermott, S. F. 2000, Solar System Dynamics (Cambridge University Press)

Mustill, A. J. & Wyatt, M. C. 2011, MNRAS, 413, 554

Muto, T. & Inutsuka, S. I. 2009, ApJ, 695, 1132

Nagasawa, M., Ida, S., & Bessho, T. 2008, ApJ, 678, 498

Naoz, S., Farr, W. M., Lithwick, Y., Rasio, F. A., & Teyssandier, J. 2011, Nature, 473, 187

Naruse, M., Berthel, M., Drezet, A., et al. 2015, Sci. Rep., 5, arXiv:1509.06382

Nelson, R. P. & Papaloizou, J. C. B. 2004, MNRAS, 350, 849

Nomura, H., Tsukagoshi, T., Kawabe, R., et al. 2021, ApJ, 914, 113

Obertas, A., Van Laerhoven, C., & Tamayo, D. 2017, Icarus, 293, 52

Okuzumi, S., Momose, M., Sirono, S.-i., Kobayashi, H., & Tanaka, H. 2016, ApJ, 821, 82

Ormel, C. W. 2017, in Form. Evol. Dyn. Young Sol. Syst., ed. M. Pessah & O. Gressel, Vol. 445 (Cham: Springer International Publishing), 197

Ormel, C. W. & Klahr, H. H. 2010, A&A, 520, A43

Paardekooper, S. J., Baruteau, C., Crida, A., & Kley, W. 2010, MNRAS, 401, 1950

Paardekooper, S. J., Baruteau, C., & Kley, W. 2011, MNRAS, 410, 293

Paardekooper, S. J. & Mellema, G. 2004, A&A, 425, L9

—. 2006, A&A, 450, 1203

Pérez, L. M., Benisty, M., Andrews, S. M., et al. 2018, ApJ, 869, L50

Picogna, G. & Kley, W. 2015, A&A, 584, A110

Pinte, C., Dent, W. R. F., Ménard, F., et al. 2015, ApJ, 816, 25

Pringle, J. E. 1981, ARA&A, 19, 137

Pu, B. & Lai, D. 2021, MNRAS, 508, 597

Queloz, D., Eggenberger, A., Mayor, M., et al. 2000, A&A, 359, 13

Quillen, A. C. 2011, MNRAS, 418, 1043

Rasio, F. A. & Ford, E. B. 1996, Science (80-.)., 274, 954

Rein, H. 2012, MNRAS Letters, 427, 21

Rein, H. & Liu, S.-F. 2012, A&A, 537, A128

Rein, H. & Papaloizou, J. C. 2009, A&A, 497, 595

Rein, H. & Spiegel, D. S. 2014, MNRAS, 446, 1424

Rein, H. & Tamayo, D. 2015, MNRAS, 452, 376

Ricker, G. R., Winn, J. N., Vanderspek, R., et al. 2014, J. Astron. Telesc. Instruments, Syst., 1, 014003

Robitaille, T. P., Whitney, B. A., Indebetouw, R., & Wood, K. 2007, ApJL, 169, 328

Rodet, L., Su, Y., & Lai, D. 2021, ApJ, 913, 104

Rosotti, G. P., Juhasz, A., Booth, R. A., & Clarke, C. J. 2016, MNRAS, 459, 2790

Rybicki, G. B. & Lightman, A. P. 1979, New York, Wiley-Interscience, 1979. 393 p.

Sachs, A. 1974, Philos. Trans. R. Soc. A Math. Phys. Eng. Sci., 276, 43

Safronov, V. S. 1969, Evoliutsiia doplanetnogo oblaka.

Shakura, N. I. & Sunyaev, R. A. 1973, in X- Gamma-Ray Astron. (Dordrecht: Springer Netherlands), 155

Simbulan, C., Tamayo, D., Petrovich, C., Rein, H., & Murray, N. 2017, MNRAS, 469, 3337

Soummer, R., Hagan, J. B., Pueyo, L., et al. 2011, ApJ, 741, 55

Takahashi, S. Z. & Inutsuka, S.-i. 2016, AJ, 152, 184

Takeuchi, T. & Lin, D. N. C. 2002, ApJ, 581, 1344

Tamayo, D., Rein, H., Petrovich, C., & Murray, N. 2017, ApJ, 840, L19

Tamayo, D., Rein, H., Shi, P., & Hernandez, D. M. 2020, MNRAS, 491, 2885

Tamayo, D., Silburt, A., Valencia, D., et al. 2016, ApJL, 832, 1

Tanaka, H. & Ida, S. 1999, Icarus, 139, 350

Tanaka, H., Murase, K., & Tanigawa, T. 2020, ApJ, 891, 143

Tanaka, H., Takeuchi, T., & Ward, W. R. 2002, ApJ, 565, 1257

Tanigawa, T. & Ikoma, M. 2007, ApJ, 667, 557

Tanigawa, T. & Tanaka, H. 2016, ApJ, 823, 48

Tanigawa, T. & Watanabe, S. 2002, ApJ, 580, 506

van der Marel, N., Dong, R., di Francesco, J., Williams, J. P., & Tobin, J. 2019, ApJ, 872, 112

Varvoglis, H., Sgardeli, V., & Tsiganis, K. 2012, Celest. Mech. Dyn. Astron., 113, 387

Vorobyov, E. I. 2013, A&A, 552, A129

Wang, S., Kanagawa, K. D., Hayashi, T., & Suto, Y. 2020, ApJ, 891, 166

Wang, S., Kanagawa, K. D., & Suto, Y. 2021a, ApJ, 923, 165

—. 2021b

Weber, P., Benítez-Llambay, P., Gressel, O., Krapp, L., & Pessah, M. E. 2018, ApJ, 854, 153

Weidenschilling, S. J. 1977, MNRAS, 180, 57

Winn, J. N. & Fabrycky, D. C. 2015, ARA&A, 53, 409

Winn, J. N., Johnson, J. A., Albrecht, S., et al. 2009, ApJ, 703, L99

Winn, J. N., Noyes, R. W., Holman, M. J., et al. 2005, ApJ, 631, 1215

Winter, A. J., Kruijssen, J. M. D., Longmore, S. N., & Chevance, M. 2020, Nature, 586, 528

Wölfer, L., Facchini, S., Kurtovic, N. T., et al. 2021, A&A, 648, A19

Wolszczan, A. & Frail, D. A. 1992, Nature, 355, 145

Wright, J. T. & Gaudi, B. S. 2013, in Planets, Stars Stellar Syst., Vol. 3 (Dordrecht: Springer Netherlands), 489

Wu, D.-H., Zhang, R. C., Zhou, J.-L., & Steffen, J. H. 2019, MNRAS, 484, 1538

Wu, Y. & Murray, N. 2003, ApJ, 589, 605

Wyatt, M. C. 2003, ApJ, 598, 1321

Xie, C., Ren, B., Dong, R., et al. 2021, ApJ, 906, L9

Yen, H.-W., Liu, H. B., Gu, P.-G., et al. 2016, ApJ, 820, L25

Youdin, A. N. & Lithwick, Y. 2007, Icarus, 192, 588

Zhang, S., Zhu, Z., Huang, J., et al. 2018, ApJ, 869, L47

Zhang, Y. & Jin, L. 2015, ApJ, 802, 58

Zhu, Z., Nelson, R. P., Dong, R., Espaillat, C., & Hartmann, L. 2012, ApJ, 755, 6